International Journal of Antennas and Propagation

Ultra-Wideband Antennas

Guest Editors: James Becker, Dejan Filipovic, Hans Schantz, and Seong-Youp Suh

Ultra-Wideband Antennas

International Journal of Antennas and Propagation

Ultra-Wideband Antennas

Guest Editors: James Becker, Dejan Filipovic,
Hans Schantz, and Seong-Youp Suh

Contents

Hindawi Publishing Corporation
International Journal of Antennas and Propagation
Volume 2008, Article ID 731247, 2 pages
doi:10.1155/2008/731247

Editorial
Ultra-Wideband Antennas

James Becker,[1] Dejan Filipovic,[2] Hans Schantz,[3] and Seong-Youp Suh[4]

[1] *Electrical & Computer Engineering Department, College of Engineering, Montana State University, 610 Cobleigh Hall Bozeman, MT 59717, USA*
[2] *Department of Electrical and Computer Engineering, University of Colorado, Boulder Campus Box 425, Boulder, CO 80309-0425, USA*
[3] *The Q-Track Corporation, 515 Sparkman Drive NW, Huntsville, AL 35816, USA*
[4] *Intel Corporation, 2200 Mission College Boulevard, Santa Clara, CA 95054-1549, USA*

Correspondence should be addressed to Hans Schantz, h.schantz@q-track.com

Received 22 May 2008; Accepted 22 May 2008

Over the last few years much has been published about the principles and applications of electromagnetic waves with large relative bandwidth, or nonsinusoidal waves for short. The next step is the development of the technology for the implementation of these applications. It is generally agreed that the antennas pose the most difficult technological problem.

Henning F. Harmuth,
Antennas and Waveguides for Nonsinusoidal Waves,
New York: Academic Press, 1984, p. xi.

More than twenty years after Harmuth's observations on the difficulties posed by UWB antenna design and six years after the FCC authorized ultra-wideband (UWB) systems, a variety of UWB products are nearing wide-scale commercialization. Antenna designers and engineers have solved the UWB antenna problem in many ways, yielding compact antennas well suited for a variety of applications. Unlike in previous decades when UWB antenna progress came in fits and spurts, today there is an active and growing community of UWB antenna designers sharing their insights and designs at professional conferences, trade shows, and on the pages of technical journals.

A keyword search of Google Patents for "UWB antenna" provides quantitative data to capture these qualitative trends. This metric is somewhat crude and may overlook certain broadband antenna designs not explicitly labeled as "UWB." Similarly, this search may include UWB systems or services that merely mention "UWB antennas." Still, this analysis provides an interesting look at trends and activity in the area of UWB antennas.

Broadband and UWB antennas date back to the earliest days of radio [1]. Harmuth and others pioneered the use of impulse or "nonsinusoidal waves" in the 1970's and 1980's [2]. The Time Domain Corporation and Multi-Spectral So lutions, Inc., were both formed in the late 1980's to commercialize UWB technology.

The US Defense Advanced Research Projects Agency (DARPA) sponsored a review of UWB technology in 1990 in the context of radar applications [3]. This investigation was controversial, upholding the merit and value of UWB technology in general, while dismissing some of the extraordinary claims of novel physics made by certain UWB advocates [4]. By the early 1990's, however, terminology had converged towards the use of the term "ultra-wideband" or "UWB." The first patent with the exact phrase "UWB antenna" was filed on behalf of Hughes in 1993. Figure 1 shows the number of US Patent Applications filed in each year during 1993–2007 containing the exact search phrase "UWB antenna."

The 1990's were an era of only modest interest in UWB antennas, and only a few US patent applications were filed. In 1999, however, UWB became front-page news in USA Today and elsewhere [5]. By 2000, industry leaders like the Time Domain Corporation, Xtreme Spectrum, and others were engaging in active lobbying of the FCC to open up spectrum for UWB applications. Their efforts were rewarded by FCC's Preliminary Report and Order in 2002 [6].

A surge of UWB patents in 2000 accompanied this increased commercial interest. Interest waned somewhat in 2001, followed by yet another surge in 2002 when the FCC

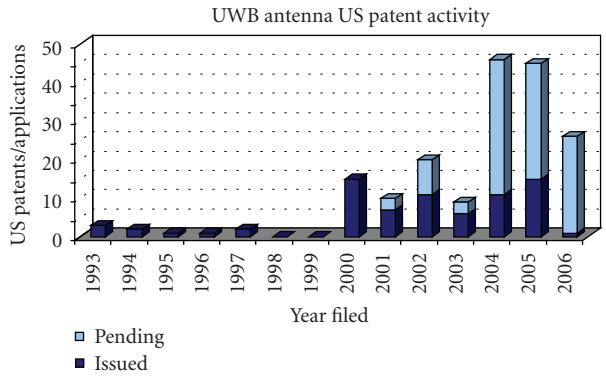

Figure 1: UWB antenna US patent activity by year (1993–2006).

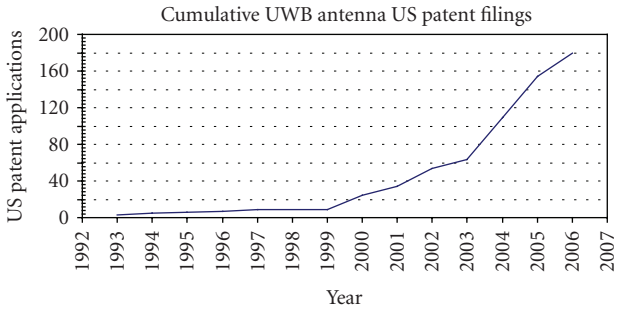

Figure 2: Cumulative UWB antenna US patent activity by year (1993–2006).

authorized UWB. Interest again waned in 2003 before exploding in 2004 and 2005. The pace of innovation dampened only slightly in 2006. Patents filed in 2007 may not yet have been published, so complete data is only available through 2006. The height of the bars in Figure 1 shows the total number of applications filed, some of which have been issued (dark portion) and some of which are still pending or were abandoned after publication (light portion). Clearly the US Patent Office is still dealing with a substantial backlog of UWB-related patents filed in 2004-2005. Figure 2 shows a cumulative plot of UWB antenna US patent filings.

UWB systems have opened up new dimensions of antenna design. Antennas have become an organic part of RF systems, providing filtering and other custom designed frequency-dependent properties. The wide bandwidths of UWB antennas present new challenges for design, simulation, and modeling. Optimizing UWB antennas to meet the demands of UWB propagation channels is similarly challenging. And as always, consumer applications demand compact and aesthetically pleasing designs that must nevertheless perform. Designers are meeting these challenges by extending the bandwidth of familiar antenna architectures like patches and slots. Designers are also using applying familiar techniques like arrays to UWB applications, as well as employing more recent concepts like antenna spectral filtering. The time is ripe for a special issue on UWB antennas that captures this progress and provides insight to where UWB antenna design will go in the future.

James Becker
Dejan Filipovic
Hans Schantz
Seong-Youp Suh

REFERENCES

[1] H. Schantz, *The Art and Science of Ultrawideband Antennas*, Artech House, Boston, Mass, USA, 2005.
[2] H. Harmuth, *Antennas and Waveguides for Nonsinusoidal Waves*, Academic Press, New York, NY, USA, 1984.
[3] C. A. Fowler, J. Entzminger, and J. Corum, "Assessment of ultra-wideband (UWB) technology," *IEEE Aerospace and Electronic Systems Magazine*, vol. 5, no. 11, pp. 45–49, 1990.
[4] C. A. Fowler, "The UWB (impulse) radar caper or 'punishment of the innocent'," *IEEE Aerospace and Electronic Systems Magazine*, vol. 7, no. 12, pp. 3–5, 1992.
[5] K. Maney, "Radical new digital technology may revolutionize communications," *USA Today*, April 1999.
[6] U.S. 47 C.F.R. Part 15 Subpart F Section 15.503d Ultra-Wideband Operation.

Hindawi Publishing Corporation
International Journal of Antennas and Propagation
Volume 2008, Article ID 713858, 8 pages
doi:10.1155/2008/713858

Research Article

Design Aspects of Printed Monopole Antennas for Ultra-Wide Band Applications

K. P. Ray

SAMEER, IIT Campus, Hill Side, Powai, Mumbai 400076, India

Correspondence should be addressed to K. P. Ray, kpray@rediffmail.com

Received 21 May 2007; Accepted 19 January 2008

Recommended by Hans G. Schantz

This paper presents the design equations for lower band-edge frequency for all the regular shapes of printed monopole antennas with various feed positions. The length of the feed transmission line is a critical design parameter of these monopole antennas. Design curves for the length of the feed transmission line for various lower band-edge frequencies for all these regular shaped monopoles have been generated. A systematic study has been presented to explain the ultra-wide bandwidth obtained from these antennas with an example of elliptical monopole antenna.

1. INTRODUCTION

Present time is witnessing a very rapid growth of wireless communications, for which antennas with very large bandwidth are in strong demand, so that various applications are covered with fewer or preferably with a single antenna. It will be preferred that an antenna has bandwidth in excess of frequency range from 800 MHz to 11 GHz or even more, to include all the existing wireless communication systems such as AMPC800, GSM900, GSM1800, PCS1900, WCDMA/UMTS (3G), 2.45/5.2/5.8-GHz-ISM, U-NII, DECT, WLANs, European Hiper LAN I, II, and UWB (3.1–10.6 GHz) [1]. Out of all the above-mentioned wireless systems, ultra-wide bandwidth (UWB) wireless technology is most sought for very high-data-rate and short-range wireless communication systems, coding for security and low probability of interception, rejection of multipath effect, modern radar systems, and so forth. As mentioned above, this technology uses ultra-wide bandwidth of 7.5 GHz, ranging from 3.1 GHz to 10.6 GHz.

Planar and printed monopole antennas are the good candidates for use in UWB wireless technology because of their wide impedance bandwidth and nearly omni-directional azumuthal radiation pattern. Many shapes of planar, also known as planar disc, monopole antennas are reported, which yield very large bandwidth [2–8]. Some of these reported configurations have bandwidth in excess of that required for UWB applications [3]. But, the planar disc configurations are not the most preferred one for these applications, because they are generally mounted on large ground plane, which are perpendicular to the plane of monopole (which makes them three-dimensional structure). Also, the large size ground plane limits the radiation pattern to only half hemisphere. On the other hand, printed monopole antennas (PMAs) are truly planar and have radiation patterns similar to that of a dipole antenna. These monopoles can be integrated with other components on printed circuit board, have reduced size on dielectric substrate, are without backing ground plane and are easy to fabricate. Printed antennas, commonly fabricated on FR4 substrate, are very cost effective, which is ideally suited for UWB technology-based low-cost systems [9–18].

In this paper, design of all the regular geometries of PMA with various feed positions is discussed. Formulae to calculate the lower band-edge (VSWR = 2) frequency for all these printed monopoles are presented. For various feed configurations, frequency-dependent design curves have been generated for 50 Ω microstrip feed line, which yields maximum bandwidth for a given lower band-edge frequency. These design curves, which cover the lower band-edge frequency of 3.1 GHz for UWB applications, are also valid for coplanar feed lines. A systematic study is presented to explain as to how bandwidth increases with increase in lateral dimension of patch giving the example of an elliptical

geometry. The theoretical study of all the configurations has been carried out using HP high-frequency structure simulator (HP HFSS) [19]. All these results are validated with experiments and reported data.

2. DESIGN CONSIDERATIONS OF ANTENNAS FOR UWB TECHNOLOGY

Some of the main features required for antennas for the application of UWB technology are as follows.

(i) It should have bandwidth ranging from 3.1 GHz to 10.6 GHz in which reasonable efficiency and satisfactory omnidirectional radiation patterns are necessary.
(ii) In this ultra-wide bandwidth, an extremely low-emission power level should be ensured. In 2002, the Federal Communication Commission (FCC) has specified the emission limits of −41.3 dBm/MHz.
(iii) The antenna propagates short-pulse signal with minimum distortion over the frequency range.

The first point is the most important one for antenna designers, which translates into the requirement that antenna should have impedance bandwidth ratio of 3.42 : 1 over which VSWR ≤ 2. Such a high impedance bandwidth is only realised using multiresonance printed monopole antenna, which generally exhibit high pass impedance characteristics. For such broadband antenna, unlike single resonance tuned dipole or monopole antennas, some special design considerations have to be taken into account. Instead of resonance or operating frequency, lower band-edge frequency and total bandwidth achieved become the design parameters for these printed monopole antennas. The lower band-edge frequency depends primarily on maximum height of the monopole, whereas bandwidth of the antenna depends on how impedance of various modes is matched with the microstrip or coplanar feed line. These parameters are discussed in details for all the regular geometries of printed monopole antennas.

3. PRINTED MONOPOLE ANTENNA DESIGN

The printed monopole antennas give very large impedance bandwidth with reasonably good radiation pattern in azumuthal plane, which can be explained in the following two ways. The printed monopole antenna can be viewed as a special case of microstrip antenna configuration, wherein the backing ground plane is located at infinity [7]. A patch is fabricated on dielectric substrate (commonly FR4). Beyond the substrate it can be assumed that a very thick air dielectric substrate ($\varepsilon_r = 1$) exists. It makes a microstrip antenna configuration on a thick substrate with ε_r closer to unity, which yields large bandwidth.

Alternatively, printed monopole antennas can be seen as a vertical monopole antenna. A monopole antenna usually consists of a vertical cylindrical wire mounted over the ground plane, whose bandwidth increases with increase in its diameter. A printed monopole antenna can be equated to a cylindrical monopole antenna with large effective diameter. This second analogy has been used to determine the lower band-edge frequency of all regular shapes of printed monopole antennas for various feed configurations.

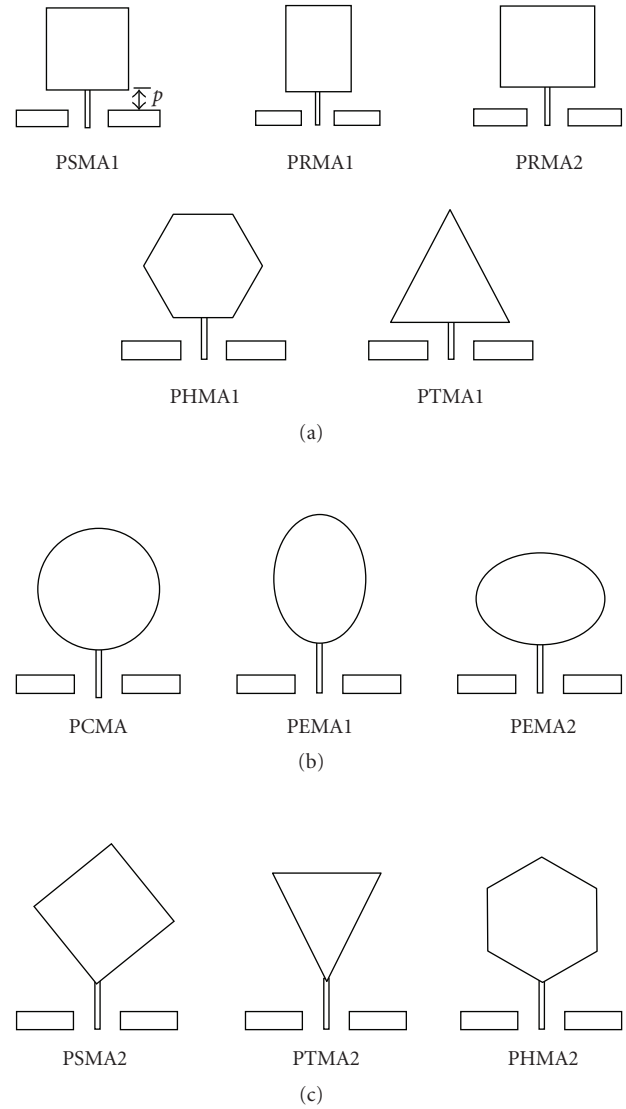

Figure 1: Various regular-shaped PMAs with different feed configurations.

4. LOWER BAND-EDGE FREQUENCY OF PRINTED MONOPOLE ANTENNAS

Various regular shaped printed monopole antennas such as printed square monopole antenna (PSMA), printed rectangular monopole antenna (PRMA), printed hexagonal monopole antenna (PHMA), printed triangular monopole antenna (PTMA), printed circular monopole antenna (PCMA), and printed elliptical monopole antenna (PEMA) for different feed positions are shown in Figure 1. For different feed locations, the suffix 1 or 2, as shown in Figure 1, are put for these monopole antennas. These antennas are generally fabricated on FR4 substrate ($\varepsilon_r = 4.4$, $h = 0.16$ cm, and $\tan\delta = 0.01$) with backing ground plane

removed. For patch dimensions, to cover the lower band-edge frequency of around 900 MHz, the maximum dimension of the substrate is taken as 9 cm × 9 cm, which becomes almost half when the lower band-edge frequency is doubled [9]. These patches can be fed by 50 Ω microstrip line or by coplanar waveguide. For both these cases, the optimum width of the backside ground plane in the case of microstrip feed or coplanar ground plane is 1 cm. These data are verified through simulation for all the configurations shown in Figure 1.

To estimate the lower band-edge frequency of printed monopole antennas, the standard formulation given for cylindrical monopole antenna can be used with suitable modification [3]. The equation was worked out for the planar monopole antennas. If L is the height of the planar monopole antenna in cm, which is taken same as that of an equivalent cylindrical monopole, and r in cm is the effective radius of the equivalent cylindrical monopole antenna, which is determined by equating area of the planar and cylindrical monopole antennas, then the lower band-edge frequency is given as [3]

$$f_L = \frac{c}{\lambda} = \frac{7.2}{(L + r + p)}\ \text{GHz}, \tag{1}$$

where p is the length of the 50 Ω feed line in cm. Unlike the planar disc monopole antennas, the printed configuration has dielectric layer on one side of the monopole. This dielectric material increases the effective dimensions of the monopole leading to reduction in the lower band-edge frequency. This is also confirmed by simulation studies. Hence, more appropriate equation for the lower band-edge frequency is given as

$$f_L = \frac{7.2}{\{(L + r + p) \times k\}}\ \text{GHz}. \tag{2}$$

With reference to various configurations in Figure 1, L and r are calculated as follows.

If S is the side length of the PSMA, then

$$\begin{aligned} L &= S, \quad r = \frac{S}{2\pi} \quad \text{for PSMA1}, \\ L &= \sqrt{2}S, \quad r = \frac{S}{2\sqrt{2}\pi} \quad \text{for PSMA2}. \end{aligned} \tag{3}$$

For PRMA, if length = L and width = W, then

$$\begin{aligned} L &= L, \quad r = \frac{W}{2\pi} \quad \text{for PRMA1}, \\ L &= W, \quad r = \frac{L}{2\pi} \quad \text{for PRMA2}. \end{aligned} \tag{4}$$

For PTMA, if the side length is T, then the values of L and r of the effective cylindrical monopole are determined for both PTMA1 and PTMA2 as

$$L = \frac{\sqrt{3}T}{2}, \qquad r = \frac{T}{4\pi}. \tag{5}$$

Similarly, for the PHMA with side length H, the L and r values of the equivalent cylindrical monopole antenna are obtained by equating their areas as follows:

$$\begin{aligned} L &= \sqrt{3}H, \quad r = \frac{3H}{4\pi} \quad \text{for PHMA1}, \\ L &= 2H, \quad r = \frac{3\sqrt{3}H}{8\pi} \quad \text{for PHMA2}. \end{aligned} \tag{6}$$

For PCMA with radius A, values of L and r of the equivalent cylindrical monopole antenna are given by $L = 2A$ and $r = A/4$.

Finally, for PEMA with semimajor axis = A and semiminor axis = B, the L and r of the effective cylindrical monopole are determined as

$$\begin{aligned} L &= 2A, \quad r = \frac{B}{4} \quad \text{for PEMA1}, \\ L &= 2B, \quad r = \frac{A}{4} \quad \text{for PEMA2}. \end{aligned} \tag{7}$$

As discussed earlier, PMA can be thought of as a variation of microstrip antenna, in which the ground plane is considered to be located at infinity. Following this analogy, the factor k in (2) can be thought of as having similar significance as $\sqrt{\varepsilon_{\text{eff}}}$. For commonly used FR4 substrate with $\varepsilon_r = 4.4$ and $h = 0.159$ cm, the empirical value of $k = 1.15$ estimates lower band-edge frequency within 10%. Equation (2) with $k = 1.15$ has been validated for various reported PMA configurations. For example, a PRMA with dimension $L = 3.0$ cm, $W = 2.0$ cm, and $p = 0.2$ cm with $\varepsilon_r = 4.4$ in [16] has measured value of $f_L = 1.59$ GHz, whereas (2) yields the value of 1.77 GHz. For second reported PRMA with dimension $L = 1.15$ cm, $W = 1.2$ cm, and $p = 0.15$ cm with $\varepsilon_r = 3.38$, simulated f_L is 4.22 GHz [17], against the calculated value of 4.199 GHz using (2). Similarly, the values of frequency calculated using (2) with $k = 1.15$ for PEMA tally very well with measured values reported in [12, 13]. For the dimension $A = 8.6$ mm, $B = 7.31$ mm, and $p = 0.5$ mm in [12], the reported measured value of frequency is 3.17 GHz, whereas (2) yields the value of 3.206 GHz. The reported measured value of frequency for the dimension of $A = 10$ mm, $B = 10$ mm, and $p = 1$ mm is 2.7 GHz [13], against the calculated value of 2.664 GHz using (2). Thus, (2) provides starting point for the design of PMAs.

Another important parameter, which decides the lower band-edge frequency as shown in (2), is the length of 50 Ω feed line p. This feed probe length, the bottom contour of the printed monopole patch and the ground plane, three together form the impedance matching network at multiple adjacent resonances of the patch simultaneously. This leads to an increase in bandwidth. Therefore, for different bottom shapes of the patches, the feed length p will be different. Based on this criterion, the various regular shaped patches have been grouped in three categories in Figure 1. In Figure 1(a), the feed transmission line sees abrupt straight edge of the patch shape like PSMA, PRMAs, PTMA, and PHMA. Second category, as shown in Figure 1(b), consists of patches like PCMA and PEMAs having smooth transition

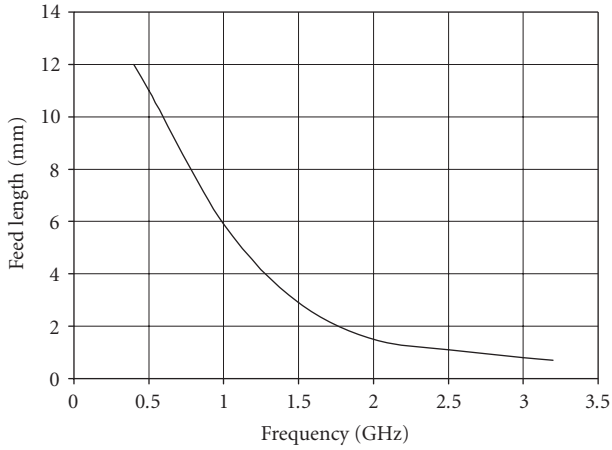

Figure 2: Variation of feed length p with lower band-edge frequency f_L for PMAs shown in Figure 1(a).

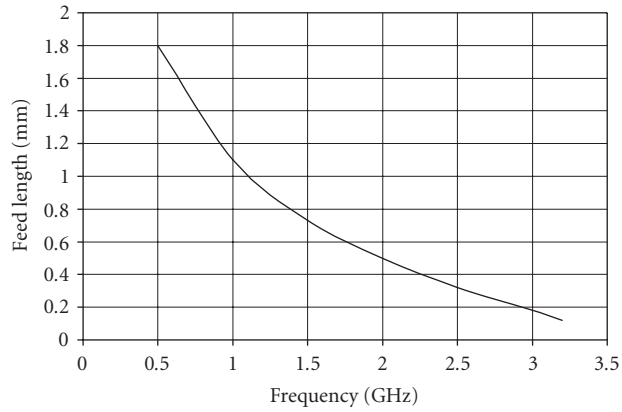

Figure 3: Variation of feed length p with lower band-edge frequency f_L for PCMA and PEMAs.

between transmission line and the curved bottom of the patch. In the third category, as shown in Figure 1(c), transition takes place through bottom corner of the patch and feed transmission line. The value of p, for lower band-edge frequency with maximum bandwidth, for these three categories has been discussed here.

To generate design data for the 50 Ω feed line length p, for different f_L, to obtain maximum bandwidth for all the PMAs under three categories were designed using (2) for various values of f_L starting from 0.5 GHz to 3.1 GHz. This frequency range covers lower band-edge frequency of all the communication channels including that of UWB technology. The value of p for each case for every printed configuration has been optimised to obtain maximum bandwidth using HP HFSS software. The optimised value of p, for given f_L and maximum bandwidth, is almost same for all the five configurations under category of Figure 1(a). These values of p versus f_L are plotted in Figure 2. For maximum bandwidth, when f_L increases from 0.5 GHz to 3.1 GHz, the value of p decreases from 12 mm to about 0.7 mm. Though these five configurations were optimised for maximum bandwidth, the highest bandwidth ratio obtained was around 2.7 : 1. This is a relatively moderate bandwidth ratio, which is attributed to the discontinuity at the junction of a feed point, where the feed line abruptly gets truncated by a straight base of the PMAs. Figure 3 shows the variation of p with f_L for the second category of PMAs, which includes PCMA and both PEMAs as shown in Figure 1(b). For this case also, as f_L increases, feed length p reduces, but magnitude of p is an order less as compared to that of PMAs under the first category. Here, when f_L increases from 0.5 GHz to 3.1 GHz, the value of p decreases from 1.8 mm to about 0.12 mm. These design curves on p are validated with measurements and reported results. The optimum value of $p = 0.3$ mm reported for PCMA at $f_L = 2.69$ GHz is exactly same as read from Figure 3 [9]. This category of PMAs gives maximum bandwidth. The three PMAs under third categories, that is, vertex fed PMAs, as shown in Figure 1(c), did not exhibit same behaviour with respect to one another. However, for some cases, the value of p versus f_L is closer to those of PMAs under second categories than those of first categories. The values of p as shown in Figures 2 and 3 are for the microstrip feed which has been found exactly the same for coplanar waveguide feed as well.

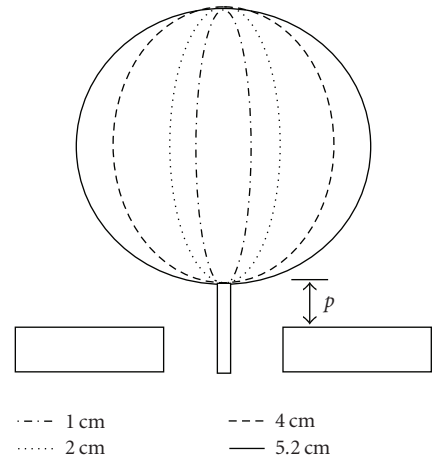

Figure 4: PEMAs with $2A = 4.8$ cm and $2B$ equal to (— - —) 1 cm, (- - - -) 2 cm, (– – –) 4 cm, and (——) 5.2 cm.

5. ULTRA-WIDE BANDWIDTH OF A PEMA

The PMA, as discussed earlier, is viewed as an equivalent thick cylindrical monopole antenna. In the radiating metallic patch, various higher order modes get excited. With optimum feed and increased lateral dimension (i.e., larger width of the patch) all the modes will have larger bandwidth, hence will undergo smaller impedance variation. The shape and size of these planar antennas can be optimised to bring in impedance of all the modes within VSWR = 2 circle in the Smith chart, leading to very large impedance bandwidth. This has been demonstrated taking the example of PEMA.

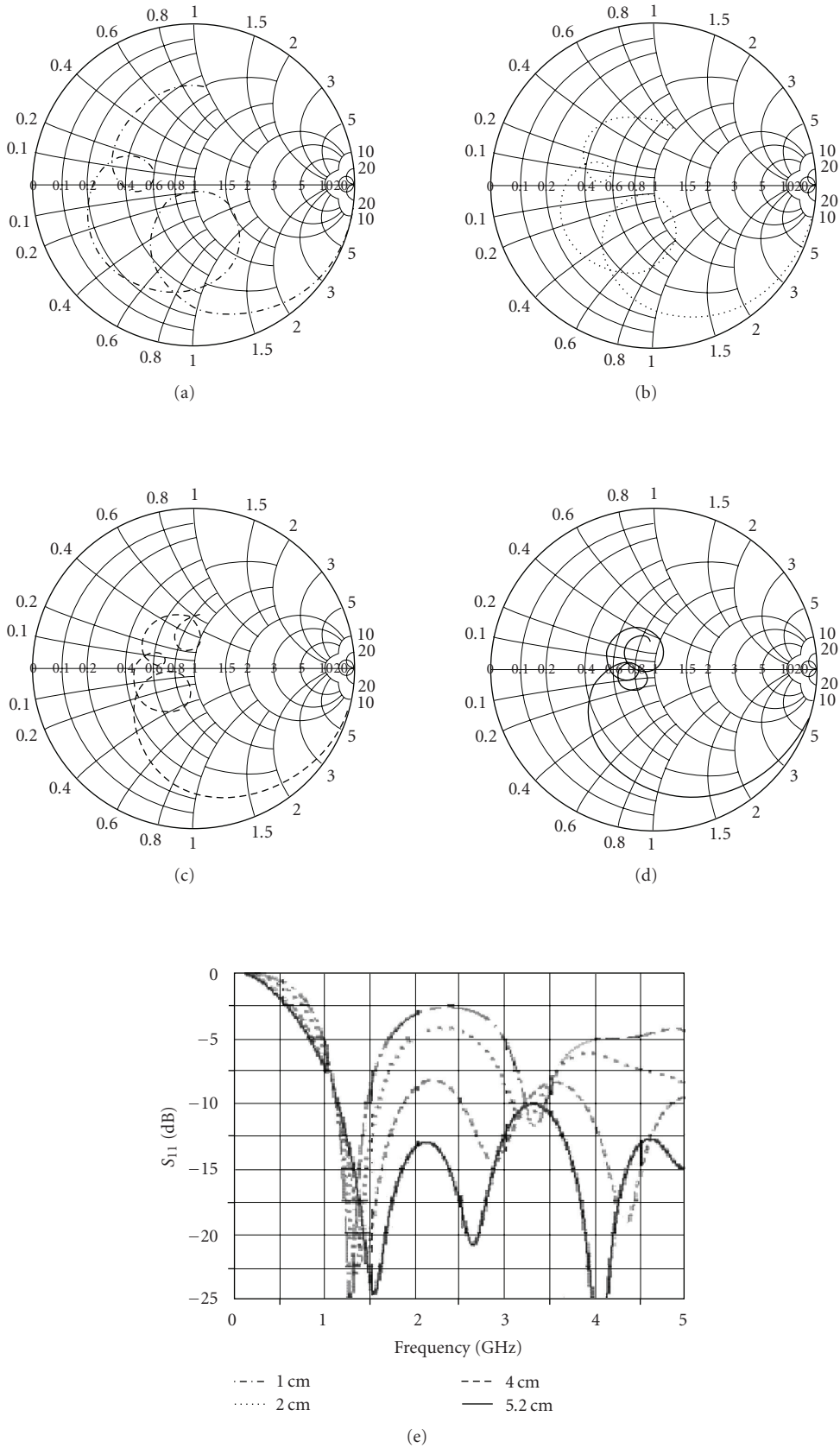

Figure 5: Impedance loci and return loss plot of four PEMAs with $2A = 4.8$ cm and $2B$ equal to (— - —) 1 cm, (- - - -) 2 cm, (– – –) 4 cm, and (——) 5.2 cm.

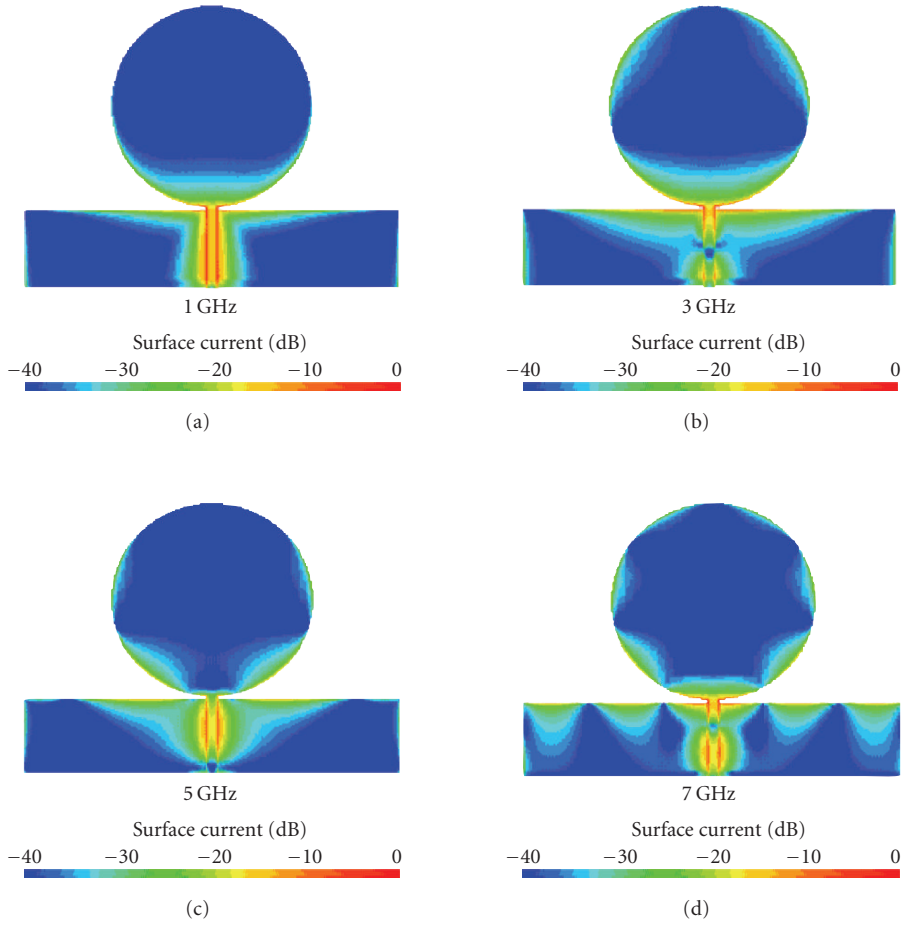

Figure 6: Simulated current distributions of a PEMA at 1 GHz, 3 GHz, 5 GHz, and 7 GHz.

The PEMAs were designed on FR4 substrate ($\varepsilon_r = 4.4$, $h = 0.16$ cm, and $\tan\delta = 0.01$) for $f_L \sim 1.1$ GHz. The value of p for this f_L as read from Figure 3 is 1 mm. The height of the PEMA is kept fixed at $2A = 4.8$ cm so that the f_L remains almost the same. To bring out the variation of input impedance and hence the bandwidth with increased lateral dimension of PEMA, four different values of $2B$ were chosen as 1 cm, 2 cm, 4 cm, and finally 5.2 cm. These configurations are shown in Figure 4. These four PEMAs were analysed using HP HFSS software up to the maximum frequency range of 5 GHz. These results in the form of impedance loci in Smith chart and corresponding return loss plots are shown in Figure 5. It is noted from Smith chart in Figure 5(a) that for $2B = 1$ cm, the PEMA behaves as a thin strip monopole antenna, which is equivalent to thin wire monopole. Here, impedance variation around and in between various loops, which indicates different modes of the elliptical patch, is large, leading to very less impedance bandwidth. As $2B$ increases, the impedance variation around and in between various modes reduces, bringing smaller loops closer to each other yielding increased bandwidth. This effect is clearly seen in impedance loci plots of Figures 5(b) to 5(d) for $2B = 2.0$ cm to 5.2 cm. The increased bandwidth can be read from the corresponding return loss plot of Figure 5(e). For

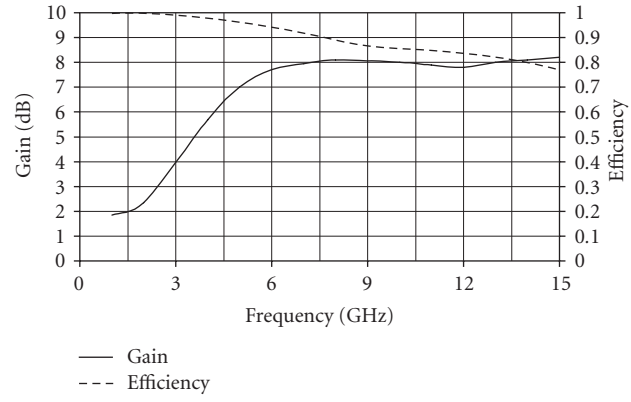

Figure 7: Variation of gain and efficiency of a PEMA with $2A = 4.8$ cm and $2B = 5.2$ cm.

$2B = 5.2$ cm, all the loops curl around the centre of the Smith chart, bringing them inside VSWR = 2 circle. This leads to increase in bandwidth beyond 5 GHz. For the fourth case of $2A = 4.8$ cm and $2B = 5.2$ cm, the PEMA was analysed up to 16 GHz.

For this optimised configuration of PEMA, the simulated surface current distributions at four frequencies are shown

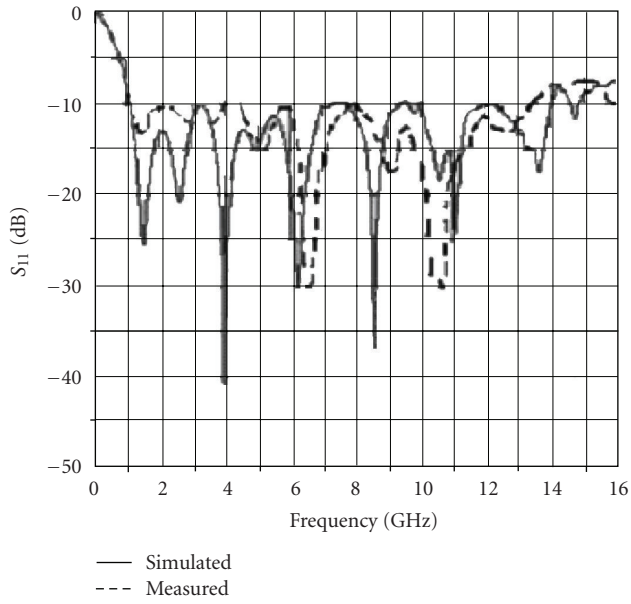

Figure 8: Return loss plots of a PEMA with $2A = 4.8$ cm and $2B = 5.2$ cm (——) simulated, (– – –) measured.

in Figure 6. Figure 6(a) shows the current distribution on the patch near the first resonance at 1 GHz. The current is distributed mainly along the edges and the feed point. Along the periphery of the PEMA, there is one half-cycle variation of current, which indicated the fundamental mode. On the ground plane, the current is distributed mainly on the upper edge. This explains the importance of an optimised dimension of the ground plane. The current distribution at 3 GHz has three times more variation as that at 1 GHz. Similarly, current distribution at 5 and 7 GHz is also shown in Figure 6. With increase in frequency, the current distribution has more half-cycle variations but with reduced amplitude and confines to the outer boundaries of the patch. The gain and efficiency of this antenna is plotted in Figure 7. The value of gain increases linearly and then saturates, while the efficiency decreases from 100% to approximately 80% for the frequency range from 1 GHz to 15 GHz. The gain increases from 1.84 dB to around 7.7 dB for the variation of frequency from 1 GHz to 6 GHz because of increase in effective area with frequency. Later, the increase is only approximately 0.5 dB for 6 to 15 GHz because of decreased efficiency. There is less current variation and hence impedance variation between various modes of the PEMA, which also leads to partial filling of nulls in the radiation pattern at higher order modes. Therefore, in complete bandwidth, the elevation and azumuthal radiation patterns remain qualitatively similar to that of the cylindrical monopole antenna. At lower frequencies, azimuthal radiation patterns are close to omnidirectional, whereas in elevation it is a figure of eight because of the very small ground plane. At higher frequencies, radiation patterns in both the planes remain similar to those at lower frequencies with more variations in the elevation plane. Moreover, these PMAs being asymmetrical configurations in two perpendicular planes, perfect omnidirectional azumuthal radiation pattern is not achieved and also cross-polar levels are high. Cross-polar levels are approximately 15 dB down as compared to corresponding copolar levels at lower frequencies, which become only around 5 dB down at highest frequency of the bandwidth. The configuration was fabricated and tested for the bandwidth. Simulated and measured S_{11} plots are compared in Figure 8. There is good agreement between the two plots. The measured bandwidth is from 1.1 GHz to 13.5 GHz against the simulated bandwidth of 1.06 GHz to 14.1 GHz.

6. CONCLUSION

Multiresonance printed monopole antennas are being used increasingly for applications of UWB technology because of their attractive features. Some of the design aspects of these antennas have been discussed in this paper. A systematic study has been presented to explain ultra-wide impedance bandwidth obtained from an elliptical monopole antenna.

ACKNOWLEDGMENTS

The author would like to acknowledge the help received from Y. Ranga, S. Tewari, M. D. Pandey, and M. K. D. Ulaganathan.

REFERENCES

[1] Z. N. Chen and M. Y. W. Chia, Broadband Planar Antennas: Design and Applications, John Wiley & Sons, Chichester, UK, 2006.

[2] M. Hammoud, P. Poey, and F. Colombel, "Matching the input impedance of a broad band disc monopole," Electronics Letters, vol. 29, no. 4, pp. 406–407, 1993.

[3] N. P. Agrawall, G. Kumar, and K. P. Ray, "Wide-band planar monopole antennas," IEEE Transactions on Antennas and Propagation, vol. 46, no. 2, pp. 294–295, 1998.

[4] H. G. Schantz, "Planar elliptical element ultra-wideband dipole antennas," in *Proceedings of the IEEE Antennas and Propagation Society International Symposium*, vol. 3, pp. 44–47, San Antonio, Tex, USA, June 2002.

[5] K. P. Ray, G. Kumar, and P. V. Anob, "Wideband circular wire mesh and annular ring monopole antennas," Microwave and Optical Technology Letters, vol. 48, no. 12, pp. 2459–2461, 2006.

[6] K. P. Ray, G. Kumar, and P. V. Anob, "Wide band planar modified triangular monopole antennas," Microwave and Optical Technology Letters, vol. 49, no. 3, pp. 628–632, 2007.

[7] K. P. Ray, P. V. Anob, R. Kapur, and G. Kumar, "Broadband planar rectangular monopole antennas," Microwave and Optical Technology Letters, vol. 28, no. 1, pp. 55–59, 2001.

[8] G. Kumar and K. P. Ray, Broad Band Microstrip Antennas, Artech House, Boston, Mass, USA, 2003.

[9] J. Liang, C. C. Chiau, X. Chen, and C. G. Parini, "Study of a printed circular disc monopole antenna for UWB systems," IEEE Transactions on Antennas and Propagation, vol. 53, no. 11, pp. 3500–3504, 2005.

[10] Q. Ye and W. R. Lauber, "Microstrip ultra-wideband dipole antenna simulation by FDTD," in *Proceedings of the IEEE Antennas and Propagation Society International Symposium*, vol. 3, pp. 620–623, Columbus, Ohio, USA, June 2003.

[11] J.-P. Zhang, Y.-S. Xu, and W.-D. Wang, "Ultra-wideband microstrip-fed planar elliptical dipole antenna," Electronics Letters, vol. 42, no. 3, pp. 144–145, 2006.

[12] K. C. L. Chan, Y. Huang, and X. Zhu, "A planar elliptical monopole antenna for UWB applications," in *Proceedings of the IEEE/ACES International Conference on Wireless Communications and Applied Computational Electromagnetics*, pp. 182–185, Honolulu, Hawaii, USA, April 2005.

[13] C.-Y. Huang and W.-C. Hsia, "Planar elliptical antenna for ultra-wideband communications," Electronics Letters, vol. 41, no. 6, pp. 296–297, 2005.

[14] K. P. Ray and Y. Ranga, "Ultra-wideband printed modified triangular monopole antenna," Electronics Letters, vol. 42, no. 19, pp. 1081–1082, 2006.

[15] K. P. Ray, Y. Ranga, and P. Gabhale, "Printed square monopole antenna with semicircular base for ultra-wide bandwidth," Electronics Letters, vol. 43, no. 5, pp. 263–265, 2007.

[16] M. John and M. J. Ammann, "Optimization of impedance bandwidth for the printed rectangular monopole antenna," Microwave and Optical Technology Letters, vol. 47, no. 2, pp. 153–154, 2005.

[17] H. A.-S. Mohamed, A. E. Abdelnasser, Z. E. Atef, and E. S. Charles, "Design of wideband printed monopole antenna using WIPL-D," in *Proceedings of the 20th Annual Review of Progress in Applied Computational Electromagnetics (ACES '04)*, Syracuse, NY, USA, April 2004.

[18] M. Ferrando-Bataller, M. Cabedo-Fabrés, E. Antonino-Daviu, and A. Valero-Nogueira, "Overview of planar monopole antennas for UWB applications," in *Proceedings of the European Conference on Antennas and Propagation (EuCAP '06)*, Nice, France, November 2006.

[19] HP high frequency structure simulator HP HFSS, version 5., 1999.

Hindawi Publishing Corporation
International Journal of Antennas and Propagation
Volume 2008, Article ID 267197, 9 pages
doi:10.1155/2008/267197

Research Article

Parametric Study of Ultra-Wideband Dual Elliptically Tapered Antipodal Slot Antenna

Xianming Qing, Zhi Ning Chen, and Michael Yan Wah Chia

Institute for Infocomm Research, 20 Science Park Road, #02-21/25 TeleTech Park, Singapore 117674

Correspondence should be addressed to Xianming Qing, qingxm@i2r.a-star.edu.sg

Received 29 April 2007; Accepted 11 November 2007

Recommended by Hans G. Schantz

Parametric study of the impedance and radiation characteristics of a dual elliptically tapered antipodal slot antenna (DETASA) is undertaken in this paper. Usually, the performance of the DETASA is sensitive to the parameters, the effects of major geometry parameters of the radiators and feeding transition of the DETASA on antenna performance are investigated across the frequency range of 1–18 GHz. The information derived from this study provides guidelines for the design and optimization of the DETASAs which are widely used for UWB applications.

1. INTRODUCTION

The cochannel interference and multipath effects of wireless communication systems can be reduced by using directional antennas [1–4]. Some of the current point-to-multipoint systems are using horn antennas for this reason, but the horn antennas are too bulky to be integrated with the rest of the wireless packages and suffer high cost of fabrication. Tapered slot antennas (notch antenna, Vivaldi antenna) have been widely used in phased and active arrays for radar systems for many years [5, 6]. They are good candidates for multifunction communication applications because of their stable directional patterns and consistent impedance matching over a very broad operating frequency range without any tuning elements as well as low profile and unobtrusive planar structures. Therefore, they have been proposed for emerging UWB wireless communications and radar applications [7–10].

The dual elliptically tapered antipodal slot antenna (DETASA) [11, 12] is a modified version of the antipodal Vivaldi radiator [13]. It differs from the conventional antipodal Vivaldi antennas since the inner and outer edges of the slotline radiator of the DETASA are elliptically tapered. The slotline radiator is fed by a pair of parallel strip lines which are transformed from a microstrip line. The variations of antipodal Vivaldi antennas were studied both analytically and experimentally [14, 15]. However, the reports hardly discuss effects of antenna parameters on the impedance and radiation characteristics of the DETASA, which is vital for an engineer to design and optimize the antenna.

Therefore, this paper investigates the effects of major geometrical parameters of the DETASA on the impedance matching, gain, and radiation patterns to provide engineers with a clear design guideline. First, Section 2 shows a design as a reference for the following discussion. The geometry of the DETASA as well as comparison of simulated and measured results is introduced. Then, Section 3 demonstrates the effects of the antenna parameters on the impedance matching. After that, Section 4 discusses the impact of the antenna parameters on the radiation characteristics including gain, cross-polarization levels, and radiation patterns in both E- and H-planes. Finally, conclusions are drawn in the last section.

2. ANTENNA CONFIGURATION

Consider a typical DETASA antenna shown in Figure 1. It comprises two main parts: tapered slotline radiator and feeding transition, which are usually printed on a piece of PCB. The tapered slotline radiator shown in Figure 1(b) is configured by two conducting arms which are symmetrically on opposite sides of a substrate with respect to the y-axis. The

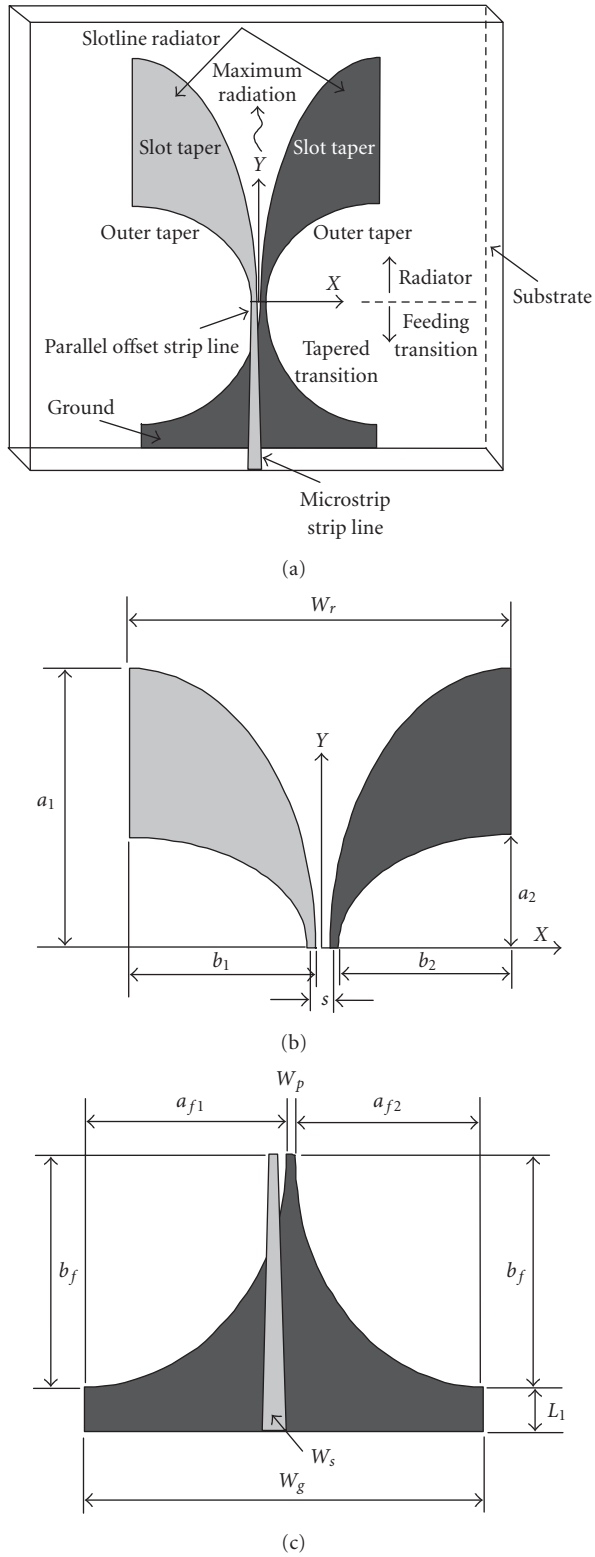

Figure 1: Geometry of a typical DETASA: (a) overall view, (b) tapered slotline radiator, and (c) feed line transition.

slot tapers of the conducting arms follow the outline of a quarter ellipse with major axis a_1 and minor axis b_1; the outer tapers are also elliptically tapered, and take the profile of a quarter ellipse with major axis a_2 and minor axis b_2. Tapering the outer conductor edge provides the convenience for antenna feeding and additional design degrees of freedom for optimizing antenna impedance and radiation performance. It is known that the lower frequency limit of this type of antenna is determined by the cutoff mechanism of the flare, namely, at the lowest operating frequency, the aperture (W_r) is $\lambda_s/2$, where λ_s is the wavelength of the slotline [5, 11, 16]. The feeding transition is shown in Figure 1(c) where a 50-Ω microstrip line (strip width, W_s, and ground width, W_g) is transformed to a parallel offset strip line (width W_p, offset S) to feed the tapered slotline radiator. The strip line is linearly tapered, while the ground plate is elliptically tapered. The profile of the ground taper takes the outlines of two quarter ellipses which are determined by major and minor axes (a_{f1}, b_f), and (a_{f2},b_f), respectively.

The E-plane of the DETASA shown in Figure 1 is on x-y plane ($\theta = 90°$), and the H-plane is on y-z plane ($\phi = 90°$). The maximum radiation will be in y-direction ($\theta = 90°$, $\phi = 90°$). The parametric studies will be carried out over a frequency range of 1–18 GHz, where the parameters a_1, a_2, W_g, b_f, S, and W_p will be considered. When a selected parameter is investigated, the rest of the parameters are unchanged. For comparison, the aperture W_r of the slotline radiator is fixed during the study to fix the lower edge of the operating frequency range. The parametric study will be conducted by the aid of using commercial software XFDTD [17] which is based on FDTD method.

To validate the simulation results, a DETASA prototype was simulated by using the XFDTD software first; the prototype was then fabricated and measured. The parameters of the reference design are $a_1 = 50$ mm, $b_1 = 25$ mm, $a_2 = 20$ mm, $b_2 = 24$ mm, $W_g = 51$ mm, $W_s = 1.86$ mm, $W_p = 1.0$ mm, $S = 0.5$ mm, $a_{f1} = 26$ mm, $a_{f2} = 24$ mm, $b_f = 25$ mm; substrate = RO4003, thickness = 0.8128 mm, $\epsilon_r = 3.38$-j0.002. The simulated and measured results in terms of return loss, gain, and radiation patterns are illustrated in Figures 2 and 3. It is found that the agreement is very good. Therefore, the using of simulated results for further parametric study is viable.

3. PARAMETRIC STUDIES: IMPEDANCE CHARACTERISTICS

Figure 4 shows the return loss of the DETASAs with varying side intercepts, $a_1 - a_2$, of the slotline radiator. It is seen that compared with the reference design with $a_1 = 50$ mm and $a_2 = 20$ mm, the larger side intercepts ($a_1 = 70$ mm, $a_2 = 20$ mm, and $a_1 = 50$ mm, $a_2 = 10$ mm) degrade impedance matching characteristic in particular at the lower edge of the bandwidth. The smaller side intercepts ($a_1 = 30$ mm, $a_2 = 20$ mm, and $a_1 = 50$ mm, $a_2 = 40$ mm) lead to the worse results than the larger. The reason is that the small-side intercepts bring the outer edges of the slotline radiator close to the slot edges, which makes the conducting arms too narrow to maintain the slotline characteristics, especially at lower frequencies.

Figure 5 illustrates the impact of the feeding transition on the impedance matching. Figure 5(a) shows that the

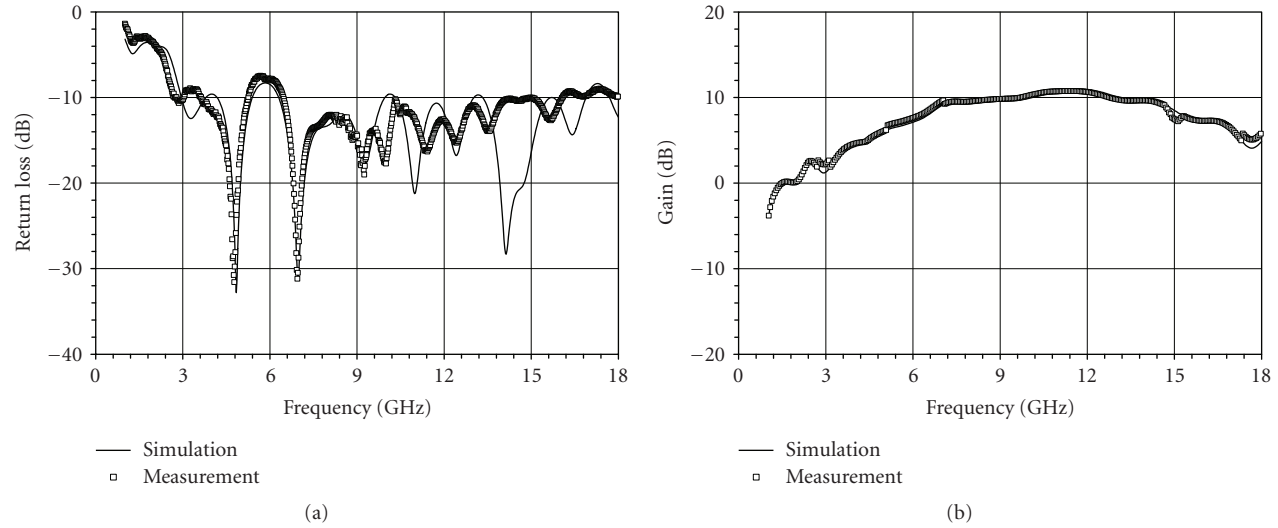

FIGURE 2: Comparison of simulated and measured return loss and gain of the reference DETASA shown in Figure 1; (a) return loss, (b) gain.

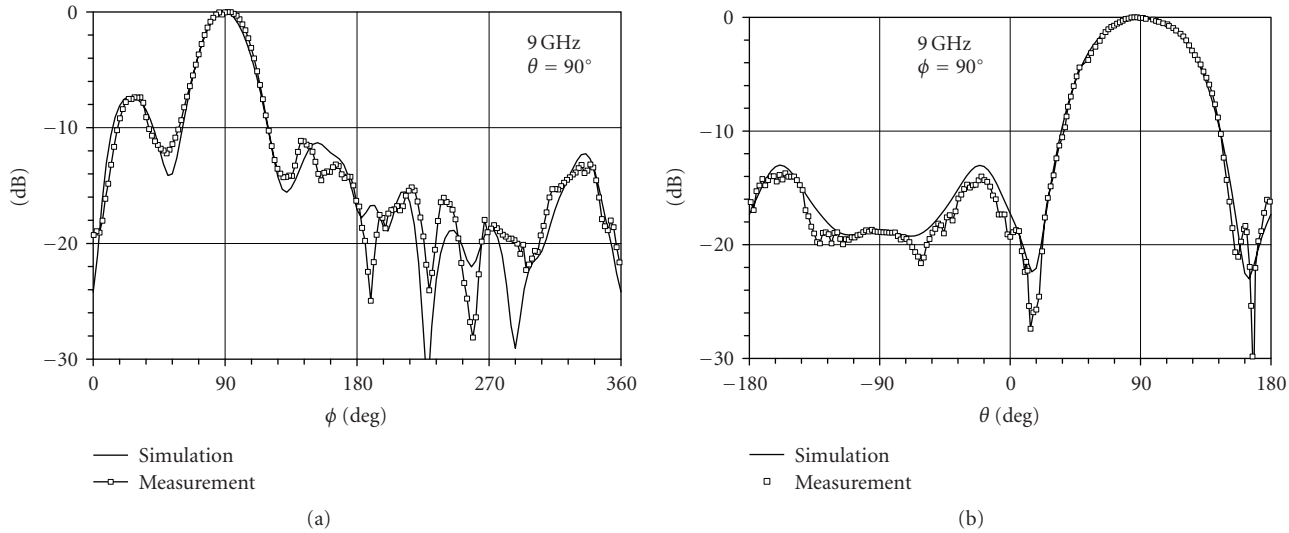

FIGURE 3: Comparison of simulated and measured radiation patterns of the reference DETASA shown in Figure 1; (a) E-plane, (b) H-plane.

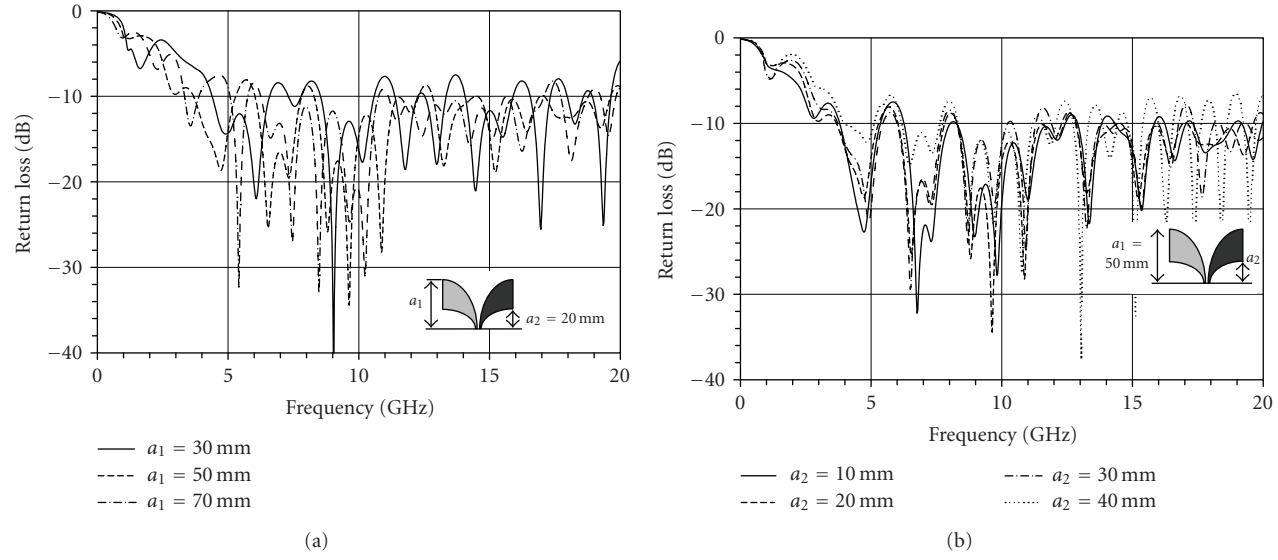

FIGURE 4: Return loss for varying the side intercepts, $a_1 - a_2$, of the slotline radiator.

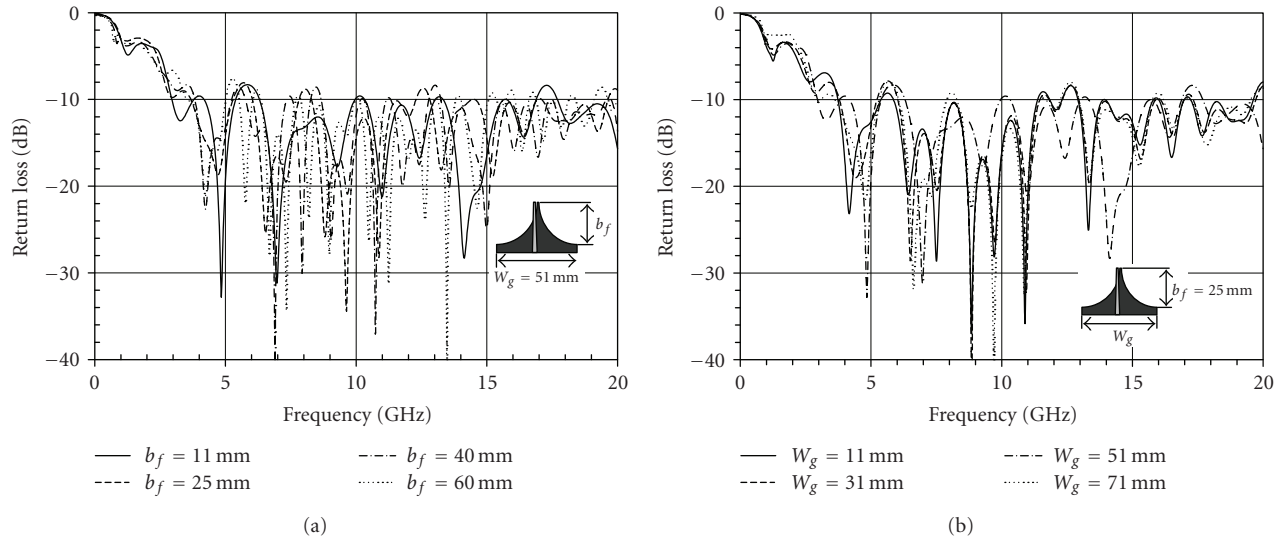

Figure 5: Return loss for different feeding transition configuration.

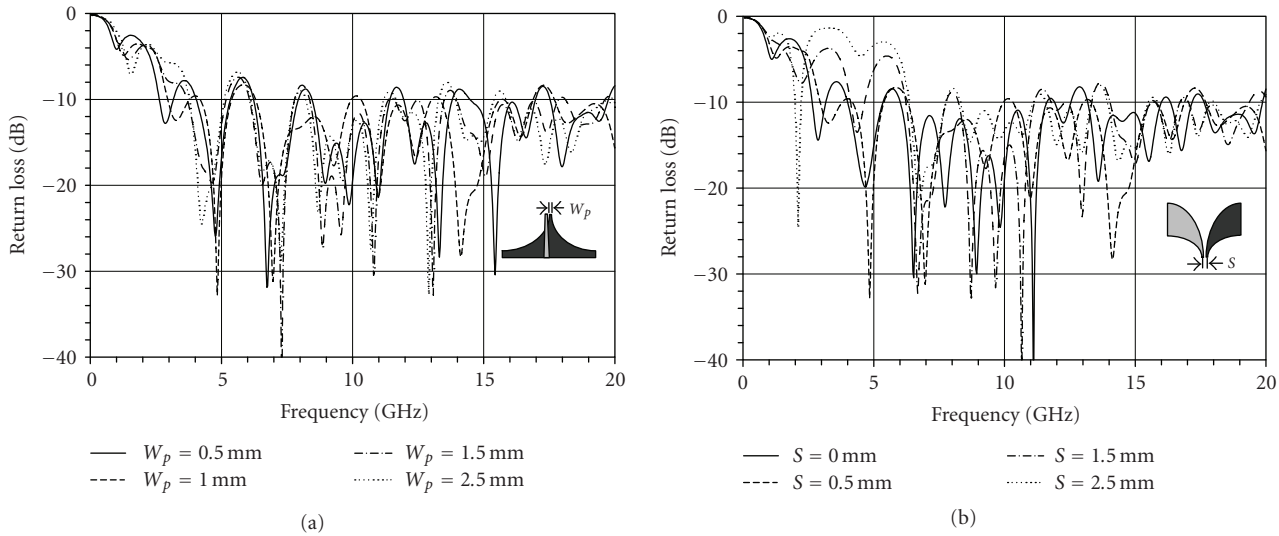

Figure 6: Return loss for varying parallel strip lines.

impedance matching is slightly affected by the length of the transition over 1–18 GHz. The similar phenomena can be observed when changing width of the tapered ground plate, W_g, as shown in Figure 5(b). Therefore, it is concluded that the length of the feeding transition and the width of the tapered ground plate have little impact on the impedance matching of the DETASA. From impedance matching point of view, a compact DETASA can be realizable by using a miniaturized feeding transition.

Figure 6 shows the return loss of the DETASAs for different parallel offset strip lines by varying the width, W_p, and the offset, S. From Figure 6(a), it is found that the effect of the strip width to impedance matching is limited. Smaller W_p is preferable for better impedance matching at lower frequencies. Figure 6(b) shows that the offset of the parallel strip line, S, has a significant impact on the return loss of DETASA; larger offset degrades the impedance matching a lot below 7 GHz. It suggests that smaller W_p and S are adequate in DETASA design for better impedance matching, especially for lower frequencies. Furthermore, W_p and S can be optimized for specific DETASA configuration.

4. PARAMETRIC STUDIES: RADIATION CHARACTERISTICS

In this section, we will address the impact of the geometry parameters of the DETASA on its radiation characteristics: gain, cross-polarization, radiation patterns including main beam, side lobe, and back lobe levels. Note that the gain addressed in this paper is the realized gain which includes the mismatching loss of the antenna.

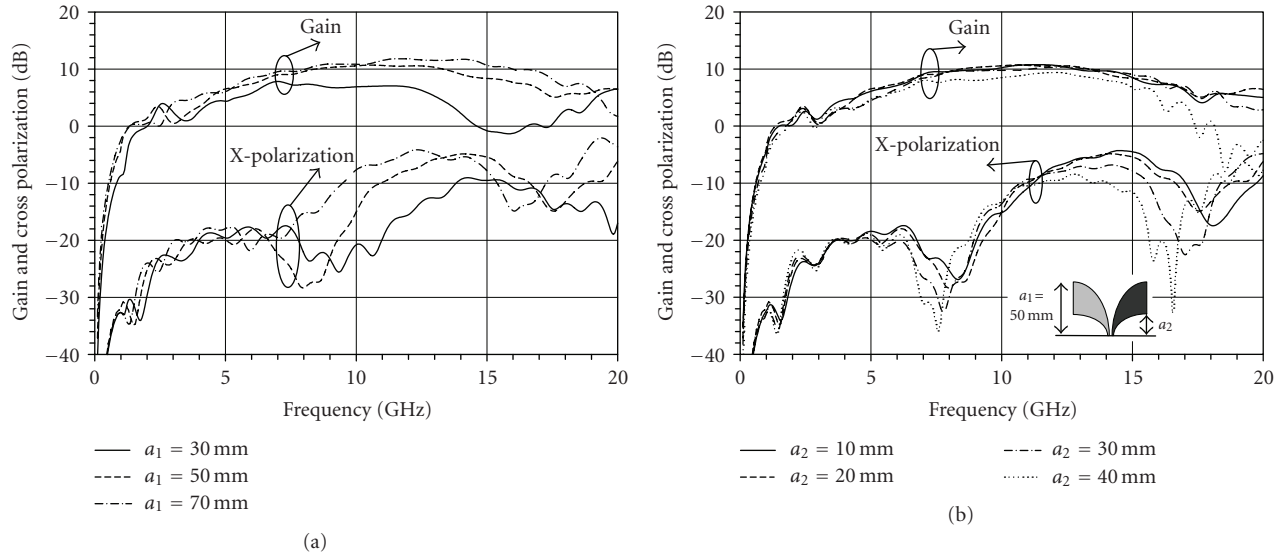

Figure 7: Gain and cross-polarization levels for varying the length of slot taper, a_1, and outer taper, a_2, of the slotline radiator.

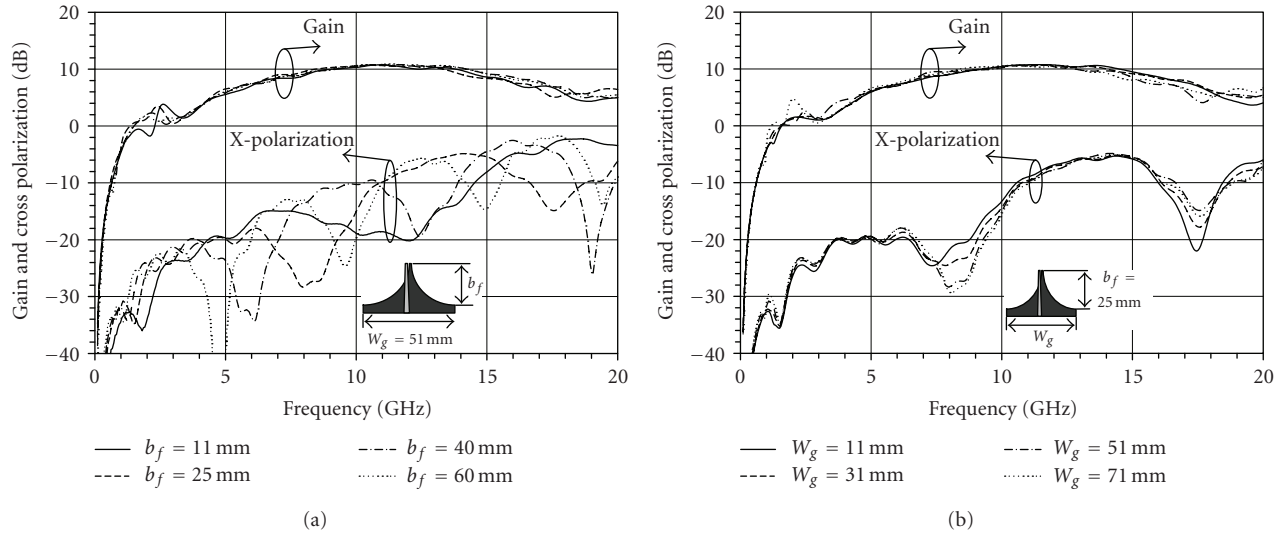

Figure 8: Gain and cross polarization with different ground profiles of feeding transition.

Figure 7 shows the impact of varying lengths of slot taper and outer taper of the slotline radiator on gain and cross-polarization levels. Figure 7(a) shows that the increase in the length of slot taper, a_1, for the fixed outer edge (a_2 = 20 mm) results in higher gain and cross-polarization levels in particular at higher frequencies. The gain drops significantly when a_1 is reduced to 30 mm because the narrow conducting arms cause the slotline radiator to not operate well. From Figure 7(b), we can find that the outer taper primarily affects the cross-polarization levels. Larger a_2 offers lower cross-polarization level. Again, the narrower conducting arm (a_1 = 50 mm, a_2 = 40 mm) reduces the gain especially at the frequencies higher than about 15 GHz.

As shown in Figure 8, it is found that the gain of the DETASA is almost unaffected by the feeding transition. The length of the tapered ground, b_f, has a great effect on the cross-polarization levels of the antenna as the operating frequency is higher than 5 GHz as shown in Figure 8(a) whereas the width of the tapered ground, W_g, hardly affects the cross-polarization level as can be seen in Figure 8(b).

Figure 9 shows the gain and cross-polarization levels of the DETASAs for changing parallel offset strip lines. It is clear that width of the strip lines, W_p, and offset of the strip lines, S, have little effect on the gain. Also, W_p does not affect the cross-polarization level below 12.5 GHz but the increasing W_p lowers cross-polarization levels at higher frequencies. Figure 9(b) shows that the increasing S results in lower cross-polarization levels at higher frequencies.

In general, all cases suffer higher cross-polarization levels at higher frequencies. The reason is the inherent asymmetrical features of antipodal structures, namely, two conducting arms of the DETASA are positioned at opposite sides

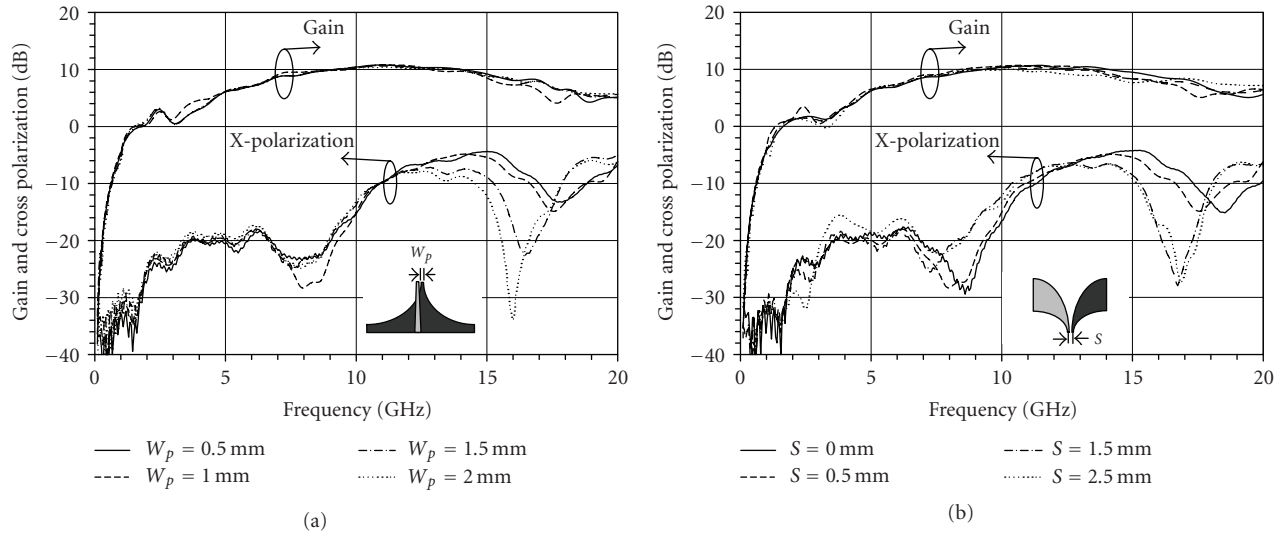

Figure 9: Gain and cross-polarization levels for parallel strip lines.

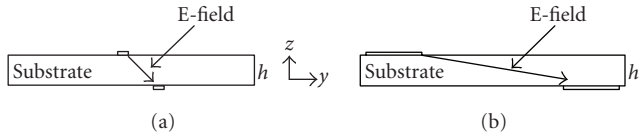

Figure 10: Cross-section view of the DETASA: (a) cross section of the DETASA next to the feeding transition, (b) cross section of the DETASA close to the aperture.

of the substrate, which causes the fields in slotline to be skew as shown in Figure 10. The skewness of the field in the slotline is more serious in the starting area which corresponds to radiation at higher frequencies. In the area close to the aperture, the separation of the conducting arms become larger so that the skewness of field is brought down and lower cross-polarization is observed at lower frequencies. Higher cross polarization at higher frequencies is the drawback of the microstrip-line-fed DETASA, the effective way to reduce cross polarization of such antenna has been reported yet.

The characteristics of radiation patterns in E- and H-planes are investigated in terms of the beamwidth, sidelobe, and backlobe levels. Figure 11 compares the radiation patterns of the DETASAs at 9 GHz for varying length of slot taper, a_1. Figures 11(a) and 11(b), respectively, show the patterns in the E- and H-planes. The E-plane patterns are asymmetrical because of the instinct of the antipodal structure. The length of the slot taper is found to have a slight effect on the beamwidth in the E-planes but a significant impact on the sidelobe and backlobe levels. Figure 11(b) demonstrates that the length of the slot taper has the largest effect on the beamwidth, sidelobe, and backlobe levels in the H-planes. The longer the length a_1 is, the narrower the main beam is. The angular locations of the peaks and nulls of sidelobes as well as the shape and levels of backlobes are changed as well. It should be noted that with $a_1 = 30$ mm, the sidelobes, and backlobes increase a lot in both E- and H-planes.

Figure 12 discusses the effects of varying length of the outer edge, a_2, on the radiation characteristics of the DETASAs. Figure 12(a) shows the radiation patterns in the E-plane. The outer taper mainly affects the sidelobe and backlobe of the patterns. The smaller a_2 leads to lower sidelobe levels. The influences of the outer taper on H-plane patterns are shown in Figure 12(b). Again, the outer taper has a great effect on the sidelobe and backlobe levels of the patterns. The angular location and the level of sidelobe as well as backlobe change significantly for varying a_2. Therefore, the length of outer edge, a_2, can be optimized for desired sidelobe and backlobe performance in both the E- and H-planes.

For further understanding the radiation characteristics of the DETASA, the current distribution on the conducting arms is calculated by using IE3D [18] which is based on moment method. Figure 13 shows the currents of two DETASAs with different slotline radiator configurations. For the DETASA which has large side intercept, $a_1 - a_2$ (shown in Figure 13(a)), the currents along the edges of the slot taper are large in quantity so they dominate the radiation of the antenna. The currents along the outer edge are oppositely directed and small in quantity so that they contribute less to the radiation. However, when conducting arms becomes very narrow, that is, the side intercept is very small (shown in Figure 13(b)), the currents along the inner and outer edges of the slot taper are similarly directed and almost equal in quantity. The radiating structure does not behave as a Vivaldi radiator but more like a V-shaped dipole. This is the reason of those DETASAs, which have small side intercepts, demonstrate lower gain, higher sidelobe and backlobe levels.

Figure 14 illustrates the radiation patterns of the DETASAs in the E- and H-planes for changing length of tapered ground, b_f. Refer to Figure 14(a), the length of the tapered ground has main effect on sidelobe and backlobe of the E-plane patterns. The pattern becomes more symmetrical when

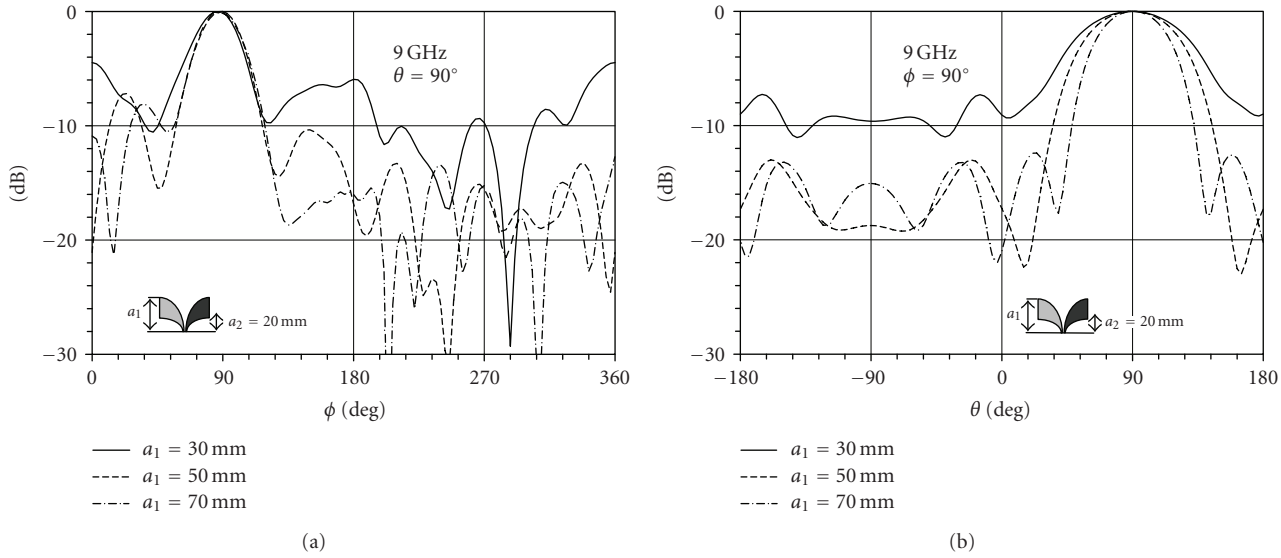

Figure 11: Radiation patterns of DETASAs for varying length of slot taper, a_1, in (a) E-plane and (b) H-plane.

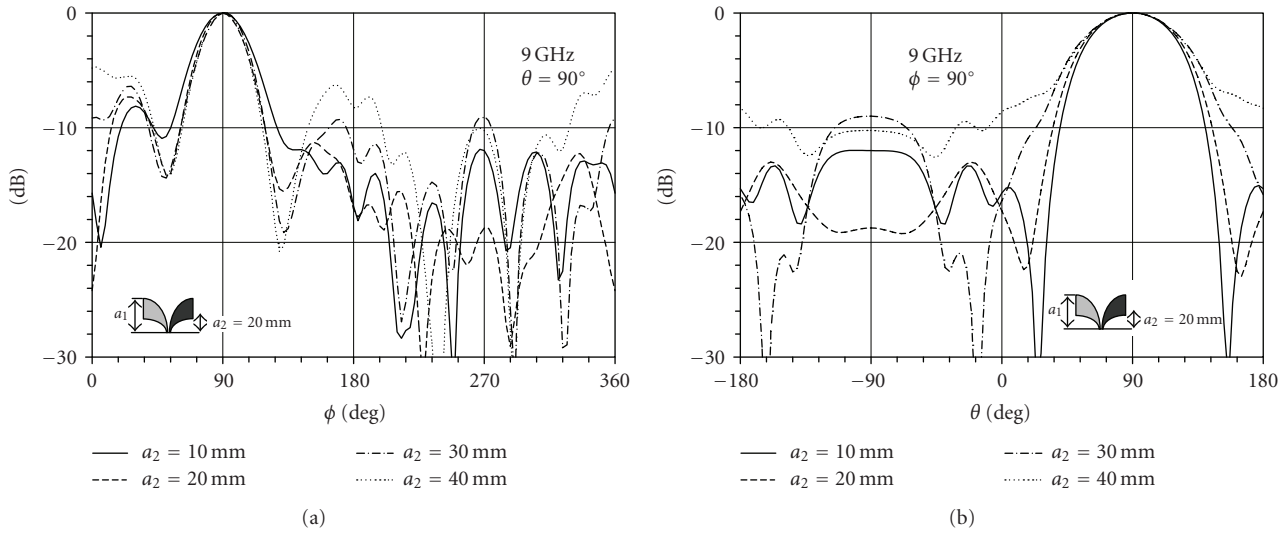

Figure 12: Radiation patterns of DETASAs for varying length of outer taper, a_2, in (a) E-plane, (b) H-plane.

tapered ground is longer. In H-planes, no significant impact is observed but the low backlobe is achieved for a specified ground length, $b_f = 25$ mm.

Figure 15 presents the E-plane and H-plane patterns of the DETASA with the width of the tapered ground, W_g, varying from 11 mm to 71 mm. Again, the width of the tapered ground affects the sidelobe and backlobe levels in the E-planes and the backlobe levels in the H-planes. Conclusively, a small width W_g is conducive to the symmetry of E-plane patterns.

It is concluded that the effect of the feeding transition to the radiation patterns is limited to the sidelobe and backlobe. As shown in Figure 13, the currents on the tapered ground plate are small and mainly along the tapered edges. For those feeding transitions which are longer in length, for example, $b_f = 60$ mm or smaller in width, for example, $W_g = 11$ mm, the antenna structure tends to be more symmetrical with respect to the y-axis; furthermore, the direction of the currents on the ground plate tends to y-direction so that they cause less distortion to the radiation, the antenna patterns becomes more symmetrical in E-plane.

5. CONCLUSIONS

This paper has investigated the effects of major geometry parameters on the impedance and radiation performance of the DETASA. The investigation was conducted to explore the general behavioral trends of the DETASA rather than to design a specific antenna. The parametric study has been done over 1–20 GHz band and yielded a wealth of information which will benefit antenna engineers for their design and optimization of the DETASA.

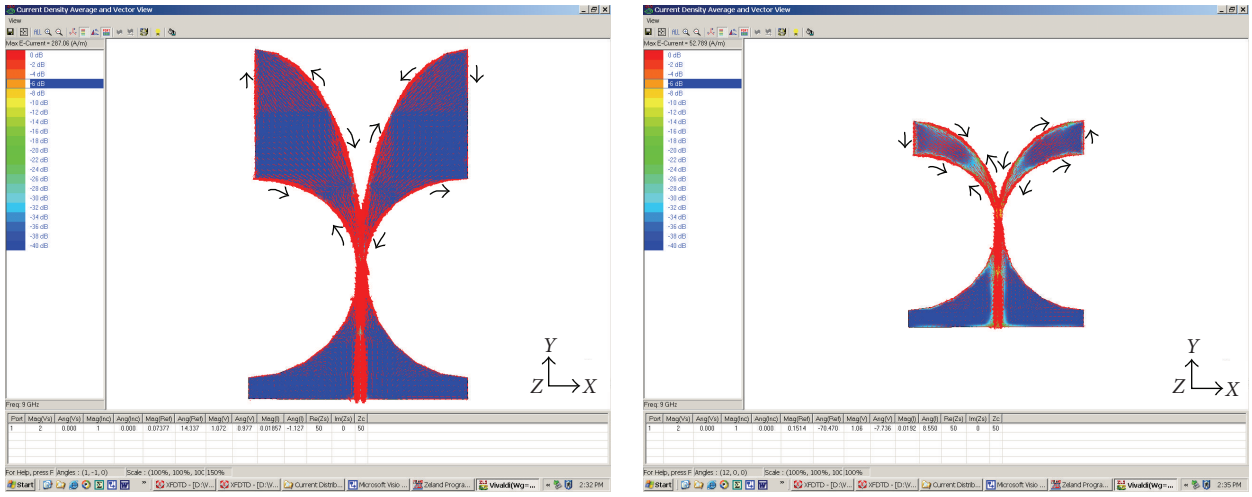

(a) (b)

Figure 13: Current distribution for DETASAs with different profile of slotline radiator: (a) $a_1 = 50$ mm, $a_2 = 20$ mm, (b) $a_1 = 30$ mm, and $a_2 = 20$ mm.

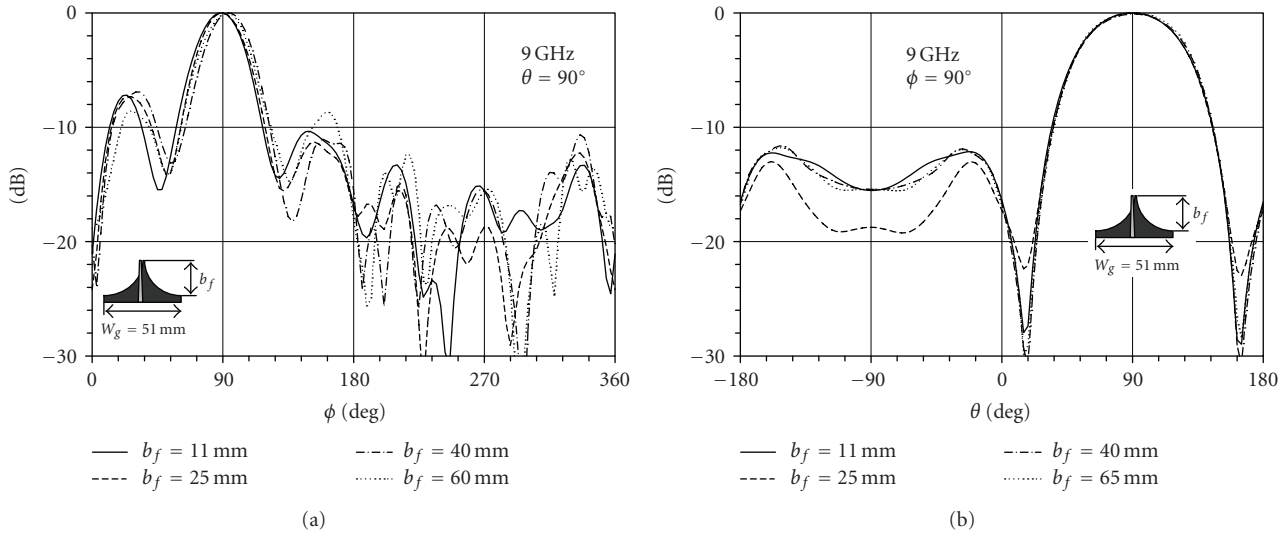

(a) (b)

Figure 14: Radiation patterns of DETASAs for changing length of tapered ground, b_f, in (a) E-plane, (b) H-plan.

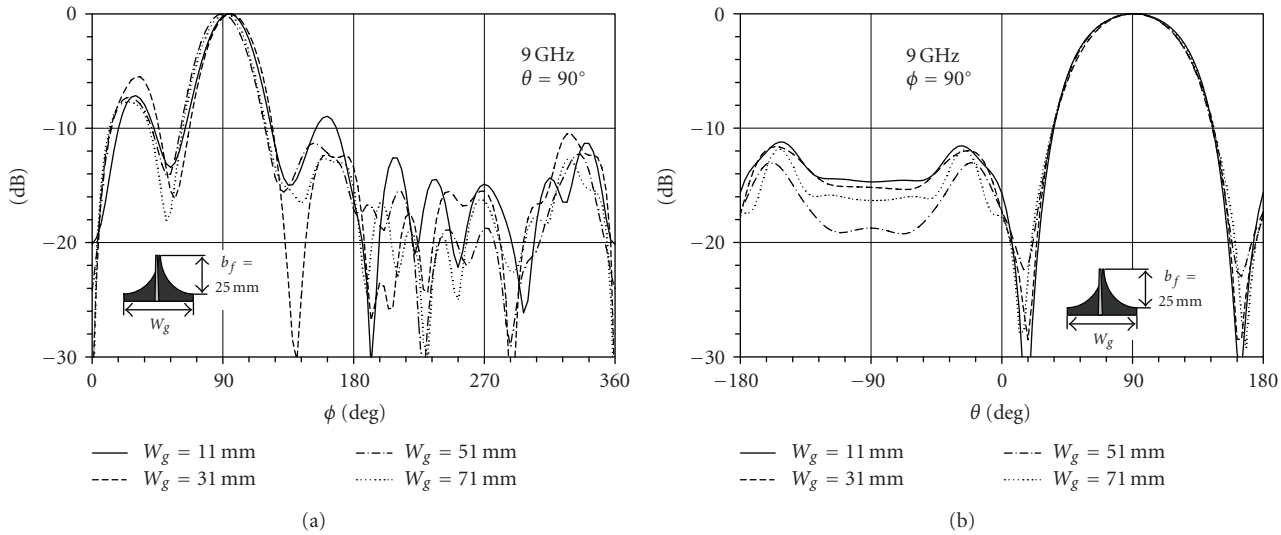

(a) (b)

Figure 15: Radiation patterns of DETASAs for changing width of tapered ground, W_g, in (a) E-plane, (b) H-plane.

From the study, we can conclude the following points, which can be used as a guideline for the design of the DETASA.

(1) The side intercepts, $a_1 - a_2$, of the slotline radiator and separation of the parallel offset strip lines, S, have major effects on the impedance matching characteristic. Large-side intercept and small separation result in good impedance matching especially at lower frequencies. The profile of the tapered ground plate has a slight effect on impedance matching.

(2) The length of the slot taper, a_1, mainly controls the gain of DETASA. Usually, longer slot taper offers higher gain but results in higher cross-polarization levels. The outer edge shows little impact on the gain. The feeding transition has shown very little effect on antenna gain but somewhat on the cross-polarization levels

(3) The length of the slot taper, a_1, has shown a significant effect on main beam of the H-plane patterns, while the main beam of the E-plane patterns is nearly unaffected. The longer the slot taper is, the narrower the H-plane beamwidth is. The length of the outer taper, a_2, has little effect on the main beam but affects the sidelobe and backlobe levels. Therefore, it can be optimized to suppress sidelobe and backlobe levels.

(4) The size of the feeding transition primarily affects the sidelobe levels of E-plane patterns. Longer or smaller feeding transitions offer more symmetrical radiation patterns in E-plane.

REFERENCES

[1] W. C. Y. Lee, *Mobile Communcations Design Fundamentals*, Wiley, New York, NY, USA, 1993.

[2] T. Manabe, Y. Miura, and T. Ihara, "Effects of antenna directivity and polarization on indoor multipath propagation characteristics at 60 GHz," *IEEE Journal on Selected Areas in Communications*, vol. 14, no. 3, pp. 441–447, 1996.

[3] S.-S. Jeng, G. T. Okamoto, G. Xu, H.-P. Lin, and W. J. Vogel, "Expérimental evaluation of smart antenna system performance for wireless communications," *IEEE Transactions on Antennas and Propagation*, vol. 46, no. 6, pp. 749–757, 1998.

[4] P. Cardieri and T. S. Rappaport, "Application of narrow-beam antennas and fractional loading factor in cellular communication systems," *IEEE Transactions on Vehicular Technology*, vol. 50, no. 2, pp. 430–440, 2001.

[5] P. J. Gibson, "The vivaldi aeriel," in *9th European Microwave Conference*, pp. 101–105, Brighton, UK, October 1979.

[6] R. Janaswamy and D. H. Schaubert, "Analysis of tapered slot antenna," *IEEE Transactions on Antennas and Propagation*, vol. 35, no. 9, pp. 1058–1065, 1987.

[7] W. Sörgel, C. Waldschmidt, and W. Wiesbeck, "Transient responses of a Vivaldi antenna and a logarithmic periodic dipole array for ultra wideband communication," in *IEEE International Antennas and Propagation Symposium and USNC/CNC/URSI North American Radio Science Meeting*, vol. 3, pp. 592–595, Columbus, Ohio, USA, June 2003.

[8] S.-G. Kim and K. Chang, "Ultra wideband exponentially-tapered antipodal vivaldi antennas," in *IEEE Antennas and Propagation Society Symposium 2004 Digest held in Conjunction with: USNC/URSI National Radio Science Meeting*, vol. 3, pp. 2273–2276, Monterey, Calif, USA, June 2004.

[9] M. Manteghi and Y. Rahmat-Samli, "A novel UWB feeding mechanism for the TEM horn antenna, reflector IRA, and the Vivaldi antenna," *IEEE Antennas and Propagation Magazine*, vol. 46, no. 5, pp. 81–87, 2004.

[10] Y. Yunqiang, Z. Cemin, L. Song, and A. E. Fathy, "Development of an ultra wideband vivaldi antenna array," in *IEEE Antennas and Propagation Society International Symposium and USNC/URSI Meeting*, vol. 1 A, pp. 606–609, Washington, DC, USA, July 2005.

[11] J. D. S. Langley, P. S. Hall, and P. Newham, "Balanced antipodal Vivaldi antenna for wide bandwidth phased arrays," *IEE Proceedings: Microwaves, Antennas and Propagation*, vol. 143, no. 2, pp. 97–102, 1996.

[12] J. A. N. Noronha, T. Bielawa, C. R. Anderson, D. G. Sweeney, S. Licul, and W. A. Davis, "Designing antennas for UWB systems," *Microwaves and RF*, vol. 42, no. 6, pp. 53–61, 2003.

[13] E. Gazit, "Improved design of the Vivaldi antenna," *IEE Proceedings H: Microwaves, Antennas and Propagation*, vol. 135, no. 2, pp. 89–92, 1988.

[14] N. Fourikis, N. Lioutas, and N. V. Shuley, "Parametric study of the co- and crosspolarization characteristics of tapered planar and antipodal slotline antennas," *IEE Proceedings H: Microwaves, Antennas and Propagation*, vol. 140, no. 1, pp. 17–22, 1993.

[15] M. C. Greenberg, K. L. Virga, and C. L. Hammond, "Performance characteristics of the dual exponentially tapered slot antenna (DETSA) for wireless communications applications," *IEEE Transactions on Vehicular Technology*, vol. 52, no. 2, pp. 305–312, 2003.

[16] K. S. Yngvesson, D. H. Schaubert, T. L. Korzeniowski, E. L. Kollberg, T. Thungren, and J. F. Johansson, "Endfire tapered slot antennas on dielectric substrates," *IEEE Transactions on Antennas and Propagation*, vol. 33, no. 12, pp. 1392–1400, 1985.

[17] "XFDTD version 6.1," Remcom, Inc., Pennsylvania USA.

[18] IE3D version 11, *Zeland Software, Inc.*, Fremont, Calif, USA.

Hindawi Publishing Corporation
International Journal of Antennas and Propagation
Volume 2008, Article ID 713921, 7 pages
doi:10.1155/2008/713921

Research Article

Printed UWB Antenna with Coupled Slotted Element for Notch-Frequency Function

X. L. Bao and M. J. Ammann

Centre for Telecommunications Value-Chain Research (CTVR), School of Electronic and Communications Engineering, Dublin Institute of Technology, Kevin Street, Dublin 8, Ireland

Correspondence should be addressed to M. J. Ammann, max.ammann@dit.ie

Received 30 April 2007; Revised 19 November 2007; Accepted 24 January 2008

Recommended by James Becker

A novel printed monopole antenna employing a slotted-plate, which is electromagnetically coupled to the microstrip-fed planar element, is proposed to provide notch-frequency function. This technique enables stopband characteristics with improved control, compared to placing the slot in the microstrip-fed element. A detailed investigation of the rejectband properties has been made for the UWB antenna. Measured data for the optimized case show the 10 dB return loss bandwidth to be 9.8 GHz (from 2.80 GHz to 12.60 GHz) with a notchband frequency from 5.15 GHz to 5.825 GHz. Propagation measurements indicate that the electromagnetically coupled slot provides a greater reduction in stopband gain for the three principal planes, compared to placing the slot in the fed element. This is desirable to mitigate interference from WLAN systems. A full parametric study of the antenna is presented.

1. INTRODUCTION

Ultrawideband (UWB) antennas have commanded increased interest in the last 4 years, due to the rapid development of wideband wireless communication systems. The planar monopole antenna is one of the candidate antennas proposed, due to low-cost, broad bandwidth, and attractive profile. These antennas have been reported with many various shaped planar elements, such as rectangular, disc, elliptical and triangular geometries [1–6]. Most UWB systems currently operate as Mode 1 devices, with an allocated spectrum from 3.1 GHz to 4.8 GHz. However, as demand increases, and the limitations in silicon technology are surpassed, the higher bands will become more populated. For these UWB systems, it may be necessary to provide rejection of interference from 802.11a WLAN or Unlicensed-National Information Infrastructure (U-NII), in the band from 5.15 GHz to 5.825 GHz. Thus, the provision of a narrow rejectband in the UWB allocated spectrum is desirable. Printed antennas with notch function have recently been reported [7–9], where various shaped narrow slots are embedded into the planar radiator to obtain the notch-frequency function. In [7–9], either U or H-shaped slots are embedded in the radiator element to obtain notchband frequencies. A different approach is to use parasitic elements which are coupled to the planar radiating element to provide the notch function [10]. An alternative method to provide the notch function is using a novel coplanar waveguide resonant cell in the CPW feedline as a narrow stopband filter [11]. In this technique, control of the notch bandwidth is more difficult due to the small dimensions involved. The proposed antenna differs from [7–9] because the H-slot is coupled to the planar radiator and is easier to tune. In comparison with [10], the proposed antenna provides better stopband rejection. Employing the filter into the antenna geometry can provide some stopband suppression with the advantages of low cost and zero passband insertion loss. This can be used alone or to complement additional filter circuitry where required.

In this paper, the notching function is provided by adding an extra slotted plate which is electromagnetically coupled to the microstrip-fed planar element, yielding greater stopband rejection. It is printed on the rear side of the substrate and provides the notch-reject function. The parameters of the slot and the coupled-plate are analysed in terms of the notch-frequency and bandwidth. A compact optimized UWB antenna with notch-frequency function was then fabricated

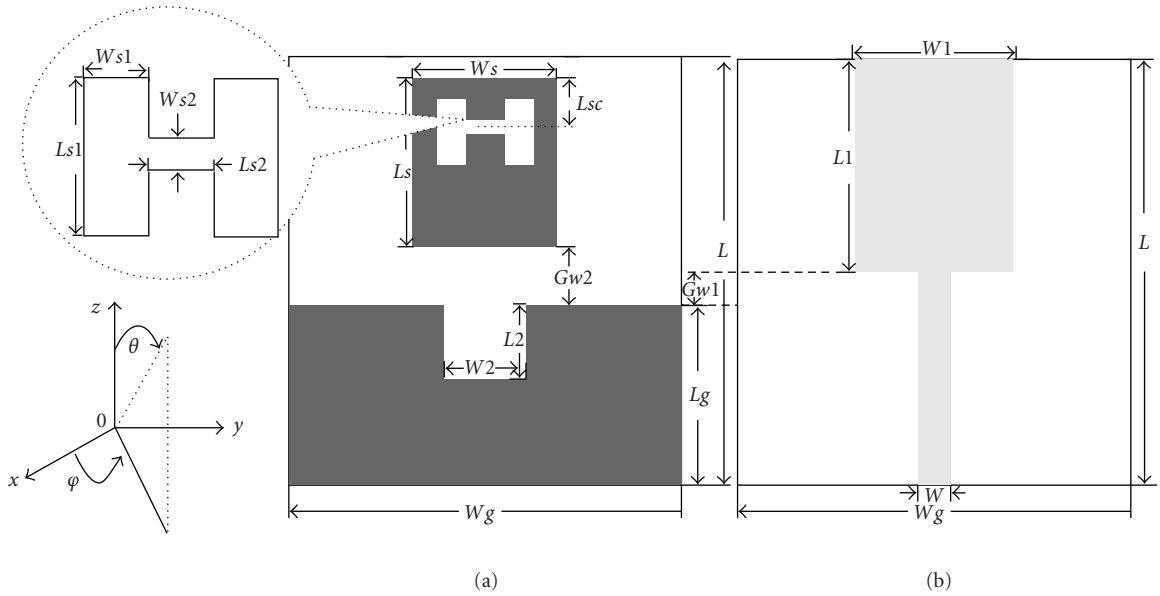

Figure 1: Geometry of the printed rectangular monopole antenna showing coupled element and coordinate system: (a) rear side showing groundplane and coupled element with H-slot, (b) front side showing microstrip-fed planar monopole.

and examined both experimentally and numerically. The measured results show that the proposed UWB antenna can achieve good impedance bandwidth characteristics, with improved control of bandnotch function.

2. NUMERICAL RESULTS FOR THE PRINTED MONOPOLE ANTENNA WITH SLOTTED-PLATE COUPLED TO RADIATOR-PLATE

The geometry and coordinate system for the proposed printed monopole antenna fed by a 50 ohm microstrip line is shown in Figure 1. It is printed on a Taconic RF35 substrate with a thickness of 1.52 mm, relative permittivity of 3.5, and a loss tangent of 0.0018. The width of microstrip feed line is fixed at 3.5 mm to achieve a 50 ohm impedance. A rectangular plate with a length $L1$ and width $W1$ is connected to the 50 ohm microstrip line. The substrate is of length L and width Wg. The ground plane has dimensions Lg and Wg. A section of groundplane of width $W2$ and length $L2$ is removed in order to improve the matching and also slightly reduces the lower-edge frequency [12]. The radiator plate is separated from the groundplane by a distance $Gw1$. The simulation was carried out using the Finite-Integration Time-Domain technique (CST MWS). The optimized printed monopole antenna dimensions are as follows: L = 28 mm, Wg = 30 mm, $L1$ = 16.5 mm, $W1$ = 12 mm, $L2$ = 4 mm, $W2$ = 3 mm, $Gw1$ = 1.5 mm, Lg = 10 mm.

To realise the proposed UWB antenna with the narrow rejectnotch band, a rectangular element is placed on the rear of the substrate and couples to the microstrip-fed plate. The H-shaped slot is removed from this rear plate as shown in Figure 1(a). The centre-frequency and width of rejected-frequency band are mainly determined by the size of H-shaped slot, its location in the coupled-plate, and the distance $Gw2$ between the coupled-plate and groundplane edge. The effects of various parameters of the H-shaped slot are discussed below. In this case, the rear plate size is selected at Ls = 12 mm and Ws = 12 mm, and an appropriate H-slot is removed from this plate to achieve the required function.

3. TUNING OF NOTCH FREQUENCY

A parametric study was made, and a set of design rules to tune the notch centre-frequency and control the notch bandwidth is presented.

3.1. The effect of the separation between coupled-plate and groundplane Gw2

The separation distance $Gw2$ between the coupled-plate and the groundplane was varied, and results show heavy dependence of the notch bandwidth on this parameter as shown in Figure 2. The dimensions of the H-shaped slot were $Ls1$ = 4 mm, $Ws1$ = 1.4 mm, $Ls2$ = 3 mm, $Ws2$ = 0.6 mm, and Lsc = 3 mm. It can be seen that as the separation $Gw2$ increases, the rejected-frequency band becomes much narrower. However, the improvement diminishes after a point and for this antenna requirement. In order to increase the bandwidth of the notch, the separation distance $Gw2$ should be reduced.

3.2. The effect of the distance of slot from the plate edge

The distance Lsc was varied from 3 mm to 9 mm for H-slot dimensions of $Ls1$ = 4 mm, $Ws1$ = 1.4 mm, $Ls2$ = 3 mm, $Ws2$ = 0.6 mm, and $Gw2$ = 3 mm. The simulated results show that only a small (0.5%) shift in notch frequency took place with no other significant changes.

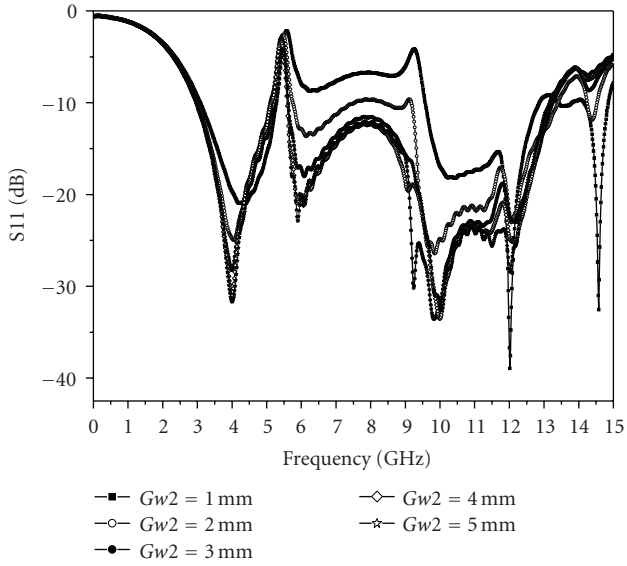

Figure 2: The simulated S11 for different values of *Gw*2.

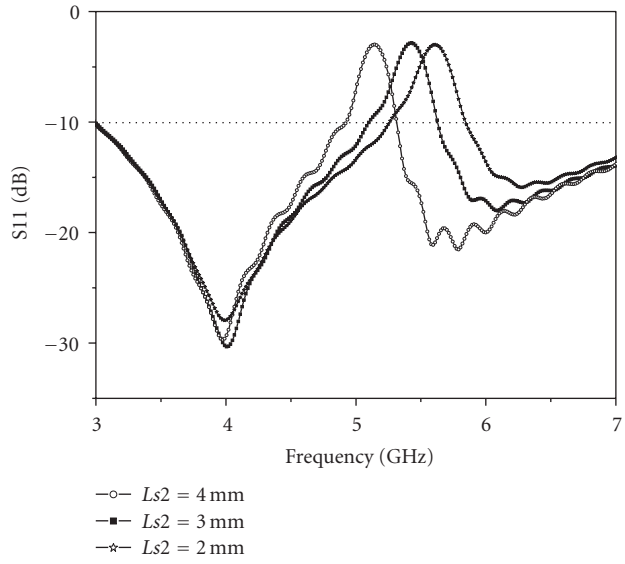

Figure 3: Simulated S11 showing notch dependence on *Ls*2.

3.3. The effect of slot dimensions Ws2 and Ls2

The slot dimensions *Ws*2 and *Ls*2, were varied, for *Ls*1 = 4 mm, *Ws*1 = 1.5 mm, *Gw*2 = 3 mm, *L*sc = 3 mm, and *Ls2* = 3 mm. It was observed that the bandwidth and notch-frequency show no dependence on *Ws*2, but that as *Ls*2 increases, the centre-frequency is reduced the reject bandwidth remaining constant.

Figure 3 illustrates the return loss for variation of the dimension *Ls*2 (*Ws*2 = 0.6 mm).

3.4. The effect of the slot length and width

The return loss curves in Figure 4 illustrate that the slot length *Ls*1 has a smaller effect on notch frequency than the parameter *Ls*2, (*Ws1* = 1.5 mm), and Figure 5 shows that the centre-frequency of the stopband shifts down as the slot width *Ws*1 increases. Here, *Ls*2 = 3 mm, *Ws*2 = 0.6 mm,

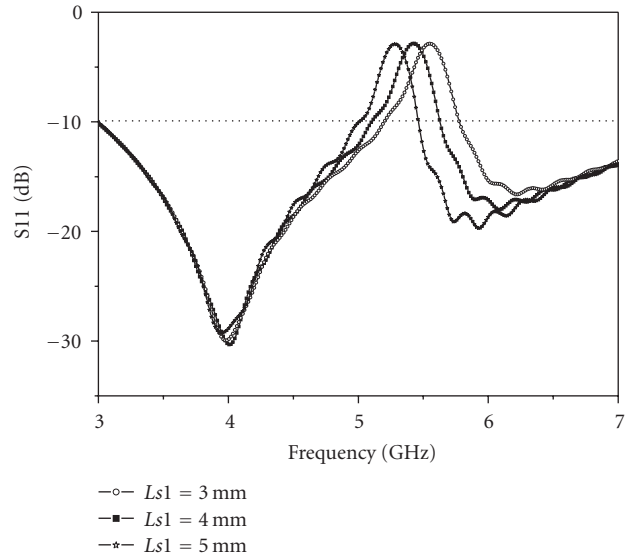

Figure 4: Simulated S11 showing notch dependence on *Ls*1.

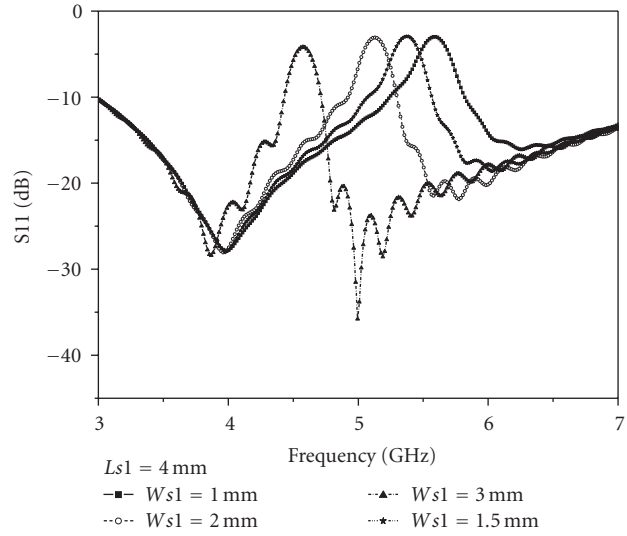

Figure 5: Simulated S11 showing notch dependence on *Ws*1.

Table 1: The effects of H-slot parametric variation on stopband centre-frequency and bandwidth.

Parameters	Stopband centre-frequency	Stopband bandwidth
Ls1	Light dependence	Constant
Ls2	Light dependence	Constant
Ws1	Heavy dependence	Constant
Ws2	No dependence	Constant
*L*sc	Light dependence	Light dependence
Gw2	Light dependence	Heavy dependence

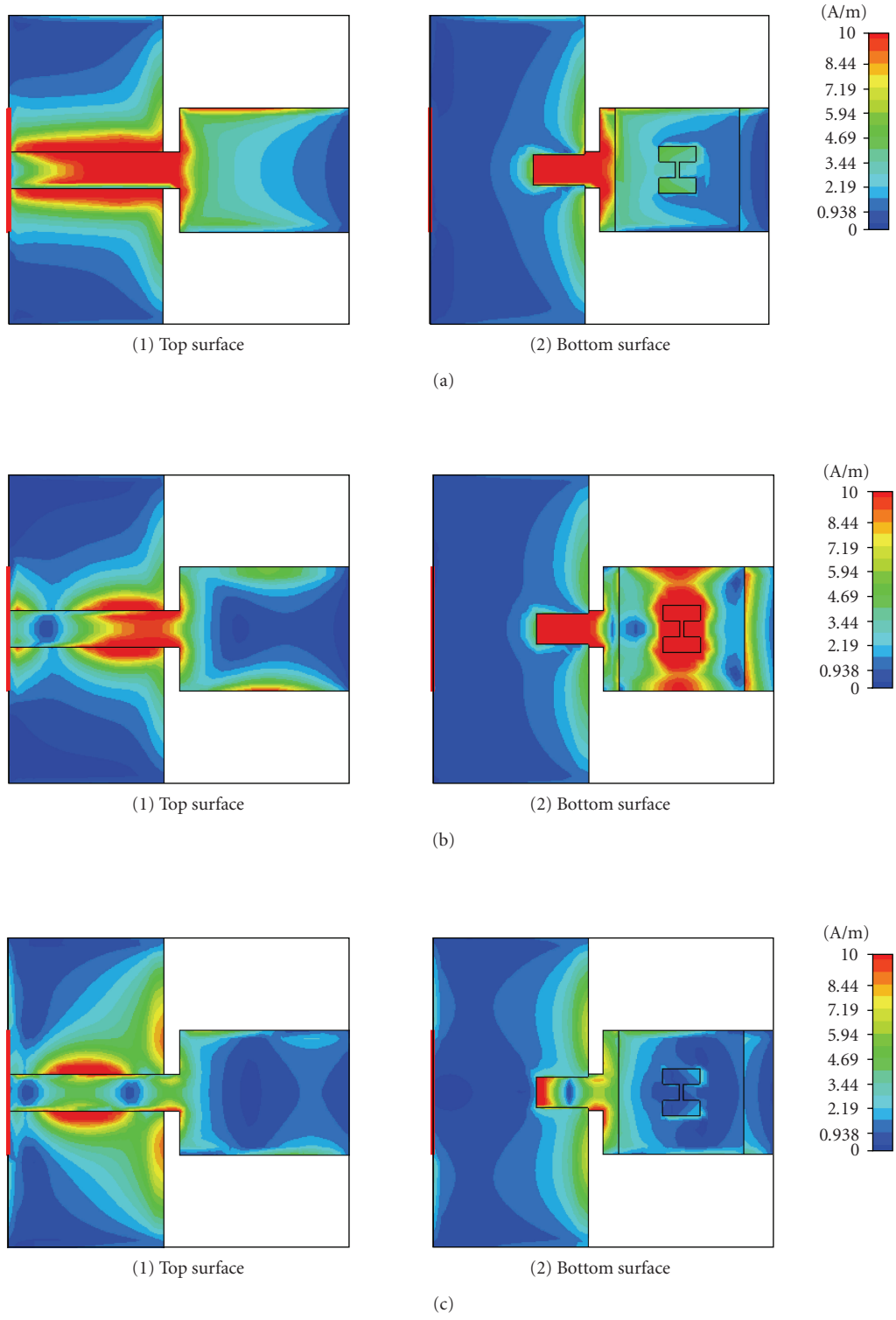

Figure 6: (a) The distribution of surface current at 3 GHz, (b) the distribution of surface current at 5.55 GHz, (c) the distribution of surface current at 8 GHz.

$Gw2$ = 3 mm, and Lsc = 3 mm. The notch frequency is heavily dependent on this parameter. The effects of H-slot parametric variation on the reject centre-frequency and bandwidth are displayed in Table 1.

The distributions of surface current are simulated by using CST microwave studio software, as shown in Figures 6(a), 6(b), and 6(c). It is noted that surface current distributions on the edges of the rectangular plate and groundplane

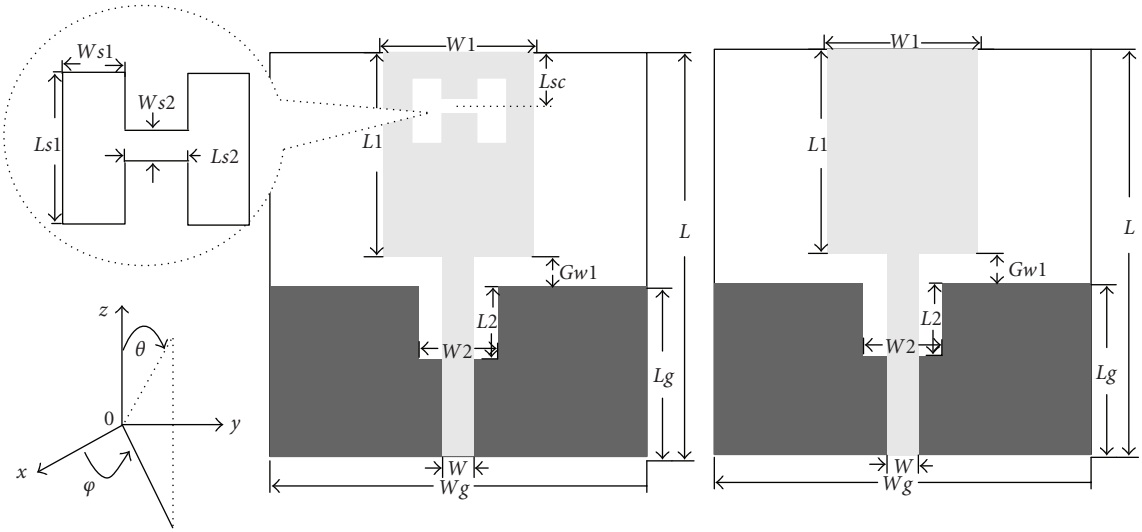

Figure 7: (a) Simple rectangular UWB monopole geometry, (b) rectangular monopole with H-slot in microstrip-fed element.

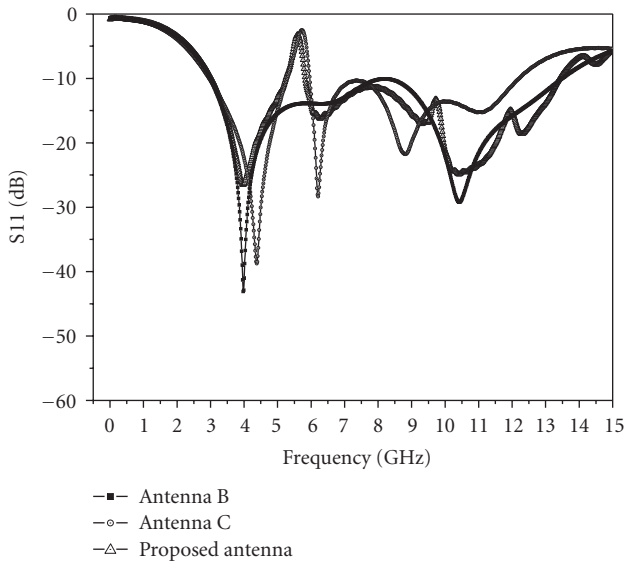

Figure 8: Comparison of simulated S11 for the three planar UWB antennas.

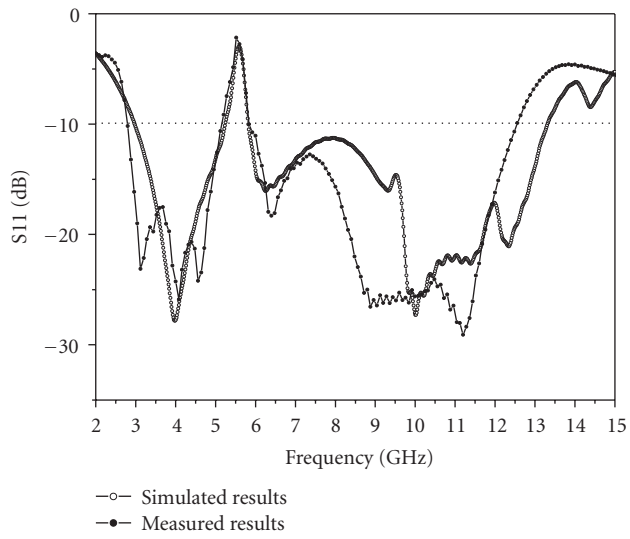

Figure 9: Comparison of the measured and simulated S11 for the proposed antenna.

are very strong. It was also observed that the surface current distributions at the edges of the H-slot are very strong at the notchband frequency of 5.55 GHz, but weak at other frequencies. This is because the H-slot shape is highly resonant at the notch frequency.

4. COMPARISON OF PROPOSED ANTENNA PERFORMANCE WITH OTHER RECTANGULAR PLANAR UWB ANTENNAS

The proposed antenna with coupled slotted plate (Figure 1, antenna A) is now compared to two other antennas, one with a simple microstrip-fed rectangular monopole (antenna B, without notch function) and the other with the slots in the microstrip-fed element (antenna C) as shown in Figures 7(a) and 7(b), respectively. The basic parameters were kept the same for all 3 antennas as follows: L = 33 mm, Wg = 30 mm, $L1$ = 16.5 mm, $W1$ = 12 mm, $L2$ = 4 mm, $W2$ = 3 mm, $Gw1$ = 1.5 mm, and Lg = 15 mm. The same substrate was used; Taconic RF35 with relative permittivity of 3.5 and thickness of 1.52 mm. For the antenna with the H-shape slot in the microstrip-fed element (Figure 7(b), antenna C), the other optimized dimensions are Lsc = 2.25 mm, $Ls1$ = 4 mm, $Ws1$ = 2.5 mm, Ls = 4 mm, and Ws = 0.3 mm. For the antenna with

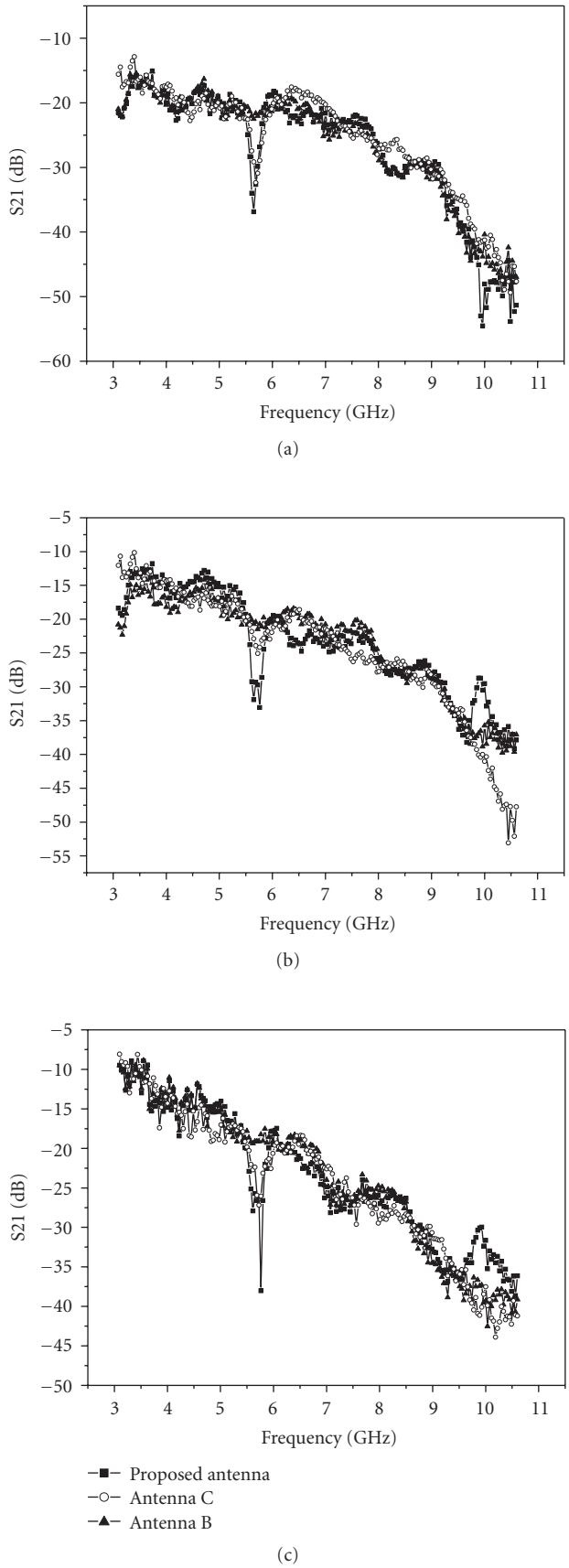

Figure 10: The measured S21 for the three antennas in the *x*, *y*, and *z* directions.

the coupled slotted plate (Figure 1, antenna A), the H-shape parameters are selected in $Ws = 12$ mm, $Ls = 12$ mm, $Gw2 = 3$ mm, $Lsc = 3$ mm, $Ls1 = 4$ mm, $Ws1 = 1$ mm, $Ls2 = 3$ mm, and $Ws2 = 0.6$ mm. The substrate had a width of 30 mm and length of 28 mm in each case. The simulated results of S11 for three antennas are shown in Figure 8. It is seen that both antenna A and antenna C show a notchband between 5.15 GHz and 5.825 GHz in the response.

Compared to the rectangular UWB, printed antenna with the H-shaped slot in the microstrip-fed element shown as Figure 7(b) (antenna C), this new proposed UWB antenna is much more convenient to tune the notch frequency and bandwidth by changing the H-slot dimensions, independent of the other antenna dimensions. This is in contrast to tuning the H-slot in the microstrip-fed planar element, which necessitates a change in the dimensions of the planar element, thus changing the overall S11 response, and requiring an iteration in the design.

Also, the proposed antenna can provide a deeper drop in notch gain.

5. MEASUREMENTS OF THE PROPOSED ANTENNA

Figure 9 presents the simulated and measured return losses for the proposed antenna, which are in good agreement. The measured 10 dB return loss impedance bandwidth is about 9.8 GHz from 2.80 GHz to 12.60 GHz with the narrow notch-frequency band from 5.15 GHz to 5.825 GHz.

The S21 was measured for the three antennas in the *x*, *y*, and *z* directions as illustrated in Figure 10. The illuminating antenna was a wideband horn antenna. It is observed that the proposed antenna has the greatest reduction in notchband gain, therefore providing better notch rejection.

The CW gain pattern is shown in Figure 11, which is determined from the directional measured transfer function. The plots in Figures 11(a) and 11(b) illustrate the measured patterns for the *XoZ* and *XoY,* planes for the UWB frequency range (from 3.1 GHz to 11 GHz), respectively. These results show the power distributions in the 3D space against frequency. The notch can be clearly seen. The measured group delay for the three UWB antennas is displayed in Figure 12, which show that the group delay is reasonably constant within about 1nanosecond except for the notchband. It shows that the antenna has low-impulse distortion and is suitable for UWB applications.

6. CONCLUSIONS

A notch-frequency band for an UWB antenna is obtained by employing a slotted coupled-plate. The effects of antenna parameters on the notch bandwidth and centre frequency are presented in detail. The measured results are in agreement with the simulated results. This parametric study is valuable in the design of wideband compact antennas with a narrow notched-band. The novel notchband UWB antenna provides easier tuning of the notch-frequency function and bandwidth with good stopband rejection. Group delay and radiation characteristics are appropriate for this application.

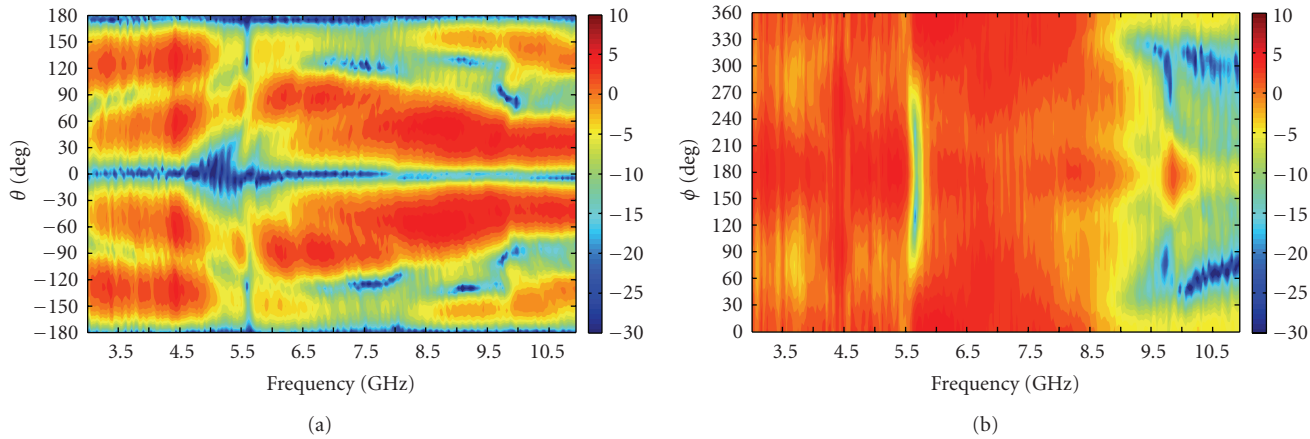

Figure 11: The measured copolar gain of the proposed antenna plotted against frequency for the principla planes: (a) *XoZ*, (b) *YoZ*.

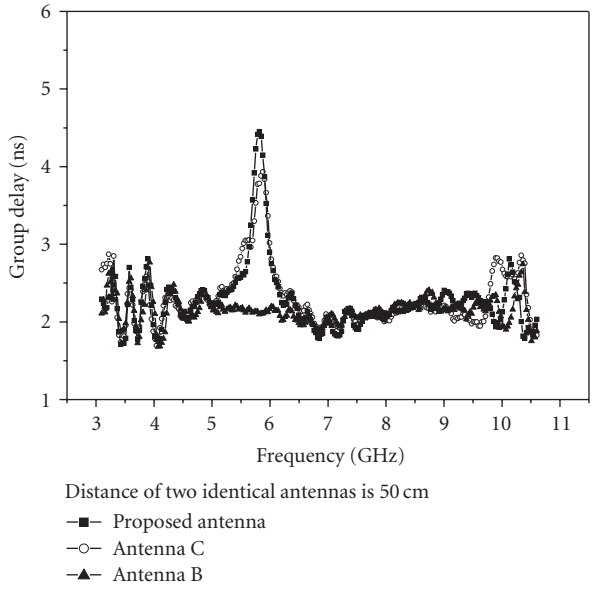

Figure 12: The measured group delay for the three UWB antennas.

ACKNOWLEDGMENT

This work is supported by Science Foundation, Ireland.

REFERENCES

[1] C.-Y. Huang and W.-C. Hsia, "Planar elliptical antenna for ultra-wideband communications," *Electronics Letters*, vol. 41, no. 6, pp. 296–297, 2005.

[2] C.-C. Lin, Y.-C. Kan, L.-C. Kuo, and H.-R. Chuang, "A planar triangular monopole antenna for UWB communication," *IEEE Microwave and Wireless Components Letters*, vol. 15, no. 10, pp. 624–626, 2005.

[3] M. J. Ammann and M. John, "Optimum design of the printed strip monopole," *IEEE Antennas and Propagation Magazine*, vol. 47, no. 6, pp. 59–61, 2005.

[4] J. Liang, L. Guo, C. C. Chiau, X. Chen, and C. G. Parini, "Study of CPW-fed circular disc monopole antenna for ultra wideband applications," *IEE Proceedings: Microwaves, Antennas and Propagation*, vol. 152, no. 6, pp. 520–526, 2005.

[5] W. Qiao, Z. N. Chen, and K. Wu, "UWB monopole antenna with a top-hat sleeve," *International Journal of Microwave and Optical Technology*, vol. 1, no. 1, 2006.

[6] Z. N. Chen, T. S. P. See, and X. Qing, "Small printed ultra-wideband antenna with reduced ground plane effect," *IEEE Transactions on Antennas and Propagation*, vol. 55, no. 2, pp. 383–388, 2007.

[7] W. J. Lui, C. H. Chehg, Y. Cheng, and H. Zhu, "Frequency notched ultra-wideband micro-strip slot antenna with fractal tuning stub," *Electronics Letters*, vol. 41, no. 6, pp. 294–296, 2005.

[8] W.-C. Liu and P.-C. Kao, "CPW-FED triangular antenna with a frequency-band notch function for ultra-wide band application," *Microwave and Optical Technology Letters*, vol. 48, no. 6, pp. 1032–1035, 2006.

[9] K. Chung, J. Kim, and J. Choi, "Wideband microstrip-fed monopole antenna having frequency band-notch function," *IEEE Microwave and Wireless Components Letters*, vol. 15, no. 11, pp. 766–768, 2005.

[10] K.-H. Kim and S.-O. Park, "Analysis of the small band-rejected antenna with the parasitic strip for UWB," *IEEE Transactions on Antennas and Propagation*, vol. 54, no. 6, pp. 1688–1692, 2006.

[11] S. W. Qu, J. L. Li, and Q. Xue, "A band-notched ultra-wideband printed monopole antenna," *IEEE Antennas and Wireless Propagation Letters*, vol. 5, no. 1, pp. 495–498, 2006.

[12] X. L. Bao and M. J. Ammann, "Investigation on UWB printed monopole antenna with rectangular slitted groundplane," *Microwave and Optical Technology Letters*, vol. 49, no. 7, pp. 1585–1587, 2007.

Hindawi Publishing Corporation
International Journal of Antennas and Propagation
Volume 2008, Article ID 410786, 7 pages
doi:10.1155/2008/410786

Research Article

UWB Directive Triangular Patch Antenna

A. C. Lepage,[1] X. Begaud,[1] G. Le Ray,[2] and A. Sharaiha[2]

[1] *GET/Télécom Paris, CNRS UMR 5141, 46 rue Barrault, 75634 Paris Cedex 13, France*
[2] *IETR, CNRS UMR 6164, Université de Rennes 1, Groupe Antennes et Hyperfréquences, Bâtiment 11D, 35042 Rennes Cedex, France*

Correspondence should be addressed to A. C. Lepage, anne-claire.lepage@enst.fr

Received 1 May 2007; Accepted 21 October 2007

Recommended by Dejan Filipovic

Compact directive UWB antennas are presented in this paper. We propose an optimization of the F-probe fed triangular patch antenna. The new design achieves an impedance bandwidth of 69% (3–6.15 GHz) and presents good radiation characteristics over the whole impedance bandwidth. The average gain is 6.1 dB. A time-domain study has been performed to characterize the antenna behavior in case a UWB pulse is used. Finally, we propose an alternative solution to facilitate the manufacturing process using metallized foam technology. It also improves the robustness of the antenna as well as reducing its cost.

1. INTRODUCTION

One of the key issues of the emerging ultra-wide band (UWB) technology is the design of low cost compact antennas.

Many researches are focused on omnidirectional antennas because their wide beamwidth enables to communicate with radio elements whatever their position is.

But directional antennas also present some interest. In fact, on the transmitter side, even if regulation authorities have limited the effective isotropic-radiated power (EIRP), the use of directional antennas enables to reduce radiation in undesired directions and thus improves power consumption. On the receiver side, the antenna gain adds a few and precious dB in the link budget.

Concerning the applications, directional antennas could be placed on a wall or implemented in a sectorized radio topology (radio-access point) or in a terminal using multiple directive antennas (antenna diversity). It is also possible for some specific applications that the user points the antenna in the desired direction, for example, for a fast download between his terminal and a PC.

With their low thickness, conformability, compactness and low cost, microstrip antennas are very attractive for such applications, but they suffer from their inherently narrow bandwidth. In order to solve this problem, a well-known technique consists in using low permittivity and thick substrate.

The extreme case is using the air as the substrate. This solution will maximize the size of the structure. However, it remains attractive for some applications as the antenna is still compact.

It has been demonstrated in [1] that increasing the thickness of the substrate induces an inductive effect on input impedance which can be offset by adding a capacitance to obtain a wide-band behavior.

Thus, the L-shaped probe proposed in [2] to feed the patch by electromagnetic coupling enables to widen the bandwidth. A triangular patch fed by an L-shaped probe achieves 42% impedance bandwidth and a maximum gain of 6 dBi [3]. An F-shaped probe rectangular patch antenna with an impedance bandwidth of 64% has also been designed in [4] but the radiation pattern was not stable over the bandwidth due to the excitation of successive radiating modes of the patch.

In [5], we have proposed a triangular patch fed by an F-shaped probe. This new structure has stable radiation pattern over the impedance bandwidth of 47%, from 3.1 to 5 GHz.

In this paper, we present an improvement of this antenna with a wider bandwidth.

We also propose an alternative solution to manufacture the probe and the patch using metallized foam technology in order to improve its reproducibility and reduce its cost.

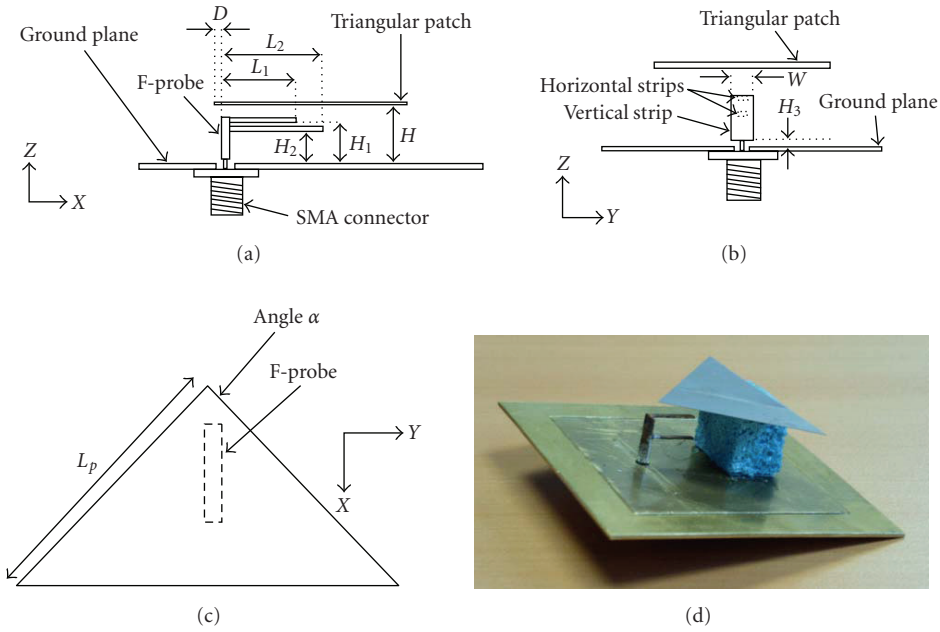

Figure 1: Geometry of the antenna and prototype.

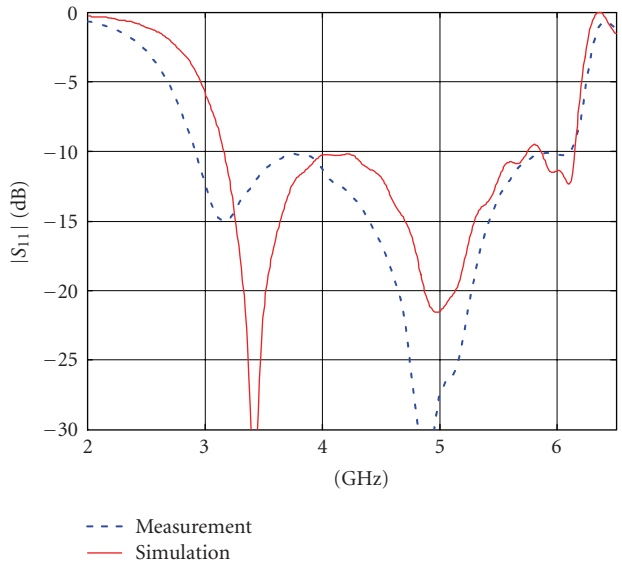

Figure 2: Measured and simulated reflection coefficient magnitude $|S_{11}|$ versus frequency.

2. DESCRIPTION OF THE F-PROBE ANTENNA

The geometry of the antenna is presented in Figure 1. The F-probe is made of a bended 0.2 mm thick metallic rectangular strip on which a second strip has been welded. The whole is welded to an SMA connector whose central conductor goes through the square ground plane.

The radiating element is an isosceles triangle cut out of a steel sheet which is electromagnetically fed by the F-probe. The triangular shape has been chosen because it has been demonstrated in [6] that three of the five first modes (TM_{10}, TM_{20}, and TM_{21}) present similar radiation pattern, polarization, and input impedance. The triangle is centered above the ground plane and supported by a foam layer; it has been verified to have a permittivity close to the air.

Dimensions of the structure are as follows: $L_p = 36$ mm, $D = 0.6$ mm, $H_3 = 0.4$ mm, $\alpha = 84°$, $H = 14.9$ mm, $H_1 = 10.05$ mm, $H_2 = 5.6$ mm, $L_1 = 9.9$ mm, $L_2 = 10.8$ mm, $w = 3.6$ mm, horizontal strips width = 1.2 mm, ground plane size = 67×67 mm, probe thickness = 0.4 mm.

The antenna has been simulated with CST Microwave Studio software.

This optimized structure is the result of a parametric study which has demonstrated that it is possible to generate multiple resonances close to each other when the lengths of the horizontal strips of the probe are slightly different.

However, a capacitance effect caused mismatching. That is why we added an inductive effect on the probe by increasing the width of the vertical strip. Finally, the optimization has also been done on H, H_1, and H_2 to obtain a good impedance matching.

This new probe is different from the one presented in [5] whose strips had all the same width and very different lengths.

At the beginning of the study, the angle α value was 90°. But due to constraints concerning the length of the base of the triangle, the value of α has been reduced to 84°.

3. RESULTS AND ANALYSIS

3.1. Frequency-domain results

The simulated and measured return loss is presented in Figure 2. The measured bandwidth, defined for a reflection coefficient $|S_{11}|$ lower than −10 dB, reaches 69%

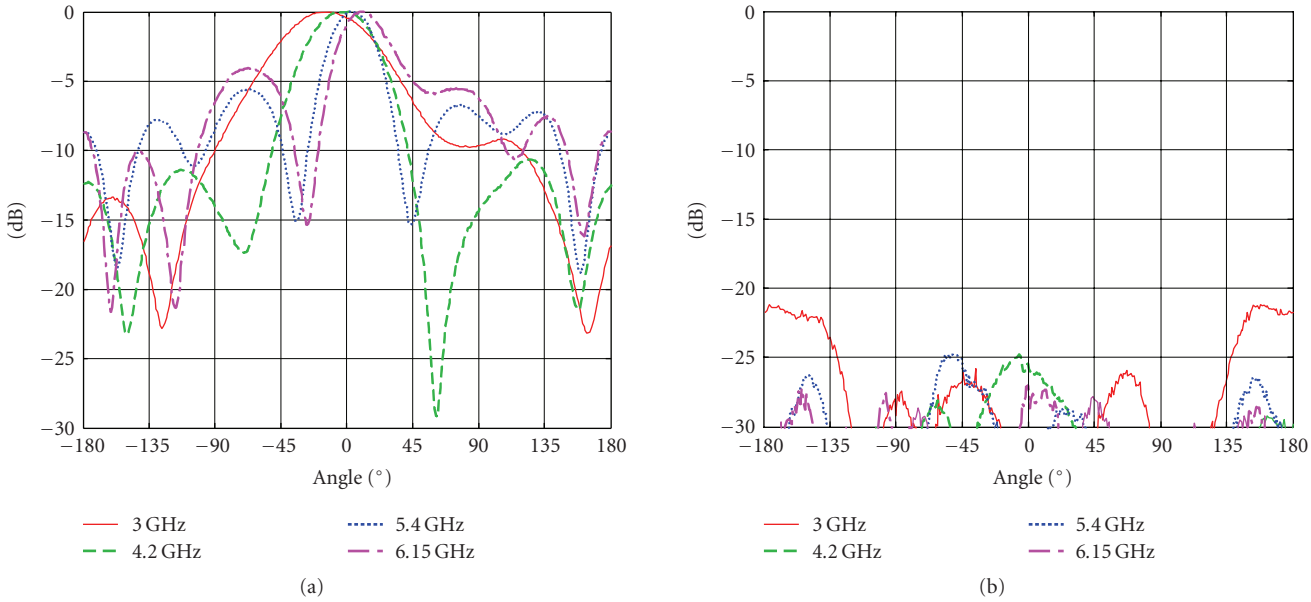

Figure 3: Radiation pattern in the E-plane.

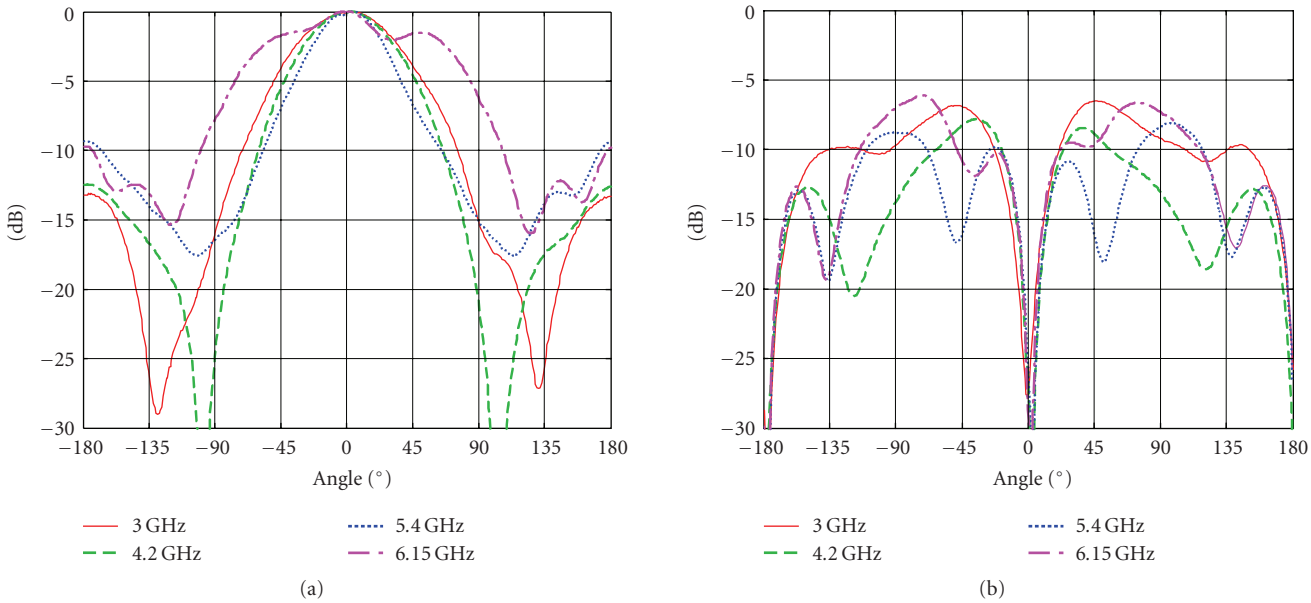

Figure 4: Radiation pattern in the H-plane.

(3.01–6.15 GHz). Good agreement between simulation and measurement is observed. And it has been demonstrated that the ground plane size has no influence on impedance matching. Figure 3 presents measured radiation pattern at different frequencies over the bandwidth in the E-plane (XZ plane) and Figure 4 in the H-plane (YZ plane).

Main lobe direction remains very stable in the H-plane and quite stable in the E-plane with a maximum variation of 15 degrees.

Cross-polarization level is very low in the E-plane and in the main lobe direction of the H-plane. In the H-plane, it is maximum (−6.7 dB) outside the main lobe for $\theta = \pm 82^\circ$ at 6.15 GHz.

Measured and simulated gains in the main lobe direction are presented in Figure 5.

Measured gain is quite stable up to 5.5 GHz and decreases at higher frequencies. Average measured gain is 6.1 dB.

Good agreement between simulation and measurement is observed except for highest frequencies, which requires new measurements.

The ground plane size influence on gain has also been studied.

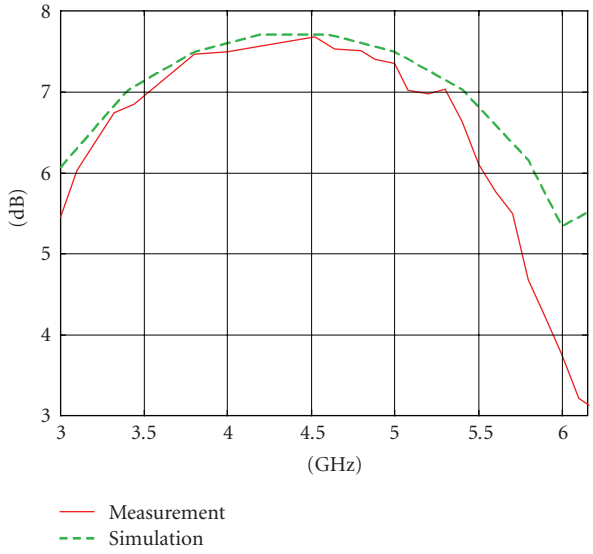

Figure 5: Comparison between simulated and measured gain in the main lobe direction over the bandwidth.

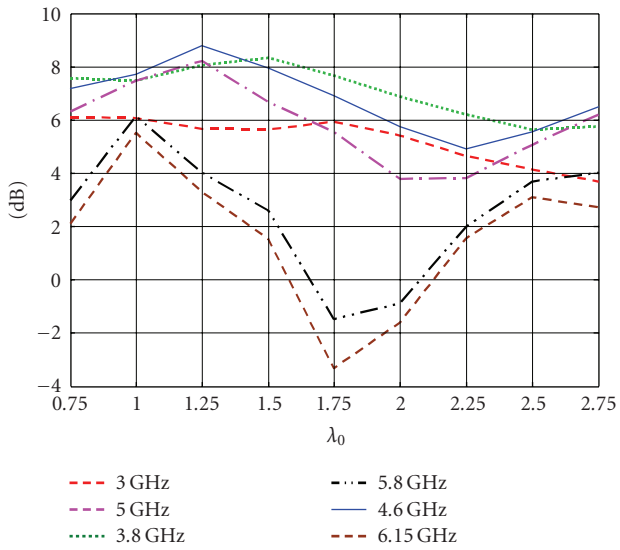

Figure 6: Gain in the main lobe direction as a function of the ground plane size at different frequencies. (λ_0 is the wavelength corresponding to the central frequency of the impedance bandwidth of the antenna).

Figure 6 presents the gain in the main lobe direction ($\theta = 0°$, $\varphi = 0°$) as a function of the ground plane size at different frequencies. It can be deduced that a ground plane size of λ_0 by λ_0 gives the smallest variation of the gain and the best average value over the bandwidth (λ_0 is the wavelength at $f = 4.58$ GHz). That is why we chose this size for the prototype.

3.2. UWB specific time- and frequency-domain analyses

Evaluation of input impedance, radiation pattern, and gain as a function of frequency is not sufficient in case of using time-domain modulation schemes, for example, pulse position modulation. The distortion of the pulse resulting from the dispersive nature of the antenna has also to be analyzed.

For this purpose, we measured the transfer function as a function of the angular coordinates using a reference antenna as described in [7].

Once it is determined, it is possible to calculate the radiated field.

We chose a Gaussian excitation impulse whose spectrum is presented in Figure 7. Figure 8 presents the excitation signal and the measured and simulated radiating field in the main lobe direction.

From Figure 8, we can observe very good agreement between simulation with CST Microwave Studio and the measurement. Although we remark some distortion, it seems to be moderate: the radiated pulse is not very different from the

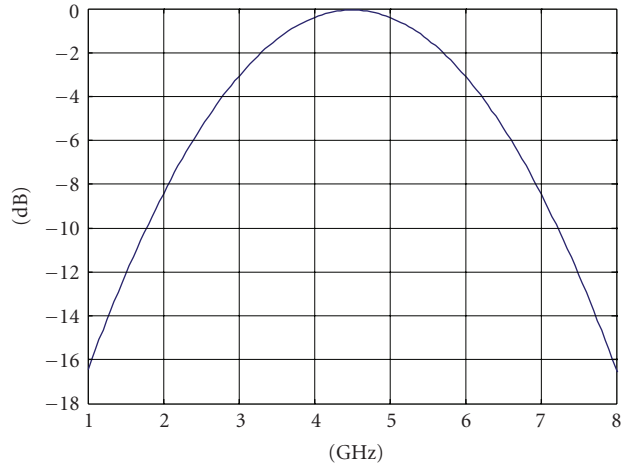

Figure 7: Spectrum of the excitation signal.

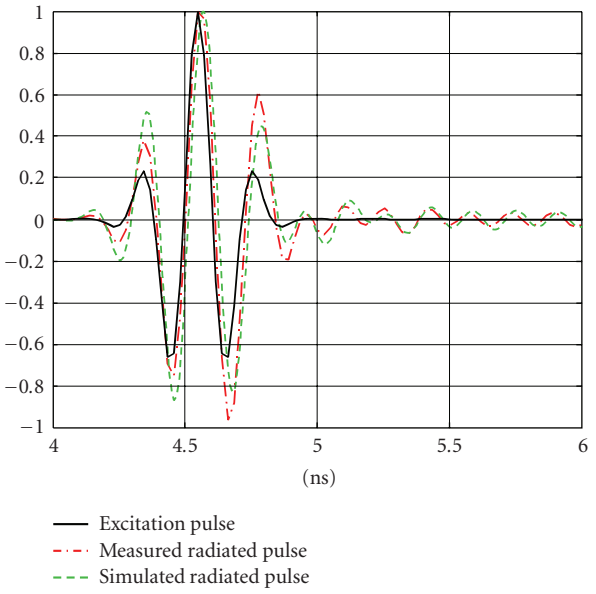

Figure 8: Excitation signal and radiated field in the main lobe direction.

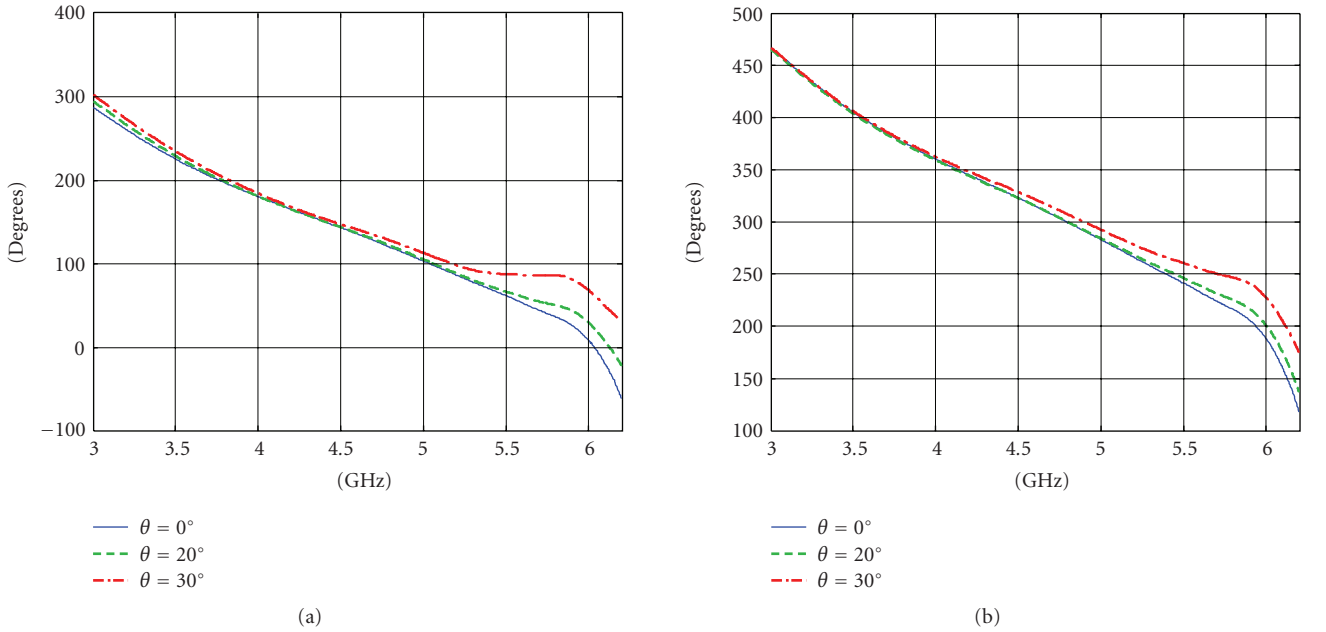

Figure 9: Simulated phase of the far-field (copolarization) in the E-plane (left) and in the H-plane at different angles in the main lobe.

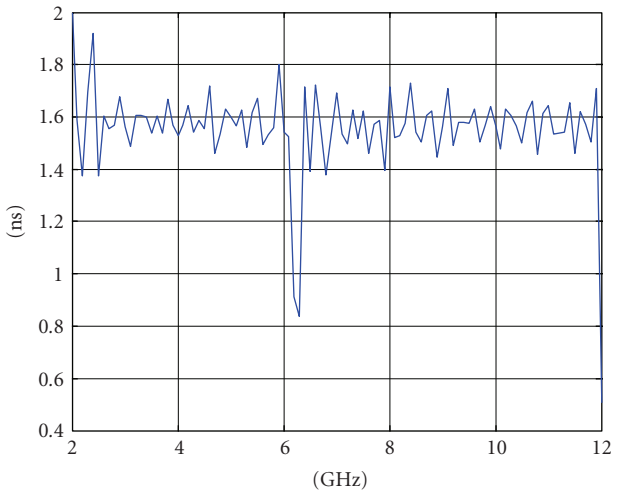

Figure 10: Group delay in the main lobe direction $\theta = 0°$ between 2 and 12 GHz.

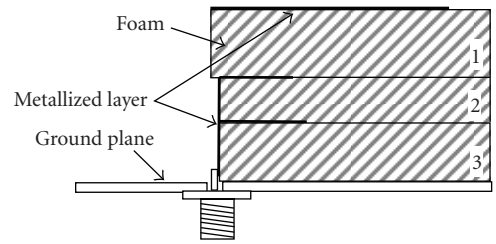

Figure 11: Structure of the antenna using metallized foam technology.

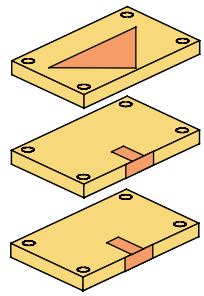

Figure 12: Metallized foam blocks before assembly.

excitation signal. It is a bit larger due to the fact that the antenna has filtered all frequencies outside its impedance bandwidth.

Figure 9 shows the evolution of the far-field phase (copolarization component) over the bandwidth for different values of elevation angle in the main lobe in the E- and H-planes. It is nearly linear which confirms low pulse distortion.

In order to quantify the phase linearity, we studied the group delay τ_g, defined in [8] as: $\tau_g = -(\partial\varphi/2\pi\partial f)$, where φ is the phase and f the frequency.

And the standard deviation of the group delay defined in [8] as $\sigma_{\text{gd}} = \sqrt{(1/\Delta f)\int_{f_1}^{f_2}(\tau_{\text{g}} - \overline{\tau_g})^2 df}$, where f_1 and f_2 are the boundaries of the impedance bandwidth Δf and $\overline{\tau_g}$ is the average group delay.

For the F-probe antenna, the standard deviation is under 250 ps over the beamwidth.

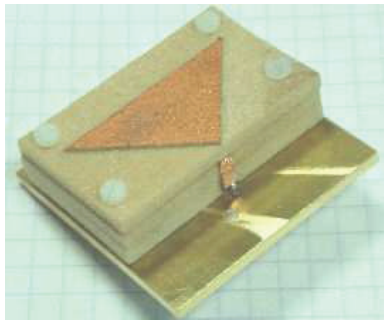

Figure 13: Triangular patch F-probe antenna using metallized foam technology.

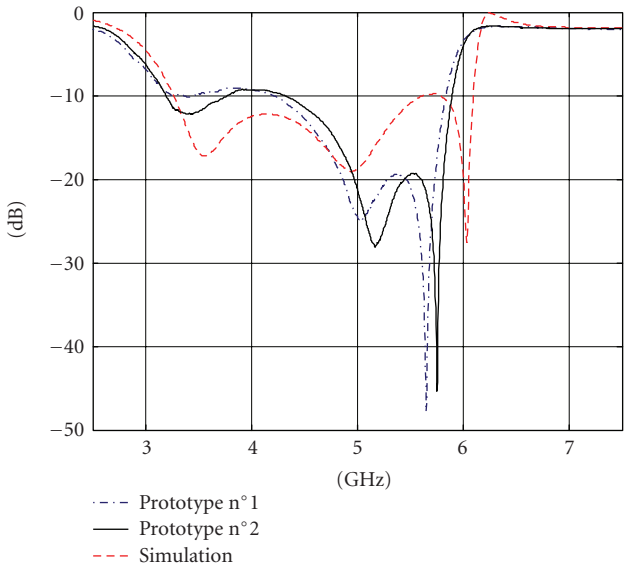

Figure 14: Measured and simulated reflection coefficient magnitude $|S_{11}|$ versus frequency.

4. F-PROBE ANTENNAS USING METALLIZED FOAM TECHNOLOGY

The F-probe triangular patch antenna presents interesting features. But one critical issue still persists: the difficulty of realization which is directly linked to the cost. In fact, the manufacturing of the F-probe is a real technological issue, especially the welding of the lower horizontal strip to the bended strip. Moreover, the robustness of the antenna has to be improved.

We retained an innovative solution developed at IETR (Institut d'Electronique et des Télécommunications de Rennes) which enables to metallize low-permittivity foam of arbitrary geometry [9].

Thus, we realized the antenna with a quite rigid foam whose electrical permittivity is 1.23.

Due to this new permittivity value, it has been necessary to resize the antenna. New dimensions are as follows: L_p = 32.5 mm, D = 0.6 mm, $\alpha = 84°$, H = 13.9 mm, H_1 = 9.7 mm, H_2 = 5.3 mm, L_1 = 9.1 mm, L_2 = 9.9 mm, w = 3.25 mm, horizontal strips width = 1.1 mm, ground plane size = 54 × 54 mm, metallization thickness = 0.02 mm.

The radiating patch and the F-probe are metallized on 3 different blocks of foam. (Figures 11 and 12): the triangle is metallized on the block n°1, the upper vertical part of the probe and the upper horizontal strip are on the block n°2 and the lower vertical part and the lower strip are metallized on the block n°3. As before, the ground plane is cut in a brass sheet. The SMA connector is welded to the vertical metallized part directly on the foam. The three blocks are screwed together and also to the ground plane with 4 nylon screws. (Figure 13).

In order to evaluate the reproducibility of the process, we realized two prototypes.

Figure 14 presents the measurement of the magnitude of the reflection coefficient for the two prototypes and the comparison with the simulation result.

First of all, results are similar for the two prototypes which demonstrate the good reproducibility of the manufacturing process.

The measured bandwidth reaches 58% (3.2–5.8 GHz).

The agreement between measurement and simulation is satisfying.

Due to space constraints, radiation patterns are not shown but they appear to be similar to those presented in Section 3.

Since the relative electric permittivity is 1.23, the gain value is similar to the one of the previous design.

The next step of improvement of the manufacturing of this antenna will be the metallization of the ground plane.

5. CONCLUSION

In this article, we have presented an optimization performed on the F-probe triangular patch antenna. The new design achieves an impedance bandwidth of 69% with a stable radiation pattern over the bandwidth and is quite compact ($\lambda_0 \times \lambda_0 \times 0.22\,\lambda_0$). A time domain study has also shown that the antenna distorts the excitation pulse in a moderate way.

A solution has also been proposed for an easier realization and a better robustness of the probe in the purpose of minimizing manufacturing costs and improving reproducibility.

At this time, this antenna is integrated in an industrial UWB test platform.

ACKNOWLEDGMENT

This work has been done in collaboration with the UEI-AAR laboratory of ENSTA, Paris, France.

REFERENCES

[1] D. H. Schaubert, D. M. Pozar, and A. Andrew, "Effect of microstrip antenna substrate thickness and permittivity: comparison of theories with experiment," *IEEE Transactions on Antennas and Propagation*, vol. 37, no. 6, pp. 677–682, 1989.

[2] K. M. Luk, C. L. Mak, Y. L. Chow, and K. F. Lee, "Broadband microstrip patch antenna," *Electronics Letters*, vol. 34, no. 15, pp. 1442–1443, 1998.

[3] C. L. Mak, K. M. Luk, and K. F. Lee, "Wideband triangular patch antenna," *IEE Proceedings: Microwaves, Antennas and Propagation*, vol. 146, no. 2, pp. 167–168, 1999.
[4] B. L. Ooi, C. L. Lee, and P. S. Kooi, "A novel F-probe-fed broadband patch antenna," *Microwave and Optical Technology Letters*, vol. 30, no. 5, pp. 355–356, 2001.
[5] A. C. Lepage and X. Begaud, "A compact ultrawideband triangular patch antenna," *Microwave and Optical Technology Letters*, vol. 40, no. 4, pp. 287–289, 2004.
[6] K. F. Lee, K. M. Luk, and J. S. Dahele, "Characteristics of the equilateral triangular patch antenna," *IEEE Transactions on Antennas and Propagation*, vol. 36, no. 11, pp. 1510–1518, 1988.
[7] H. Ghannoum, *Etude conjointe antenne/canal pour les communications ultra Large Bande en présence du corps humain*, Ph.D. thesis, ENST, Paris, France, 2006.
[8] C. Roblin, S. Bories, and A. Sibille, "Characterization tools in the time domain," in *Proceedings of International Workshop on Ultra Wideband Systems (IWUWBS '03)*, Oulu, Finland, June 2003.
[9] S. Chainon and M. Himdi, "2D and 3D metallized foam technology applied to conformal antennas," in *Proceedings of the 3rd Workshop on Conformal Antennas*, Bonn, Germany, October 2003.

Hindawi Publishing Corporation
International Journal of Antennas and Propagation
Volume 2008, Article ID 129584, 11 pages
doi:10.1155/2008/129584

Research Article

Single and Multiple Scattering in UWB Bicone Arrays

Raffaele D'Errico[1,2] and Alain Sibille[1]

[1] *ENSTA, 32 Boulevard Victor, 75739 Paris Cedex 15, France*
[2] *DEIS, Facoltà di Ingegneria, Via del Risorgimento 2, 40100 Bologna, Italy*

Correspondence should be addressed to Raffaele D'Errico, raffaele.derrico@ensta.fr

Received 1 May 2007; Revised 12 September 2007; Accepted 29 December 2007

Recommended by Dejan Filipovic

An analysis of interactions between radiators in a UWB biconical array, drawing attention to single and multiple scatterings, is carried out. The complementarity between electrical coupling and radiation scattering is argued. The point source approximation is discussed and shown to be insufficient. An approximation of radiation scattering based on angular averaging of the scattering coefficient is proposed. This approach yields a reduction of the problem complexity, which is especially interesting in UWB multiple antenna systems, because of the large bandwidth. Multiple scattering between radiators is shown to be a second-order effect. Finally, a time domain approach is used in order to investigate pulse distortion and quantify the exactness of the proposed scattering model.

1. INTRODUCTION

It is well known that multiple antenna system (MAS) offers attractive applications in wireless communications by means of MIMO techniques that give out high channel capacities, by taking benefit of antenna diversity at both ends of the link. Furthermore, ranging applications may take advantage from MAS, through direction-of-arrival (DOA) estimation in addition to time of arrival (TOA). The same MAS principles can be applied to UWB technologies [1], in order to improve the link robustness or range, and exploit the high-multipath resolution.

Usually, arrays should be compact in order to be incorporated in radio devices. Obviously, by reducing the single antenna size or the inter-antennas distance, it is possible to minimize the overall system dimension. On the other hand, the mutual coupling also increases for closely spaced sensors, which can detrimentally modify the system performances. Thus, radiation, phase, and distortion characteristics of the single radiator are altered because of the presence of other antennas. In the case of narrow-band arrays, the theory of active element factor accounts for mutual coupling effects, including the possibility of scan blindness [2, 3]. In UWB systems, these phenomena are more difficult to investigate since the driven and the parasitic radiators act in a different way according to the frequency. Moreover, the electrical distance between the antennas depends on the wavelength. Hence, the frequency dependence is an additional parameter which introduces a supplementary complexity with respect to the traditional narrow-band systems.

Investigations on UWB arrays [4–6], often neglect coupling effects. Time-domain factor [6] frequently employed for UWB impulse radio system should be a useful mathematic tool, but it does not take into account that the single element radiation characteristics are altered when placed within a MAS.

Parametric studies on scan impedance and mutual impedance in UWB arrays have been presented in literature [7, 8]. Recently, pulse distortion introduced by interelements interaction has been studied for a particular UWB array [9], and a time-domain approach has been used to investigate the pulse distortion due to the antenna coupling [10].

In this paper, we present a general method, based on the definition of a scattering coefficient, to predict the effects of the passive radiators within MAS. The method has the advantage to avoid the use of a full method of moments (MoM) computation of the array.

In Section 2, we present an electrical circuit analysis of MAS carried out in the frequency domain, by distinguishing between coupling and *scattering* effects. Point source approximation is discussed in Section 3. In Section 4, we model the parasitic antennas as scatters, by means of antenna cross

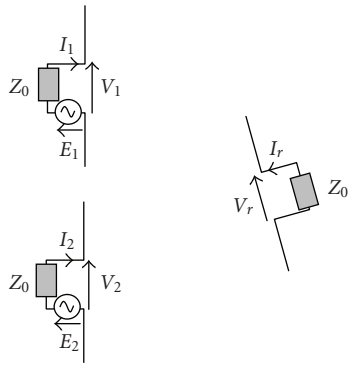

Figure 1: Multiple antennas operating in transmission.

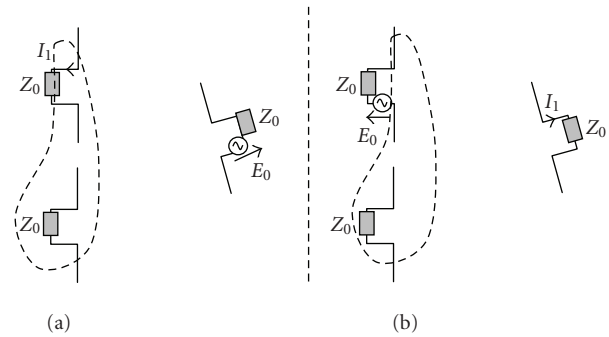

Figure 2: (a) MAS operating in reception and (b) single antenna in reception.

section. We focus on linear and circular arrays using UWB biconical antenna as simple radiator. Multiple scattering is discussed and is shown to be a second-order effect in Section 5. In Section 6, impulse distortion due to interelements interaction is discussed.

2. AN ELECTRICAL NETWORK ANALYSIS OF MULTIPLE ANTENNAS SYSTEMS

The understanding of multiple antenna systems operation is here based on electromagnetic theory and electrical networks analysis as follows. All voltages, impedances, and currents are frequency dependent. This dependence can not be neglected in UWB multiple antennas. Let us consider a MAS operating in transmission, with several source signals and impedance loads on the antenna access port, as depicted in Figure 1. We indicate with the index i ($i = 1, 2, \ldots, N$) the ith element of the transmitting array and with r a receiving antenna.

Then, at a given frequency, the system should be described by a $(N + 1) \times (N + 1)$ network complex matrix, where N is the number of antennas composing the transmitting MAS. For simplicity of discussion, let us consider $N = 2$.

$$\begin{pmatrix} E_1 - Z_0 I_1 \\ E_2 - Z_0 I_2 \\ V_r \end{pmatrix} = \begin{pmatrix} V_1 \\ V_2 \\ -Z_0 I_r \end{pmatrix} = \begin{pmatrix} Z_{11} & Z_{12} & Z_{13} \\ Z_{21} & Z_{22} & Z_{23} \\ Z_{31} & Z_{32} & Z_{33} \end{pmatrix} \begin{pmatrix} I_1 \\ I_2 \\ I_r \end{pmatrix}. \quad (1)$$

Through the superposition theorem, it is clear that a voltage V_r at the receiving port can be obtained by summing the received voltages, when V_1 has its nominal value and $V_2 = 0$, and when V_2 has its nominal value and $V_1 = 0$. Thus, in order to obtain V_r, it is sufficient to have the knowledge of as many complex radiation patterns as antenna ports, where each pattern requires 1 V applied to one port, and 0 V (short circuit) on the others. The values of V_1 and V_2 are simply obtained by solving the electrical network equations of the array in transmission, given its load and source voltage conditions.

Furthermore, by neglecting couplingbetween transmitting and receiving antennas, (1) can be simplified as

$$\begin{pmatrix} E_1 - Z_0 I_1 \\ E_2 - Z_0 I_2 \end{pmatrix} = \begin{pmatrix} V_1 \\ V_2 \end{pmatrix} = \begin{pmatrix} Z_{11} & Z_{12} \\ Z_{21} & Z_{22} \end{pmatrix} \begin{pmatrix} I_1 \\ I_2 \end{pmatrix}. \quad (2)$$

When the MAS operates in reception, the theorem of reciprocity (see Figure 2) makes it straightforward to obtain the received voltage over the loads of the array ports. Since the left and right situations are reciprocal, the current in the load of array port 1 (a) is equal to the current in the load of the single antenna (b). The second array port and its load can be considered to be part of a unique port big antenna. Thus, I_1 in the receiving array can be obtained from the knowledge of the array operating in transmission. Of course, what applies to port 1 applies to port 2 as well, so that both I_1 and I_2 in the receiving array can be computed from the complex gain patterns in transmission. The computation of I_1 requires to solve the electrical network equations to obtain the voltages on each antenna port when array port one is fed with E_0. The same work must be done again when E_0 feeds array port 2. It is important to note here that the conventions for currents signs should be properly defined.

Let us consider a two-antenna system with an ideal voltage source on port 1, a Z_0 load on port 2 ($E_2 = 0$), and the receiving antenna is load with Z_r. It is very easy to obtain

$$\begin{aligned} E_1 &= \left(Z_{11} - \frac{Z_{12}^2}{(Z_{22} + Z_0)}\right) I_1, \\ I_r &= -\left(\frac{Z_{31}}{Z_{33} + Z_r} + \frac{Z_{32} \cdot Z_{12}}{(Z_{33} + Z_r)\,(Z_{22} + Z_0)}\right) I_1. \end{aligned} \quad (3)$$

The last equation means that the received signal is equal to the sum of two terms: the first is the received signal due to the feeding of port 1 in the presence of port 2 open circuited; the second is the received signal due to the current excited in port 2, due to the finite load Z_0 and to the impedance coupling term Z_{12}, which causes radiation by antenna 2. Coming back to the general equations of the three-antennas system, we have

$$-(Z_{33} + Z_r) \cdot I_r = Z_{31} \cdot I_1 + Z_{32} \cdot I_2, \quad (4)$$

where Z_{33} is the receiving antenna self-impedance. What is very interesting in this expression is that it shows that the received signal is the superposition of 2 terms: the first is due to antenna 1 excited by a current I_1 *in the presence of antenna 2 with port 2 open circuited*, and the second is the equivalent of that by inverting indexes 1 and 2. In other words, we can very

rigorously compute the array effect on an excited element as follows.

(i) Compute the radiation with one element excited and all others open circuited.
(ii) Successively compute the radiation of each other element, *in the presence of all others open circuited*, due to the current which feeds it by proximity coupling from the first element. This current is obtained from the electrical coupling network equation.
(iii) Compute the sum of all received signals (as many ones as elements in the array).

Usually, an open-circuited element provides little electromagnetic perturbation on the other elements. This is due to the fact that a little current develops in such an element (take as an example, a quarter wavelength monopole, which is nonresonant when open circuited). Thus, the shadowing effect is very weak in this case. Neglecting this contribution is the so called *point source approximation* [11], since only secondary currents induced by coupling are responsible for radiation by the neighbouring elements.

However, if the element has a large size, current can develop along it, producing scattered radiation which we call *scattering* or diffraction, even if it is open circuited. This effect adds to the secondary radiation due to coupling.

This approach precisely defines what is meant by *scattering* and what is meant by *coupling*.

3. ANTENNA POINT SOURCE APPROXIMATION

A nonspecific isolated antenna radiates an electric field that can be written as follows:

$$\vec{E}_{\text{iso}}(r,\theta,\phi,f) = -j\eta\frac{e^{-j\beta r}}{2\pi r}\vec{E}_0(\theta,\phi,f) = K(f,r)\cdot Z_{11\,\text{iso}}(f)\cdot I_{1\,\text{iso}}(f)\cdot\vec{e}_{\text{iso}}(\theta,\phi,f), \tag{5}$$

where I_1 and Z_{11} represent, respectively, the current and self-impedance at antenna port, and K is a constant depending on the free space impedance η, the observation distance r, and the wave vector in free space β. The dependence on the frequency f is now explicit. Let us consider the $N \times N$ linear system $[V(f)] = [Z(f)][I(f)]$, where N is the number of antennas in the array. By imposing that, one antenna is fed ($V_i = 1\,\text{V}$), and other ones are terminated with their loads; it is possible to calculate the currents developed at the ports of each antenna. Then, the point source approximation of the radiated field, when the ith antenna is fed and other ones are loaded with 50 Ohms in a linear array, is

$$\vec{E}_{r_i}(r,\theta,\varphi,f) = K(f,r)\cdot Z_{11\,\text{iso}}(f)\cdot\left[I_i(f) + \sum_{\substack{n=1\\ n\neq i}}^{N} I_n(f)e^{j\Delta_n(f)}\right]\cdot\vec{e}_{\text{iso}}(\theta,\phi,f), \tag{6}$$

where $\Delta_n(f) = \text{nd}\cdot(2\pi f/c)\hat{a}\bullet\hat{r}$, d is the inter-antennas distance, $\hat{a}$ is the antennas alignment direction, and c the free space velocity. By means of this approximation, the only information that one has to know is the radiation pattern and return loss of the simple radiator, and the $N \times N$ impedance matrix of the system. No explicit near field information is needed, which has the advantage of a much simpler way to predict the multiple antenna system behavior. In a thin dipole MAS, the current distribution on the open-circuited dipole, when another one is fed, is very small; thus the scattering effect does not affect the radiation characteristics in a significant way. Let us consider two thin dipoles (radius $a = 0.1\,\text{mm}$) resonant at 3 GHz in a linear end-fire array configuration ($d = 50\,\text{mm}$). In Figure 3, we compare the radiation pattern, when the second antenna is loaded with 50 Ohms (black line), calculated by the MoM, and the radiation pattern obtained by point source approximation which neglects *scattering* effects (blue line).

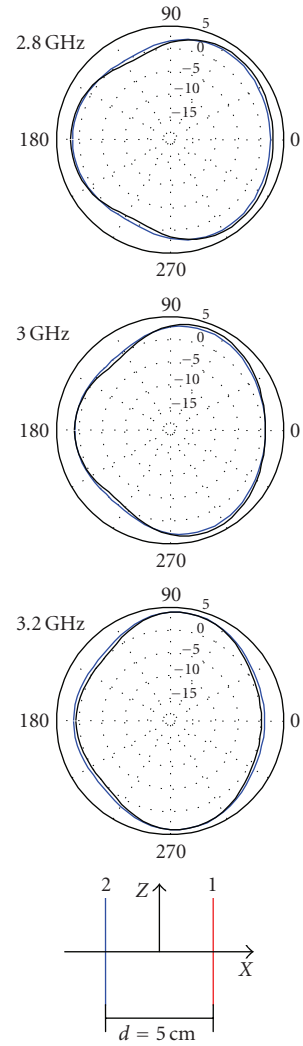

FIGURE 3: Thin dipoles ($d = 50\,\text{mm}$): simulated expected radiation pattern (black line) and point source approximation (blue line).

Accordingly, the point source approximation is satisfactory even in case of strong mutual coupling in classical narrowband systems, where dipole is commonly assumed as single radiator.

Let us employ a biconical omnidirectional antenna as simple radiator in order to investigate UWB multiple antennas.

This antenna is derived from a previous work on the design of an UWB antenna for channel measurements [12]. Antenna dimensions are 31 mm × 37 mm (diameter × height), and its input bandwidth is 2.75–16 GHz; see Figure 4. The inter-antennas distance d is taken with respect to the bicone's evolution axis.

In Figure 5, we show the azimuth radiation pattern of two bicone antennas ($d = 50$ mm), one driven and the other one loaded with 50 Ohms, together with its point source approximation. It is easy to see that the approximation does not agree with the expected radiation pattern. This is due to the fact that, when the first antenna is excited, the current density on the second open-circuited antenna is stronger than that in the dipole case, and the *scattering* effect is predominant over the coupling one. By increasing the inter-antennas distance, radiator interactions become less significant, and also *scattering*.

4. SINGLE SCATTERING BETWEEN RADIATORS

As seen in the previous section, predicting scattering turns out is essential to calculate the radiation pattern of multiple antennas, especially in UWB applications as the antenna size is not negligible with respect to the wavelength. Let us consider the same two biconical antenna arrays as above, where open circuit conditions are imposed on the second antenna port. We consider that the total radiated field is due to the sum of two contributions: the first is the suitably delayed field of the excited isolated radiator; the second, which represents the open-circuited antenna, is the same radiated field suitably delayed and multiplied by a scattering coefficient $\mathrm{SC}(f, d, \theta, \varphi)$. In a two-antenna array, as depicted in Figure 4, this results for the field radiated by the array in the expression:

$$\begin{aligned}\vec{E}\,(r,\theta,\phi,f,d) &= \vec{E}_{\mathrm{iso}}(r,\vartheta,\phi,f)\\ &\quad\cdot\left(e^{j(d\pi f/c)\sin\theta\cos\phi} + \mathrm{SC}(f,d,\theta,\phi)\cdot e^{-j(d\pi f/c)\sin\theta\cos\phi}\right).\end{aligned} \tag{7}$$

At this stage, there is no assumption as long as SC is a free parameter. The formula is just shaped in order to envision the open-circuited antenna as a scatter, which has same geometry and physical characteristics as a single element. Antennas have two possible modes of scattering: the first is the scattering due to the fact that the antenna is of a given shape, material and size; the second because the antennas have been designed to transmit or receive RF energy at the relevant frequency [13]. By means of a MoM tool (Wipl-D), it is possible to compute the antenna radar cross section and scattered field Es by the open circuited antenna, illuminated by a field Ei of a plane wave incident from the direction (θ_i, ϕ_i), where the excited radiator is located in the array. We here limit ourselves to the main polarization, that is, the θ-component. Once the scattered field by the open-circuited antenna has been computed by MoM, the scattering coefficient SC can be approximated for every distance as follows:

$$\mathrm{SC}(f,d,\theta,\phi) \approx \frac{1}{d}e^{-j(2\pi f/c)d}\frac{E_s(\theta,\phi,f)}{E_i(\theta_i,\phi_i,f)}. \tag{8}$$

Thus, the scattering coefficient is approximated by a far field computation, which is easier than a near field computation. In Figure 6, we show the result of this SC approximation on the computation of the azimuth radiation pattern. We observe a varying accuracy according to the frequency; nevertheless the approximation is satisfactory even at low inter-antennas distance ($d = 50$ mm). Naturally, the discrepancy increases at the higher frequencies, as the wavelength becomes smaller than the radiator size. Using (7) and by knowing the exact value of $\vec{E}\,(r,\theta,\varphi,f,d)$ and $\vec{E}_{\mathrm{iso}}(r,\theta,\varphi,f)$, one can also obtain the exact value of the SC.

Looking at the cylindrical antenna geometry, a natural but strong approximation is to eliminate the ϕ-dependency. Averaging over the azimuth angle will introduce an inaccuracy in evaluating the SC and consequently also on the radiation pattern. In Figures 7 and 8, we compare the azimuth-averaged exact value of SC with that computed with (8). A good agreement is shown for all frequencies and elevation angles, with the exception of the lowest frequencies at the zenith (z-axis). This should in part be explained by the presence of a stronger side component of the scattered field, which is not taken into account in the plane wave approximation. Furthermore, it is interesting to see that from 10 to 16 GHz the antenna presents a different scattering behavior in amplitude as well in phase. This is due to the fact that an UWB antenna, even if matched, does not present the same radiation behavior over its full bandwidth. In particular, this bicone was designed for channel measurement in the FCC band, that is, below 10.6 GHz [12].

Obviously, using a mean value in the azimuth dependence of the SC yields an inaccuracy in the radiation pattern computation, but it is interesting to observe (see Figure 9) that this inaccuracy may be tolerable. In particular, when the antennas are distant enough, the error introduced by averaging can be neglected as depicted in Figure 9. This allows a reduction of the problem complexity, and a reduction of the number of parameters needed to describe the multiple antennas behavior, which has some virtues due the large bandwidth in UWB. In Figures 10 and 11, we show the expected radiation pattern together with its scattering approximation on two elevation planes. The SC model is less accurate on the X-Z plane (see Figure 10) than on Y-Z plane (see Figure 11) where the array effect is more significant.

The two antennas array presented above is a simple case of interaction between radiators, where the parasitic element can be easily modeled as a scatter.

Let us now consider a circular array, as depicted in Figure 12 (radius $a = 50$ mm), composed by three equally spaced bicone antennas. The driven radiator (antenna 1) is

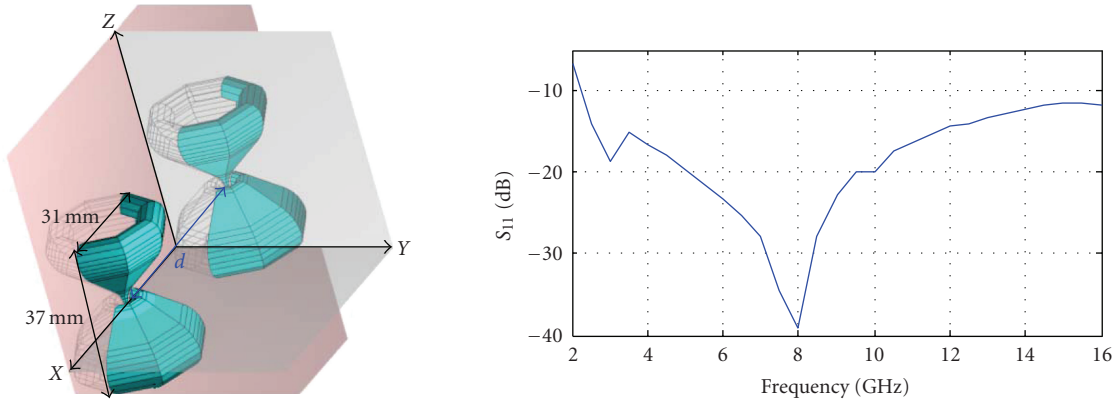

(a) (b)

Figure 4: (a) ENSTA bicone antennas and (b) ENSTA bicone return loss.

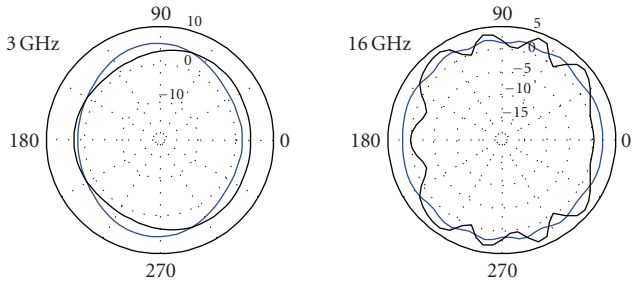

(a) (b)

Figure 5: Two ENSTA bicone antennas ($d = 50$ mm): antenna 1 is excited; antenna 2 is 50 Ohms loaded. Simulated expected radiation pattern (black line) and point source approximation (blue line).

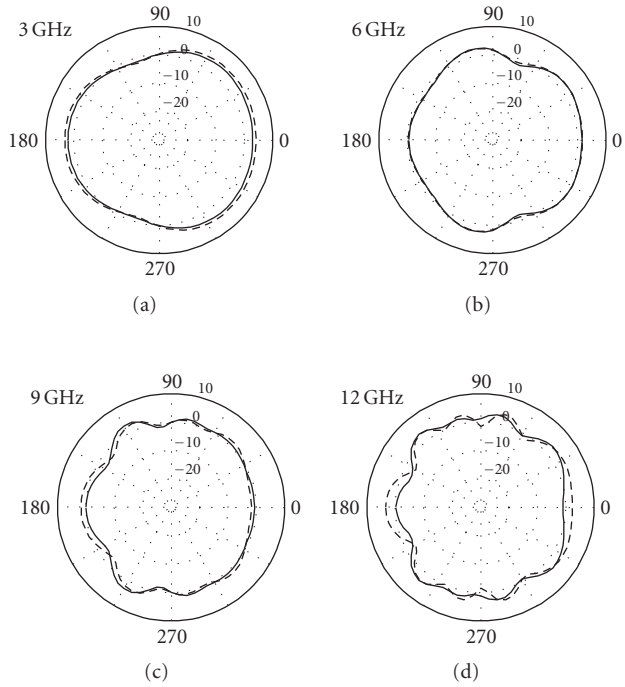

(a) (b) (c) (d)

Figure 6: Expected azimuth (X-Y plane) radiation pattern for two antennas (solid line) and SC approximation (dashed line). Antenna 1 is excited; antenna 2 is open circuited ($d = 50$ mm).

placed along the y-axis, while the others are open circuited. This is a generalization of the two bicones array presented above. Thus, the total radiated field can be expressed as

$$\vec{E}\,(r,\theta,\phi,f,d) = \vec{E}_{\text{iso}}(r,\theta,\phi,f) \cdot\left(e^{j(2\pi/\lambda)a\sin\theta\cos(\phi-\phi_1)} + \sum_{n=2}^{N} \text{SC}_{n1}(f,d,\theta,\phi)\cdot e^{j(2\pi/\lambda)a\sin\theta\cos(\phi-\phi_n)}\right), \tag{9}$$

where φ_n represents the azimuth position of the nth radiator, and $\text{SC}_{n1}(f,d,\theta,\varphi)$ is the scattering coefficient calculated by (8), but properly turned in order to take into account the nth antenna position with respect to the fed antenna. Hence, we consider only the scattered field by antennas 2 and 3 due to the excitation of antenna 1. Multiple scattering between the two open-circuited antennas is here neglected. Figure 12 shows that effectively multiple scattering should be neglected without a significant degradation of the approximation accuracy.

5. MULTIPLE SCATTERING BETWEEN RADIATORS

Generally, by increasing the number of antennas, multiple scattering effects have to be taken into account. However, depending on the array configuration this can be assumed as a second-order effect.

Let us consider a three bicones linear array along the x-axis: antenna 1 is placed at $x = d$, antenna 2 at $x = 0$, and antenna 3 at $x = -d$.

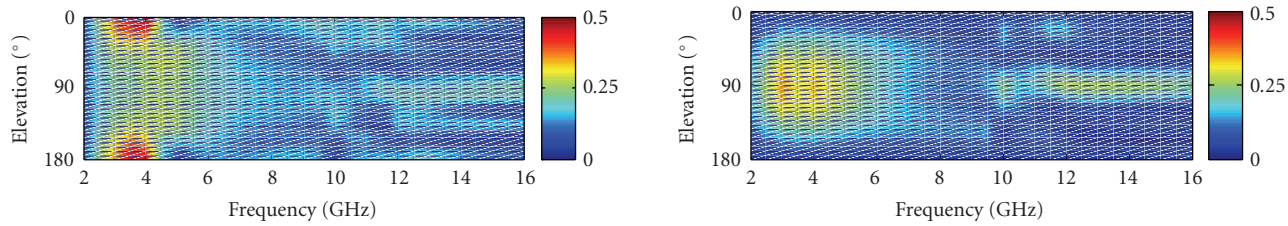

Figure 7: Azimuth-averaged SC modulus of ENSTA bicone antenna ($d = 50$ mm): (a) exact computation and (b) computation by means of scattered fields.

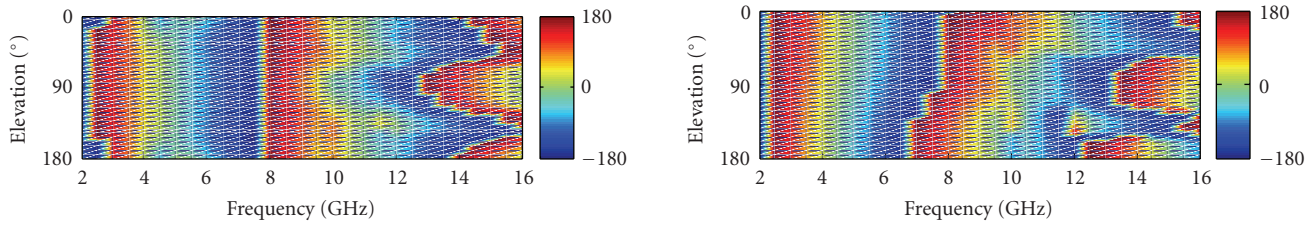

Figure 8: Azimuth-averaged SC argument of ENSTA bicone antenna ($d = 50$ mm): (a) exact computation and (b) computation by means of scattered field.

When the antenna 1 is fed, single and multiple scatterings should be considered. According to (7) and (8), the scattered field by antenna 2 can be computed as

$$\vec{E}_{\text{open }21}(r,\theta,\phi,f,d) = \vec{E}_{\text{iso}}(r,\theta,\phi,f)\cdot \text{SC}_{21}(f,d,\theta,\phi), \tag{10}$$

and the scattered field by antenna 3 can be expressed as

$$\vec{E}_{\text{open }31}(r,\theta,\phi,f,d) = \vec{E}_{\text{iso}}(r,\theta,\phi,f)\cdot\left(\text{SC}_{31}(f,d,\theta,\phi)\cdot e^{-j(2d\pi f/c)\sin\theta\cos\phi}\right). \tag{11}$$

Scattering coefficients are computed according to (8):

$$\begin{aligned}\text{SC}_{31}(f,d,\theta,\phi) &\approx \frac{1}{2\cdot d}e^{-j(2\pi f/c)2\cdot d}\frac{E_s(\theta,\phi,f)}{E_i(\theta_{31},\phi_{31},f)},\\ \text{SC}_{21}(f,d,\theta,\phi) &\approx \frac{1}{d}e^{-j(2\pi f/c)d}\frac{E_s(\theta,\phi,f)}{E_i(\theta_{21},\phi_{21},f)}.\end{aligned} \tag{12}$$

In addition, multiple scattering between antenna 2 and antenna 3, which are open circuited, can be expressed as

$$\vec{E}_{\text{open }32}(r,\theta,\phi,f,d) = \vec{E}_{\text{iso}}(r,\theta,\phi,f)\cdot \text{SC}_{21}(f,d,\theta,\phi)\cdot\left(\text{SC}_{32}(f,d,\theta,\phi)\cdot e^{-j(2d\pi f/c)\cos\theta\cos\phi}\right), \tag{13}$$

where

$$\text{SC}_{32}(f,d,\theta,\phi) \approx \frac{1}{d}e^{-j(2\pi f/c)d}\frac{E_s(\theta,\phi,f)}{E_i(\theta_{32},\phi_{32},f)}. \tag{14}$$

In (10), (11), and (13), electric fields are opportunely delayed by taking into account the antenna position along the x-axis of different antennas. According to (8), the scattering coefficients in (12), and (14) are computed by simulating the single antenna cross section. In the computation of a generic SC_{mn}, the illuminating radiated field is a plane wave, coming from the direction (θ_{mn},ϕ_{mn}) of the mth antenna with respect to the nth antenna. Practically, it is the same scattering coefficient in (8), but suitably attenuated, delayed, and oriented, in order to take into account the position of the antennas within the array. Finally, the total radiated electric field can be computed by means of the superposition theorem as

$$\begin{aligned}\vec{E}\,(r,\theta,\phi,f,d) = \vec{E}_{\text{iso}}(r,\theta,\phi,f)e^{j(2d\pi f/c)\sin\theta\cos\phi}\\ + \vec{E}_{\text{open }21} + \vec{E}_{\text{open }31} + \vec{E}_{\text{open }32}.\end{aligned} \tag{15}$$

This expression neglects the 2nd-order scattered field by the fed antenna due to the scattered fields by both antenna 2 and antenna 3. In Figures 13 and 14, we show the expected radiation pattern (black line) and the electric field computed by means of (15), (blue marker) for two different inter-antennas distance $d = 5$ cm and $d = 10$ cm. The electric field agrees quite well with the expected radiation pattern especially at higher inter-antennas distance. However, multiple scattering expressed in (14) is small comparing to the single scattering terms, given that a little current distribution is developed on open-circuited antenna 2.

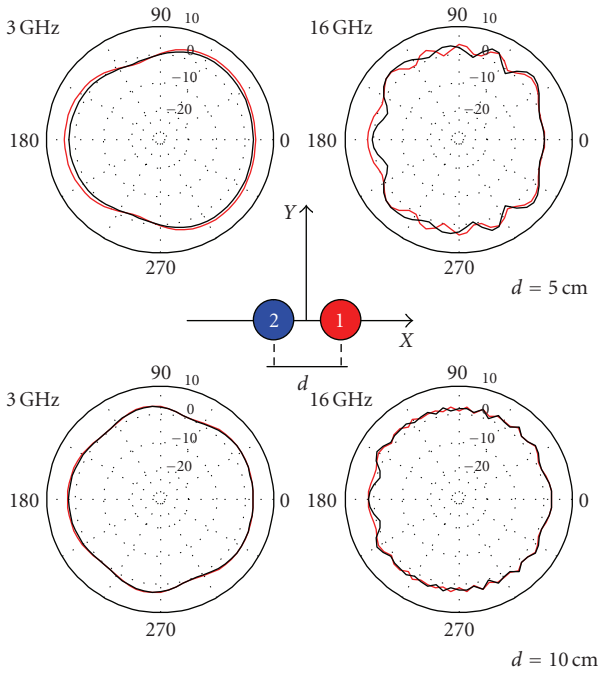

FIGURE 9: Expected azimuth (X-Y plane) radiation pattern for two antennas (solid line); SC approximation (red line) with scattering coefficient averaged over the azimuth angle. Antenna 1 is excited; antenna 2 is open circuited.

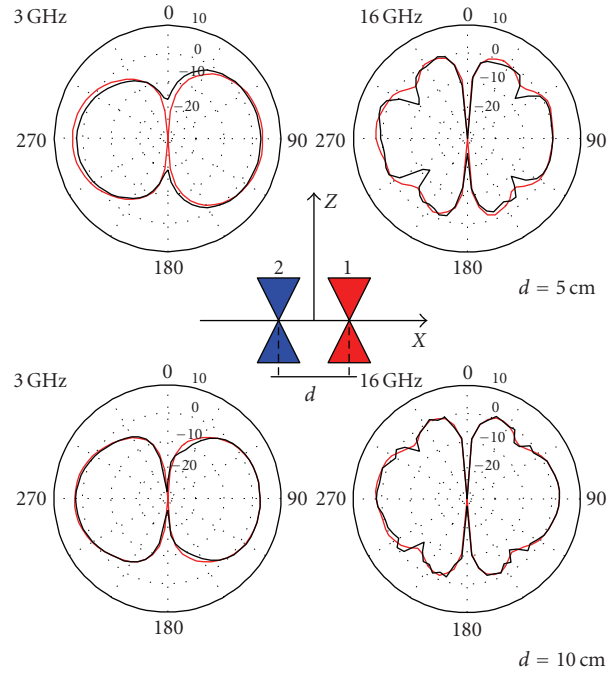

FIGURE 10: Expected radiation pattern in elevation ($\varphi = 0°$, Z-X plane) (black line) and SC azimuth-averaged approximation (red line). Antenna 1 is excited; antenna 2 is open circuited.

Furthermore, the single scattering by antenna 3, computed by means of (11) should be neglected because of the shadowing due to the presence of antenna 2.

Consequently, the total radiated electric field can be very simply approximated as

$$\vec{E}\,(r,\theta,\phi,f,d) = \vec{E}_{\text{iso}}(r,\theta,\phi,f)e^{j(2d\pi f/c)\sin\theta\cos\phi} + \vec{E}_{\text{open }21}. \tag{16}$$

Figures 13 and 14 validate this assumption by showing that the radiation pattern computed by means of (16) is nearly exactly superimposed to the radiation pattern computed by means of (15), which takes into account all the single and multiple scattering terms. This means that, in this case, the three bicones array has the same behavior as the two bicones array.

Similarly, when antenna 2 is fed, only single scattering on antennas 1 and 3 can be taken into account. Thus, the total radiated field can be written as

$$\begin{aligned}\vec{E}_{\text{open}}(r,\theta,\phi,f,d) &= \vec{E}_{\text{iso}}(r,\theta,\phi,f)\cdot\Big(1+\text{SC}_{12}(f,d,\theta,\phi)\cdot e^{j(2d\pi f/c)\sin\theta\cos\phi} \\ &\quad + \text{SC}_{32}(f,d,\theta,\phi)\cdot e^{-j(2d\pi f/c)\sin\theta\cos\phi}\Big),\end{aligned} \tag{17}$$

where $\text{SC}_{12}(f,d,\theta,\varphi)$ and $\text{SC}_{32}(f,d,\theta,\varphi)$ are the scattering coefficients for antennas 1 and 3 calculated by (8), by taking into account their position with respect to the fed antenna. Figure 15 shows the azimuth pattern together with its SC approximation for a linear array, when the central antenna is fed and expressed in (17). Multiple scattering between two open-circuited antennas can be neglected while preserving the approximation accuracy.

The model taking into account single and double scatterings, between two parasitic elements, can be generalized for a nonspecific N antennas array. Thus, the radiated field by the mth fed element, within the array, can be written as

$$\begin{aligned}&\vec{E}_m(r,\theta,\phi,f,d) \\ &\quad = \vec{E}_{\text{iso}}(r,\theta,\phi,f) \\ &\qquad \cdot\left(e^{j\delta_m(f)} + \sum_{\substack{n=1\\n\neq m}}^{N}\left(\text{SC}_{nm} + \sum_{\substack{p=1\\p\neq n}}^{N}(\text{SC}_{np}\cdot\text{SC}_{pm})\right)e^{j\delta_n(f)}\right),\end{aligned} \tag{18}$$

where SC_{nm} is the scattering coefficient between the nth and mth antenna computed by means of (8), omitting the (f,d,θ,ϕ) dependence for the sake of briefness. The phase delay $\delta_n(f) = (2\pi f/c)\vec{a}_n\bullet\hat{r}$ takes into account the position of the nth antenna (indicated by the vector $\vec{a}_n$) in the array. As far as double scattering can be considered as a second-order effect, (18) can be simplified as

$$\vec{E}_m(r,\theta,\phi,f,d) = \vec{E}_{\text{iso}}(r,\theta,\phi,f)\cdot\left(e^{j\delta_m(f)} + \sum_{\substack{n=1\\n\neq m}}^{N}\text{SC}_{nm}e^{j\delta_n(f)}\right). \tag{19}$$

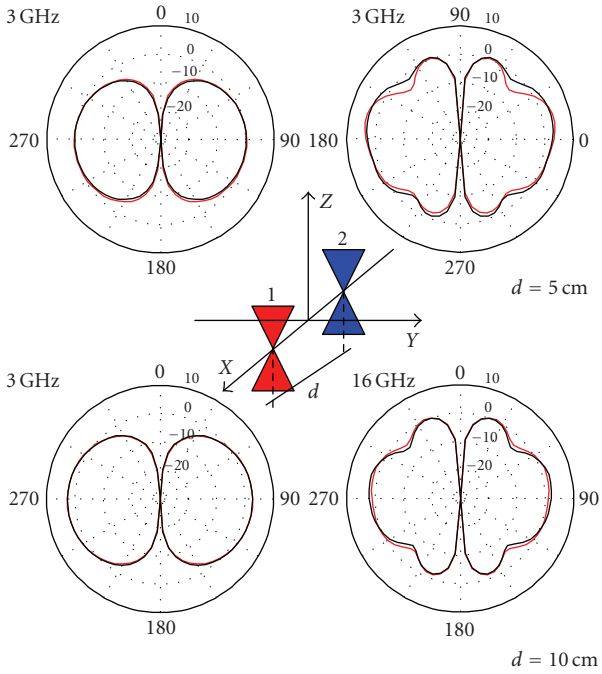

Figure 11: Expected radiation pattern in elevation ($\varphi = 90^\circ$, Z-Y plane) (black line) and SC azimuth-averaged approximation (red line). Antenna 1 is excited; antenna 2 is open circuited.

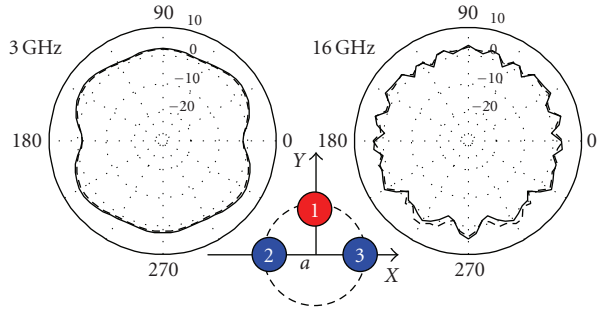

Figure 12: Three-bicone circular array with feeding on antenna 1 and open-circuit on antennas 2 and 3. Expected azimuth (X-Y plane) radiation pattern (solid line) and SC approximation (dot line).

Therefore, once the single isolated antenna radiation and its antenna cross section have been computed, one should easily predict the performances of a generic array. The proposed approach is of particular interest in compact MAS design, for which the radiation pattern distortion is stronger. On the other hand, the proposed model is still useful in large bidimensional arrays, but multiple scattering should be considered, given that mutual coupling can generate phase resonance among the arrays [14].

6. PULSE DISTORTION DUE TO INTER-ELEMENT INTERACTION

By means of time domain approach, it is possible to access the waveform of the radiated field as a function of the angular coordinates. When an antenna is excited by an incident signal $w(t)$, it radiates an electric field, whose waveform, $e(\theta, \phi, t)$ in the (θ, ϕ) direction, is a distorted version of the incident one. Distortion is due to dispersion, that is, the frequency-dependence of the realized gain and the angular frequency-deviation of the radiation pattern. A common feature in UWB antenna characterization is a time domain approach with the purpose to characterize the distortion introduced by the antenna. In multiple antenna systems, the additional distortion due to the interaction between radiators has to be taken into account. Even when close antennas are open circuited, scattering effects are responsible for some distortion, which is the time domain counterpart of the alteration of the radiation pattern discussed in the previous paragraphs. This is of practical importance in pulsed schemes, where distortion may affect the overall system performance by introducing inter-symbol interference.

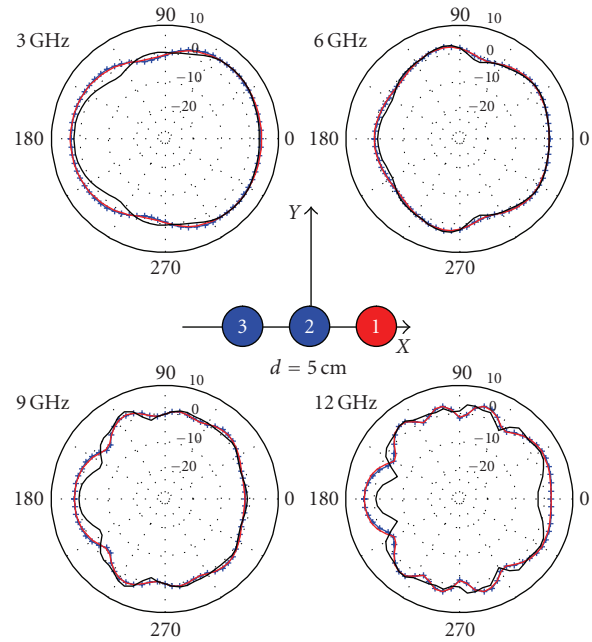

Figure 13: Three-bicone linear array ($d = 5$ cm) with feeding on antenna 1 and open circuit on antennas 2 and 3. Expected azimuth (X-Y plane) radiation pattern (black line), SC approximation with all single and multiple scattering terms (blue marker), and SC approximation with only single scattering on antenna 2 (red line).

Here, the chosen excitation signal $w(t)$ is a Gaussian impulse with a -10 dB power bandwidth of 3–10.0 GHz (see Figure 16). Our aim is to estimate the accuracy of the SC approximation.

In Figures 17, 18, 19 we show, for different directions, the waveform $e(\theta, \phi, t)$ radiated by a biconical antenna in a two radiators linear array when the parasitic element is open circuited, and we compare it with the radiated waveform $e_{SC}(\theta, \phi, t)$ computed by means of the SC. The inter-antennas distance is 5 cm. The computed waveform agrees quite well with the expected one. A small degradation accuracy is shown for the highest elevation angles and in the end-fire direction ($\phi = 180^\circ$).

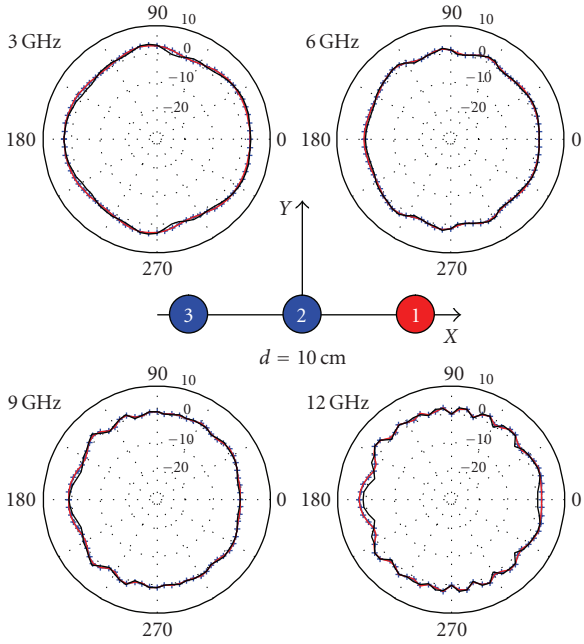

FIGURE 14: Three-bicone linear array ($d = 10$ cm) with feeding on antenna 1 and open circuit on antennas 2 and 3. Expected azimuth (X-Y plane) radiation pattern (black line), and SC approximation with all single and multiple scattering terms (blue marker), SC approximation with only single scattering on antenna 2 (red line).

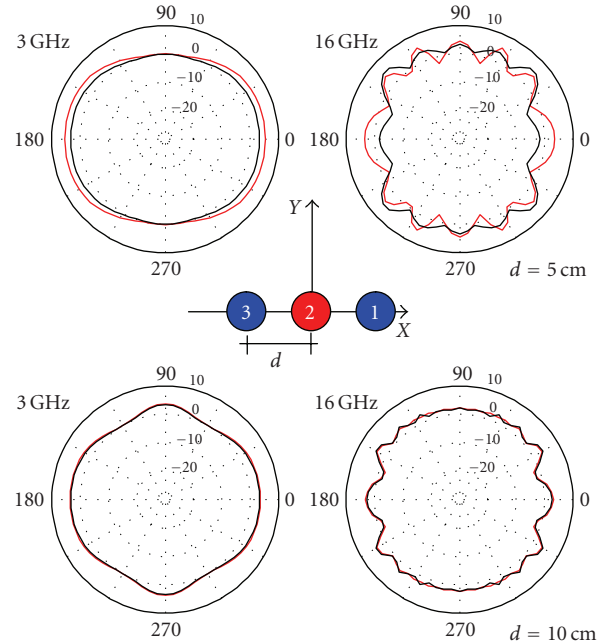

FIGURE 15: Three-bicone linear array with feeding on antenna 2 and open circuit on antennas 1 and 3. Expected azimuth (X-Y plane) radiation pattern (solid line) and SC approximation (red line).

Figures 17, 18, 19 show a visual agreement of the approximation. Let us consider a simple pulse scheme in a simple AWGN channel (power spectral density equal to N_0). The receiver is a classical correlator, and the reference template pulse is $\mathrm{ref}(t)$.

Since the receiver usually chooses $\tau_{\max}$ in order to maximize SNR, then

$$\mathrm{SNR} = \frac{\int_{-\infty}^{+\infty} |\mathrm{rec}(t)|^2 dt}{Z_0 N_0} \times \left| \frac{\int_{-\infty}^{+\infty} \mathrm{rec}(t)\mathrm{ref}(t-\tau_{\max})dt}{\sqrt{\int_{-\infty}^{+\infty} |\mathrm{rec}(t)|^2 dt} \cdot \sqrt{\int_{-\infty}^{+\infty} |\mathrm{ref}(t)|^2 dt}} \right|^2, \quad (20)$$

where Z_0 is the load on receiving antenna, and $\mathrm{rec}(t)$ is the received pulse which can be expressed as [15]

$$\mathrm{rec}(t,\theta,\phi) = \frac{\partial^{-1}}{\partial t} * h_{\mathrm{TX}}(t,\theta,\varphi) * h_{\mathrm{RX}}(t,\theta,\varphi) * w(t), \quad (21)$$

where $h_{\mathrm{TX}}(t,\theta,\varphi)$ and $h_{\mathrm{RX}}(t,\theta,\varphi)$ are the transmitting impulse response of the transmitting and receiving antennas, respectively. The reference pulse is chosen to be identical to the received pulse when two ideal isotropic antennas are used. If we consider an ideal antenna at the transmitting side and an array on the receiving side, we can estimate the effect

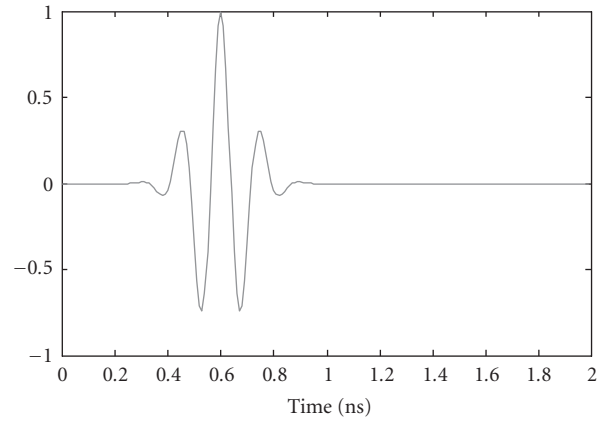

FIGURE 16: Excitation signal at antenna port: Gaussian impulse with a −10 dB power bandwidth of 3–10.0 GHz.

of the SC approximation on SNR:

$$\mathrm{SNRD}(\theta,\phi) = \frac{\mathrm{SNR}_{\mathrm{SC}}(\theta,\phi)}{\mathrm{SNR}_{\mathrm{expected}}(\theta,\phi)}, \quad (22)$$

where $\mathrm{SNR}_{\mathrm{SC}}(\theta,\varphi)$ and $\mathrm{SNR}_{\mathrm{expected}}(\theta,\varphi)$ are the SNR computed by using the SC approximated and the real antenna impulse response.

As depicted in Figure 20, the difference on SNR is less then 0.7 dB in case of low inter-antennas distance ($d = 5$ cm) and about 0 dB for higher antenna distances ($d = 10$ cm, $d = 20$ cm).

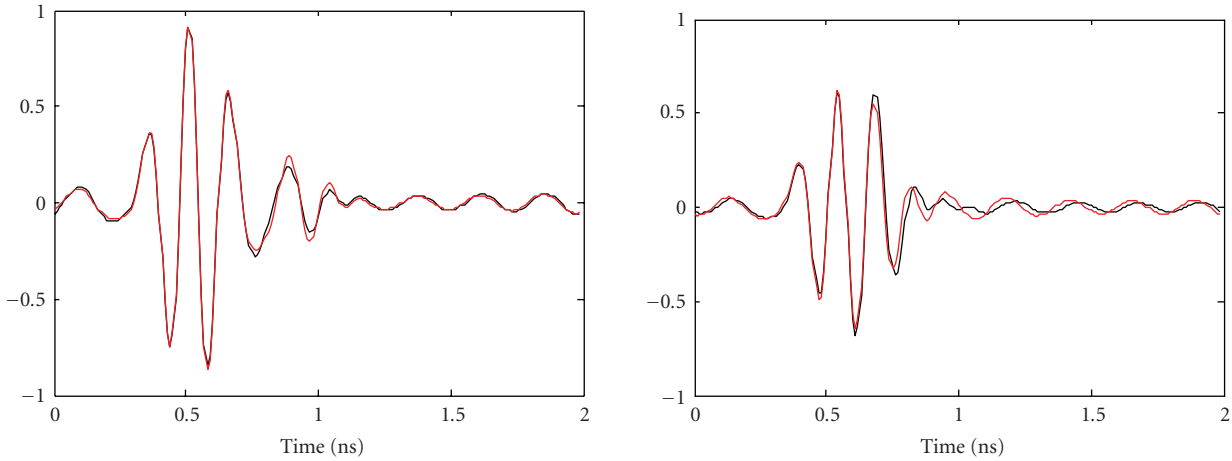

Figure 17: Expected radiated waveform (black line), SC approximation (red line) at (a) $\varphi = 0^\circ$ and $\theta = 90^\circ$, (b) $\theta = 30^\circ$.

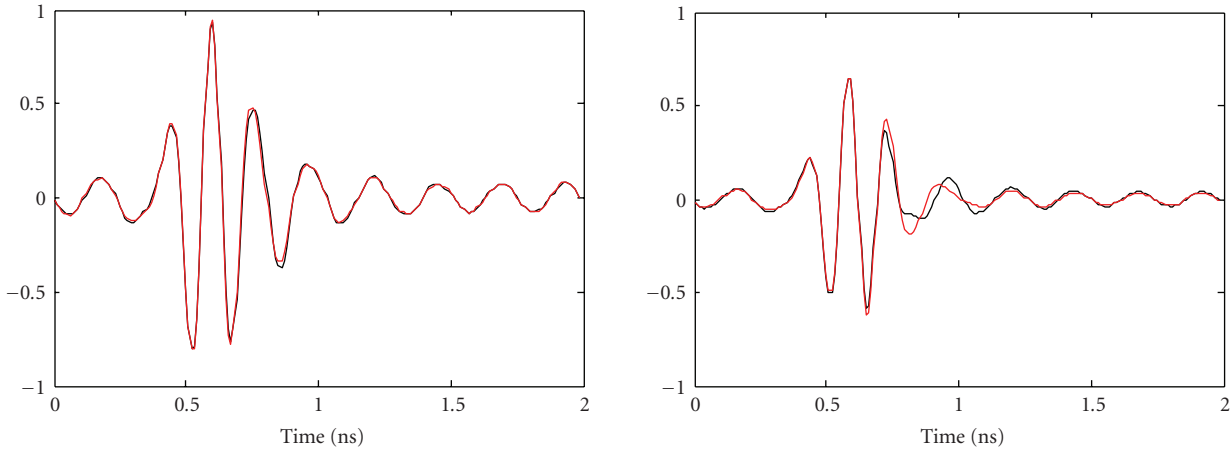

Figure 18: Expected radiated waveform (black line), SC approximation (red line) at (a) $\varphi = 90^\circ$ and $\theta = 90^\circ$, (b) $\theta = 30^\circ$.

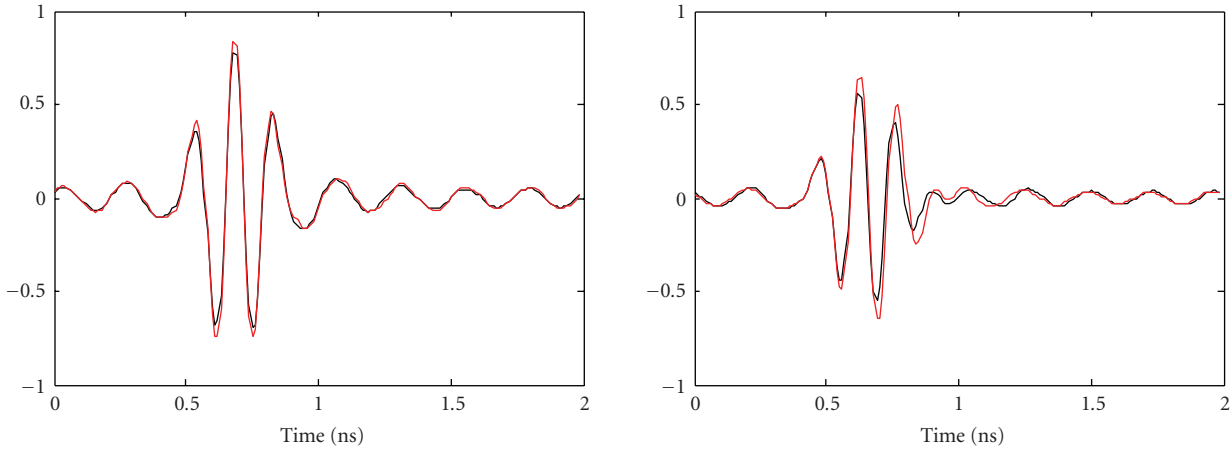

Figure 19: Expected radiated waveform (black line), SC approximation (red line) at (a) $\varphi = 180^\circ$ and $\theta = 90^\circ$, (b) $\theta = 30^\circ$.

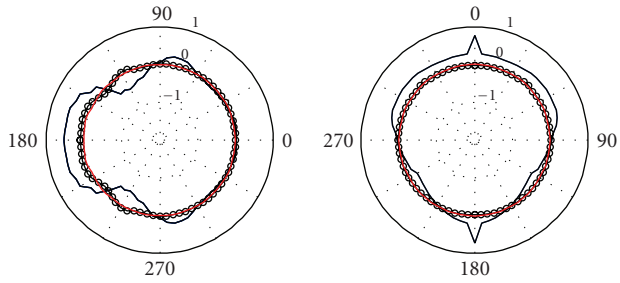

FIGURE 20: (a) SNRD (dB) in azimuth and (b) elevation plane. d = 5 cm (black line), 10 cm (open dots), and 20 cm (red line).

7. CONCLUSIONS

A network analysis of multiple antenna systems has been carried out in order to identify the origins of inter-elements interaction and model them. This approach discriminate precisely what is *scattering* from what is *coupling*. When the first one is negligible, a point source approximation may be applied, as commonly occurs with thin dipoles. In contrast with UWB antennas, which generally occupy a larger volume, the contribution to total electric field by the open-circuited elements becomes more significant. Thus, *scattering* has been modelled by a *scattering coefficient* (SC). A practical way to obtain this SC is to illuminate the open-circuited passive element and compute the bistatic antenna radar cross section. This approximation neglects the incident wave curvature and near field effects, but the reasonable agreement with full computations justifies its use, given its much greater simplicity. As a result, only single radiator pattern and SC are sufficient to predict the multiple antennas performance. The dependence on azimuth angle can further be averaged in the bicone antennas case, without significant loss in approximation validity. This means a simplification of the problem of inter-elements interaction, and a reduction of the number of parameters describing the phenomena. Multiple scattering between antennas can be considered as a second-order effect. Furthermore, single scattering can be neglected for the most distant radiators, especially if shadowing by a closer radiator occurs. As a consequence, a three bicones linear array has the same behavior as the two bicones array when the driven radiator is at the extremity. More generally, scattering due to the closest elements is the major cause of radiation pattern alteration and additional distortion. Finally, additional distortion due to inter-elements interaction has been investigated. It has been shown that the SC approximation is accurate enough to predict the effect of the antenna in an UWB pulse scheme. The generality of the proposed model simplifies the task of the antenna designer, who does not have to simulate several array designs, and, consequently, time consuming full-MoM simulations of the whole array are not required.

ACKNOWLEDGMENT

This work was in part supported by the European Commission under IST integrated project *PULSERS Phase II*.

REFERENCES

[1] A. Sibille, "Spatial diversity," in *UWB Communication Systems—A Comprehensive Overview*, EURASIP Book Series on Signal Processing and Communications, pp. 302–329, Hindawi Publishing Corporation, New York, NY, USA, 2006.

[2] D. M. Pozar, "The active element pattern," *IEEE Transactions on Antennas and Propagation*, vol. 42, no. 8, pp. 1176–1178, 1994.

[3] K. K. Chan, R. M. Turner, and K. Chadwick, "Coupling coefficients and active element patterns of finite waveguide arrays," in *Proceedings of the IEEE Antennas and Propagation Society International Symposium Digest (APS '95)*, vol. 3, pp. 1396–1399, Newport Beach, Calif, USA, June 1995.

[4] A. Shlivinski and E. Heyman, "A unified kinematic theory of transient arrays," in *Ultra-Wideband Short-Pulse Electromagnetics*, P. D. Smith and S. R. Cloude, Eds., pp. 327–334, Kluwer Academic/Plenum Publishers, New York, NY, USA, 2000.

[5] W. Soergel, C. Waldschmidt, and W. Wiesbeck, "Transient radiation from a linear UWB antenna array," in *Proceedings of the URSI International Symposium on Electromagnetic Theory (URSI EMTS '04)*, pp. 1254–1256, Pisa, Italy, May 2004.

[6] S. Foo and S. Kashyap, "Time-domain array factor for UWB antenna array," *Electronics Letters*, vol. 39, no. 18, pp. 1304–1305, 2003.

[7] T. Chio and D. H. Schaubert, "Parameter study and design of wide-band widescan dual-polarized tapered slot antenna arrays," *IEEE Transactions on Antennas and Propagation*, vol. 48, no. 6, pp. 879–886, 2000.

[8] P. L. Tokarsky, "Coupling effects in resistive UWB antenna arrays," in *Proceedings of the 3rd International Conference in Ultrawideband and Ultrashort Impulse Signals*, pp. 188–190, Sevastopol, Ukraine, September 2006.

[9] G. Kotyrba and H. J. Chaloupka, "On signal distortion in compact UWB arrays due to element interaction," in *Proceedings of the IEEE Antennas and Propagation Society International Symposium Digest (APS '05)*, vol. 1 A, pp. 614–617, Washington, DC, USA, July 2005.

[10] M. Ciattaglia and G. Marrocco, "Investigation on antenna coupling in pulsed arrays," *IEEE Transactions on Antennas and Propagation*, vol. 54, no. 3, pp. 835–843, 2006.

[11] K. Siakavara and J. N. Sahalos, "A simplification of the synthesis of parallel wire antenna arrays," *IEEE Transactions on Antennas and Propagation*, vol. 37, no. 7, pp. 936–940, 1989.

[12] H. Ghannoum, S. Bories, C. Roblin, and A. Sibille, "Biconical antennas for intrinsic characterization of the UWB channel," in *Proceedings of the IEEE International Workshop on Antenna Technology: Small Antennas and Novel Metamaterials (IWAT '05)*, vol. 2005, pp. 101–104, Singapore, March 2005.

[13] R. C. Hansen, "Relationship between antennas as scatters and as radiators," *Proceedings of the IEEE*, vol. 77, no. 5, pp. 659–662, 1989.

[14] R. W. P. King, "Supergain antennas and the Yagi and circular arrays," *IEEE Transactions on Antennas and Propagation*, vol. 37, no. 2, pp. 178–186, 1989.

[15] A. Shlivinski, E. Heyman, and R. Kastner, "Antenna characterization in the time domain," *IEEE Transactions on Antennas and Propagation*, vol. 45, no. 7, pp. 1140–1149, 1997.

Hindawi Publishing Corporation
International Journal of Antennas and Propagation
Volume 2008, Article ID 378285, 7 pages
doi:10.1155/2008/378285

Research Article

Archimedean Spiral Antenna Calibration Procedures to Increase the Downrange Resolution of a SFCW Radar

Ioan Nicolaescu[1] and Piet van Genderen[2]

[1] *Department of Military Electronic Systems and Communications, Military Technical Academy, 81-83 George Cosbuc Avenue, Bucharest 050141, Romania*
[2] *International Research Centre for Telecommunication-transmission and Radar, University of Technology, Mekelweg, 2628 Delft, The Netherlands*

Correspondence should be addressed to Ioan Nicolaescu, ioannic@mta.ro

Received 18 June 2007; Revised 5 October 2007; Accepted 12 February 2008

Recommended by Dejan Filipovic

This paper deals with the calibration procedures of an Archimedean spiral antenna used for a stepped frequency continuous wave radar (SFCW), which works from 400 MHz to 4845 MHz. Two procedures are investigated, one based on an error-term flow graph for the frequency signal and the second based on a reference metallic plate located at a certain distance from the ground in order to identify the phase dispersion given by the antenna. In the second case, the received signal is passed in time domain by applying an ifft, the multiple reflections are removed and the phase variation due to the time propagation is subtracted. After phase correction, the time domain response as well as the side lobes level is decreased. The antenna system made up of two Archimedean spirals is employed by SFCW radar that operates with a frequency step of 35 MHz.

1. INTRODUCTION

Located at the interface between the propagation media and the electronic device, the antenna is a very important element of any electronic equipment used either to pass information from one place to another or for object detection and tracking (radar systems etc.). In the last decade, a lot of work has been done to find a proper system for landmine detection. Among other systems, the ground penetrating radar (GPR) is very promising because of its advantages over other types of sensors as: no direct contact with the surface, the possibility to detect both metallic and nonmetallic objects, and so forth. The GPR works either in time domain (video pulse radar) or in frequency domain (SFCW radar). In the case of SFCW radar, the antenna system consists of two antennas, one for transmission and the other one for reception, which will be moved above the ground at a certain distance (in this specific case 70 cm) to scan the ground surface. The main parameters of radar are the range and the resolution. The range of SFCW radar is given by the frequency step and the resolution by the frequency range. For landmine detection, one needs both deep penetration and high resolution. Taking into account these requirements and the international regulations with regards to frequency allocation, the frequency range for SFCW radar has been chosen from 400 MHz to 4845 MHz. The low frequency will provide deep penetration while high frequency will give the needed resolution. The antenna system has to comply with these frequency range, has to have a stationary phase point because the distance is phase embedded, and should have no extra delays within the antenna because they will worsen the down range resolution of the system. Moreover, because the system is a bistatic one (one antenna for transmission and one antenna for reception, 52 cm apart), the coupling signal and the common footprint have to be as low as possible to provide both dynamic range and cross-range resolution. Several ultra wideband (UWB) antennas had been investigated for this application and the best fit was found for two Archimedean spirals with opposite sense of rotation that have a low level of the leakage signal and provide circular polarization, which is a very important advantage in this application. However, the Archimedean

spiral has a frequency dependent delay that will worsen the range resolution. In order to remove the delay, two procedures are investigated in this paper.

2. ANTENNA SYSTEM—TIME DOMAIN RESPONSE

In order to identify the delay within the antenna systems, the two Archimedean antennas had been connected to a vector network analyzer (VNA) set to work as an SFCW radar from 400 MHz to 4845 MHz in 128 steps (the frequency step was 35 MHz). One antenna will transmit 128 frequencies and the other will receive the reflected signals.

If a metallic plate is placed at a distance d of the antenna system and the power transmitted by the radar is equalized for all 128 frequencies, then the transmitted signalcan be written like

$$u(t) = \frac{1}{128}\sum_{n=1}^{128} Ae^{j2\pi f_n t}, \tag{1}$$

where A is a constant. This signal propagates to the metallic plate and is scattered back to the antenna system. The received signal can be written as

$$s(t, t_{in}) = \frac{1}{128}\sum_{n=1}^{128} r_n Ae^{j2\pi f_n (t-t_{in})}, \tag{2}$$

where t_{in} denotes the delay due to the antenna system and due to propagation towards the metallic plate and back; r_n includes the propagation losses as well as the reflection losses.

The delay t_{in} is frequency dependent because the delays within the antenna system depend on frequency [1]. This happens due to the principle of operation of spiral antenna, which states that this antenna has an active part that changes with frequency such as the ratio between the geometrical dimension and the wavelength stays constant. The lower frequencies have a larger delay than the higher frequencies [2] because at lower frequencies, the currents have to propagate a longer way before being radiated than the currents at higher frequencies. This will lead to an increased time response as can be seen in Figures 1–3, where three situations are displayed.

The first one corresponds to the case when the ifft transform is applied to a set of 128 frequencies that cover the entire operational band of the radar and the synthesized time response is about 9 nanoseconds. The second case is for 108 frequencies (first 20 frequencies are removed) and the synthesized time response is around 5.5 nanoseconds. In the third situation, the last 20 frequencies are removed and the synthesized time response is about 8.5 nanoseconds.

The signals for the three situations are given by

$$s_1(t_{in}) = \frac{1}{128}\sum_{n=1}^{128} r_n Ae^{-j2\pi f_n t_{in}}; \tag{3}$$

for all 128 frequencies,

$$s_2(t_{in}) = \frac{1}{108}\sum_{n=21}^{128} r_n Ae^{-j2\pi f_n t_{in}}; \tag{4}$$

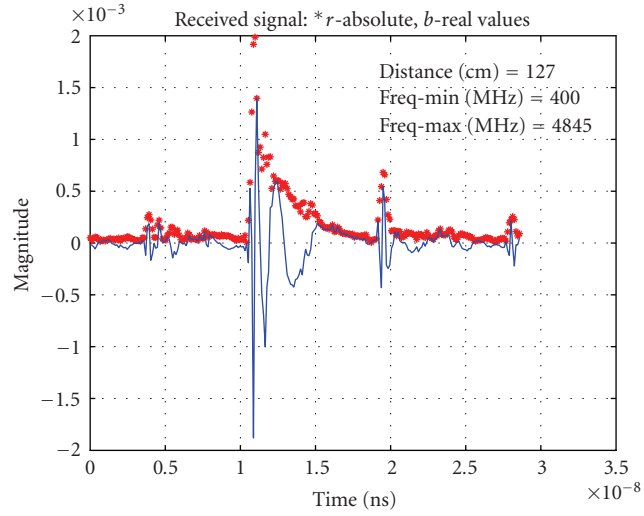

FIGURE 1: The received signals, in time domain, for 4445 MHz frequency span (128 frequencies).

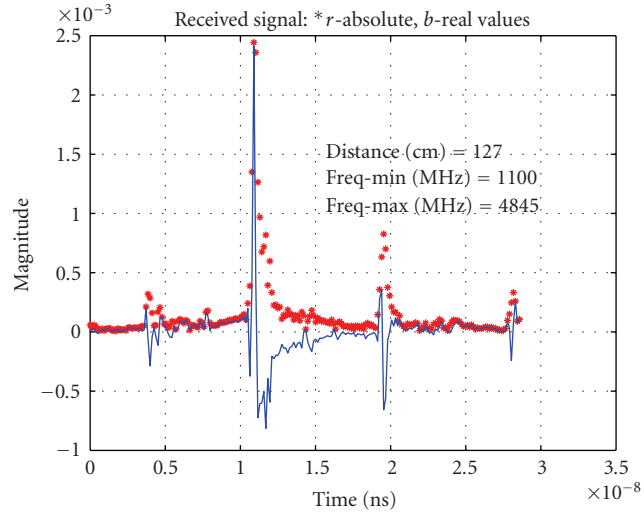

FIGURE 2: The received signals, in time domain, for 3745 MHz frequency span (108 frequencies—first 20 removed).

for 108 frequencies (first 20 removed), and

$$s_3(t_{in}) = \frac{1}{108}\sum_{n=1}^{107} r_n Ae^{-j2\pi f_n t_{in}}; \tag{5}$$

for 108 frequencies (last 20 removed), where $0 \le t_{in} \le 1/\triangle f$.

3. CALIBRATION USING AN ERROR-TERM FLOW GRAPH

3.1. Formulation

The time response of the antenna system is drastically increased due to different delays associated with different frequencies (Figures 1–3). The calibration procedure should remove this phase dispersion introduced by the antenna system. Because the radar measures amplitude and phase,

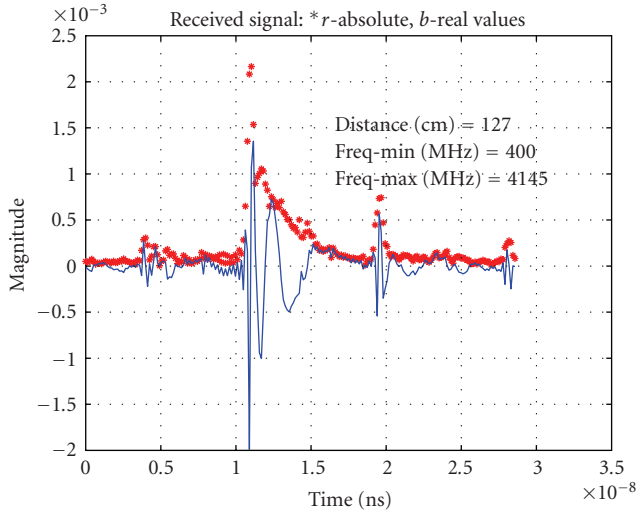

Figure 3: The received signals, in time domain, for 3745 MHz frequency span (108 frequencies—last 20 removed).

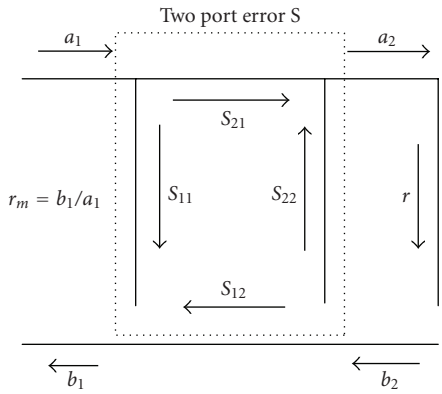

Figure 4: Error-term flow graph for one port vector network analyzer; a and b are reflected waves.

in other words, it is a vectorial device, the calibration procedure that is in place for vector network analyser should be followed. A vector network analyser is calibrated by using an error-term flow graph for the frequency signal like in Figure 4.

The reflection coefficient r, which is a function of frequency, can be calculated using the well-known formula [3]

$$r = \frac{r_m - S_{11}}{S_{12}S_{21} - S_{22}(r_m - S_{11})}. \tag{6}$$

The three unknowns (S_{11}, S_{22}, and $S_{12}S_{21}$) in (6) can be determined by measuring the reflections from three standards, which for vector network analyzer are: the open, the short, and the matched load. If we are able to find the three standards, this procedure can be used for calibration.

In order to apply this procedure to SFCW radar, let us assume that all systematic linear errors are included in the two-port error network. The correct reflection coefficient, r, from an object will be given by formula (6), where S_{11} represents the leakage signal and S_{22} depends on the radar cross section (RCS) of the antenna and takes into account the multiple ground bounces. The three unknowns can be computed if three independent calibration targets are available. According to [4], these are represented by free space ("empty room," $r = 0$), a metal plate ($r = -1$), and a wire grid. The error coefficients can be derived as follows:

$$\begin{aligned} S_{11} &= r_{mo}, \\ S_{22} &= \frac{r_{mg} - r_{mo} + r_g(r_{mg} - r_{mo})}{r_g(r_{mg} - r_{mm})}, \\ S_{12}S_{21} &= -(r_{mg} - r_{mo})(1 + S_{22}), \end{aligned} \tag{7}$$

where r_{mo}, r_{mm}, and r_{mg} denote measured signals for "empty room," metal plate, and metal grid and r_g is the exact reflection coefficient of the metal grid. Having the error coefficients, the reflection coefficient for any object can be easily computed using (7).

The disadvantage of this procedure lies in the difficulty to find the precise value of the reflection coefficient for the third standard (wire grid). It can be found either by measurements or by calculation. V. Mikhnev has proposed a procedure that replaces the third standard by measuring the reflection coefficient from the same metallic plate placed in one or several shifted locations. If the reflectivity of the antenna system from the free space is low ($S_{22} \ll 1$), which is true when the antenna system is high enough above the ground, then the reflection coefficient of the shifted metal plate can be written as

$$r_{sp}(f) = r_m(u + vf + wf^2)\exp(-j2\beta l), \tag{8}$$

where r_{sp} is the reflection coefficient of the metallic plate placed in a shifted position; l is the offset distance, β is the phase propagation constant and u, v, and w are parameters which depend on l. If S_{22} is neglected then, the real value of the reflection coefficient can be computed using the formula

$$r = \frac{r_m - S_{11}}{S_{12}S_{21}}, \tag{9}$$

and the unknown parameters u, v, and w can be determined by solving the optimization problem

$$\sum_n \left| \frac{r_{sp}(f_n) - r_o(f_n)}{r_m(f_n) - r_o(f_n)} - (u + vf_n + wf_n^2)\exp(-j2\beta_n l) \right| \longrightarrow \min. \tag{10}$$

3.2. Experimental results

Having the values of the unknown parameters in (8), the exact value of the reflection coefficient of the shifted metallic plate can be computed. This method provides better results if the offset distance is around a quarter of a wavelength. The SFCW radar is an ultra wideband device; it operates from 400 to 4845 MHz so it is not possible to make measurements at a quarter of wavelengths for all frequencies. This is why several measurements have been made at different shifted positions (l = 97; 99; 102; 105; 109; 112; 115; 118; 122; 125; 127 cm) and

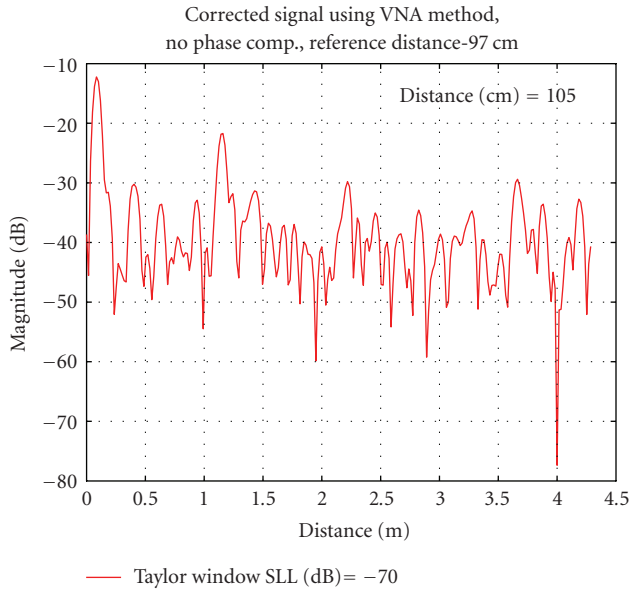

Figure 5: Calibrated A-scan using VNA method; reference distance-97 cm, separation 105 cm.

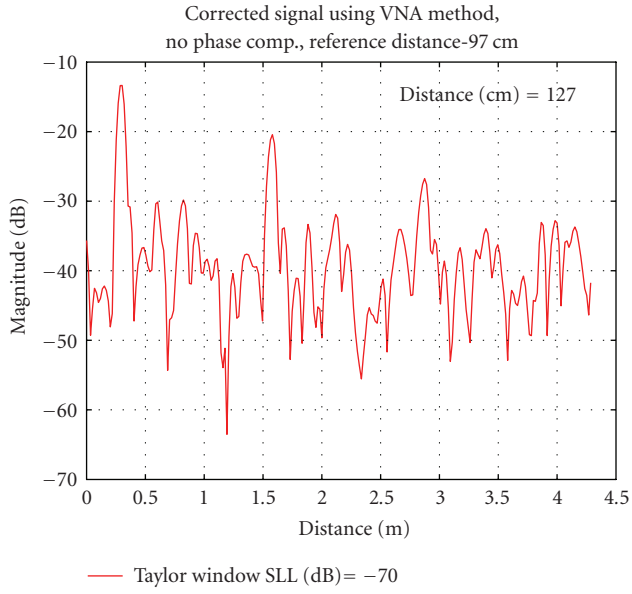

Figure 6: Calibrated A-scan using VNA method; reference distance-97 cm, separation 127 cm.

the unknown parameters are computed following a process of minimization of (10). The values obtained for the three unknowns are $u = 0.96888$; $v = 0.22 \times 10^{-10}$; and $w = 0$.

The results are presented in Figures 5 and 6. Comparing these figures with Figure 1, it can be seen that the time response decreases and the level of the signal just after the ground reflection is as low as −40 dB below the main peak. This outcome is quite important because the mines are supposed to be in this area.

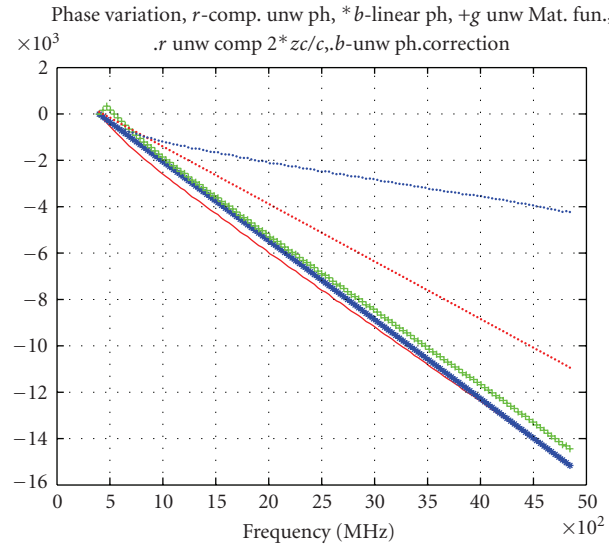

Figure 7: Unwrapped phase variation for 128 frequencies (light red: measured; dark blue: linearized; green: unwrapped with Matlab function; light red: due to propagation; light blue: phase error).

4. CALIBRATION PROCEDURE USING A METALLIC PLATE

The other procedure, which has been investigated, is the single reference procedure. It supposes to use a single reference, a metallic plate, located at a certain distance of the antenna system [5]. In this case, the transmitted signal is given by (1) and the received signal can be calculated using (2). As was mentioned before, the delays within the transmitting and the receiving antennas are frequency dependent. In fact, this effect can be seen in Figure 7 where the phase variation of the antenna is compared with a linear one. The upper line represents the phase distortion. As can be seen in Figures 1–3, there are multiple bounces so, in order to make a proper calibration, the first reflection should be isolated. Time domain gating can do this. In order to decrease the side lobes level, a Kaiser window, with $\beta = 3.15$, is applied.

The received signal after down conversion at the output of I and Q mixers will be

$$s(\dot{t}_{in}) = \frac{1}{128}\sum_{n=1}^{128} r_n k_n A e^{-j2\pi f_n t_{in}}, \tag{11}$$

where k_n takes into accountthe variation of the gain along the processing chain for each frequency (channel). If the reference plate is located at a reference distance r_{ref} then the two-way propagation delay t_{ref} is given by

$$t_{\text{ref}} = \frac{2r_{\text{ref}}}{c}, \tag{12}$$

where c is the speed of light.

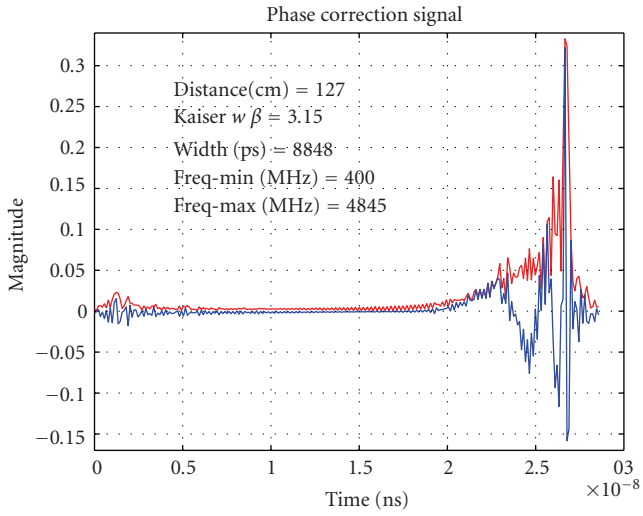

FIGURE 8: Phase correction signal in time domain (red line: absolute values, blue line: real values).

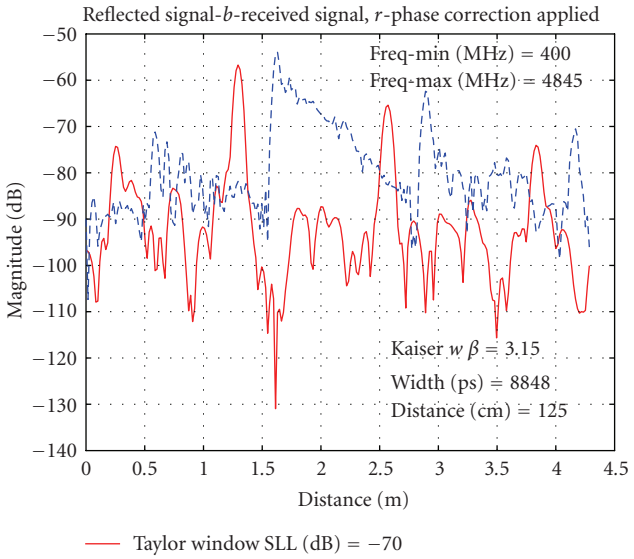

FIGURE 9: A range profile before calibration (blue line) and after calibration (red line) for a distance of 125 cm; data measured with VNA.

The correction signal that removes the phase dispersion within the antenna system will be

$$s_{\text{cor}}(t_{\text{ref}}, t_{in}) = \frac{1}{128}\sum_{n=1}^{128} e^{-j2\pi f_n (t_{\text{ref}} - t_{in})}. \tag{13}$$

This signal is displayed in Figure 8, in time domain, and it is the mirror image of the gated signal.

The calibrated signal is obtained by multiplying, for each frequency, the measured signal with the one given by (13). After an ifft is applied, a calibrated range profile as in Figures 9 and 10 is got. Matched filter calibration procedure has been employed for SFCW radar because the level of the side lobes in the vicinity of the ground reflection is lower than for VNA.

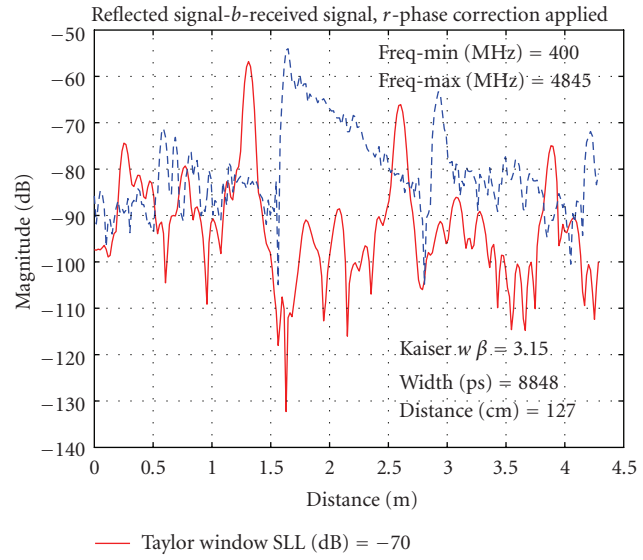

FIGURE 10: A range profile before calibration (blue line) and after calibration (red line) for a distance of 127 cm; data measured with VNA.

5. SYSTEM CALIBRATION

The SFCW radar works in frequency domain. After down conversion, at the output of the quadrature mixers, for each frequency, a complex signal is obtained. The phase and magnitude of these signals depend on the parameters of the processing chain and among these, the balance between I and Q channels plays a crucial role. The calibration of SFCW radar is made in two stages. In the first stage, the delays within the transmitter and the receiver are removed by making a direct connection, with a known length cable, between the two and dividing each A scan by this reference signal.

For one frequency, the output signal $s_1(f_k)$, after the first stage, is given by

$$s_1(f_k) = \frac{s_m(f_k) - s_{\text{off}}(f_k)}{s_{m\_\text{ref}}(f_k) - s_{\text{off}}(f_k)} e^{-j2\pi f_k (l_{\text{ref}}/v)}, \tag{14}$$

where $s_{\text{off}}(f_k)$ is the DC offset signal for the kth frequency, $s_{m\_\text{ref}}(f_k)$ is the measured signal with a direct connection between the transmitter and the receiver, $s_m(f_k)$ is the measured signal, l_{ref} is the length of the cable used for direct connection and v is the propagation velocity through the cable. The measured data, in time domain, after applying a Hamming window in order to decrease the side lobes level, are presented in Figure 11.

In the second stage, the single reference procedure is followed. To this end, a metallic plate is placed at 1.27 m separation of the antenna system. The performances that come out can be seen in Figures 12 and 13 where an uncalibrated and a calibrated A scans are showed. The first peak of the signal on Figure 13 is the coupling signal, the second is the reflection from the ground and the next are

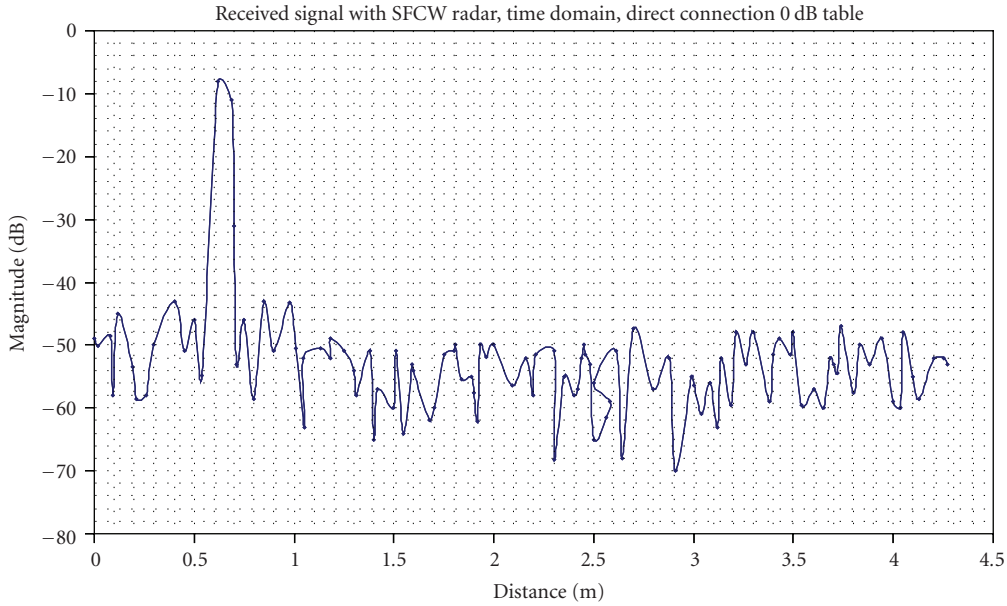

Figure 11: *A* scan (range profile) after removing the DC offset and the delays within the transmitter and the receiver.

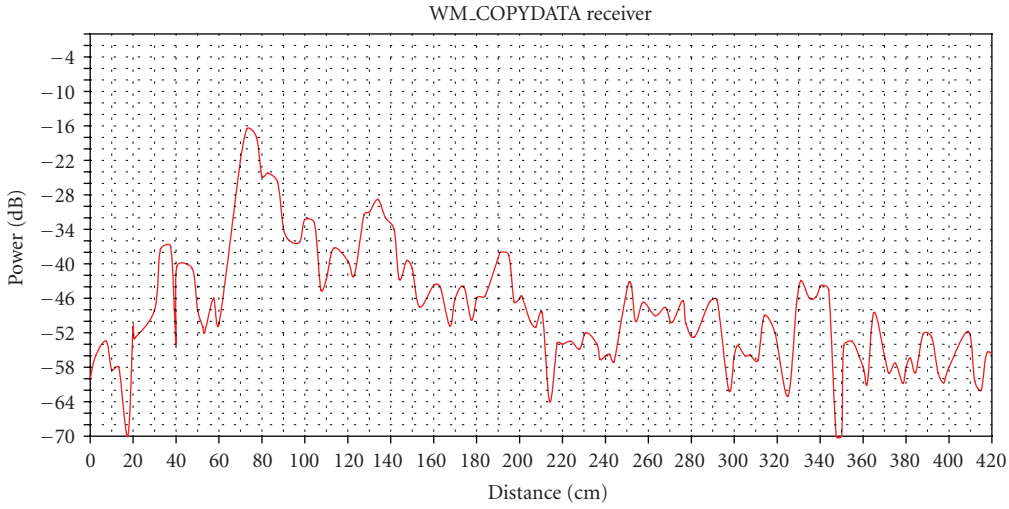

Figure 12: *A* scan measured with SFCW radar before calibration.

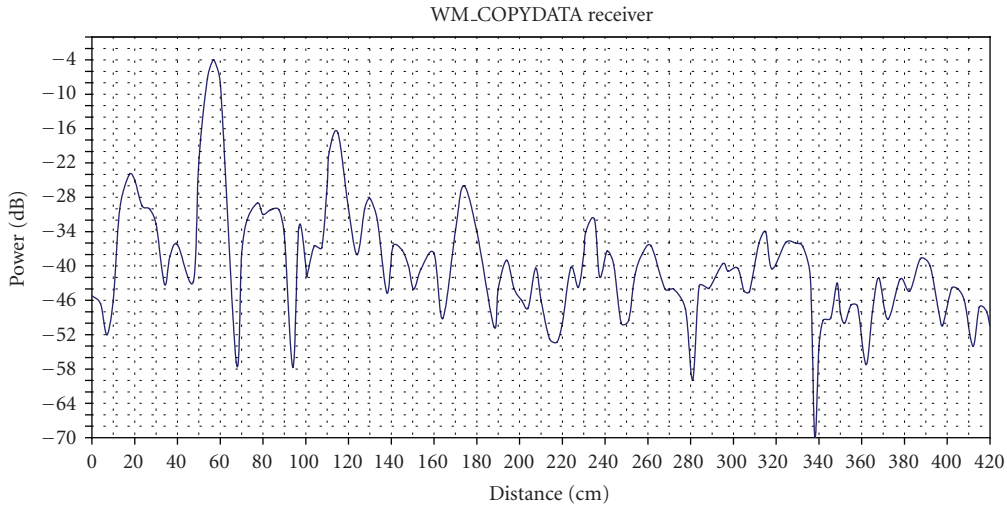

Figure 13: *A* scan measured with SFCW radar after matched filter calibration procedure is applied.

multiple bounces so, the third peak can be used as a measure of the RCS of the antenna system.

6. CONCLUSIONS

(1) The Archimedean spiral antenna is a very good candidate for UWB application but it has a major drawback because it is a dispersive system, which means that the delay within the antenna is frequency dependent. As a result, in any application where the shape of the pulse is important as, for instance in radar systems, a calibration procedure to remove the delays within the antenna system is needed.

(2) The SFCW radar works in frequency domain it means it has a synthesized time domain pulse that defines the downrange resolution of the system. The procedures described in the paper should be used to calibrate the system for the delays within the antenna system.

(3) For this application, because the landmines are supposed to be shallowly buried, the enlargement of the time domain response means that the reflection from the ground surface will cover the weaker signals, which may come from landmine. For the same reason, the level of the signal just after the first reflection from the ground has to be as low as possible.

(4) The three standards procedure that is used for the vector network analyzers calibration cannot be employed because of the difficulty to find a suitable standard besides the "empty room" and the metallic plate. Nonetheless, an alternative of this procedure, which supposes to replace the third standard with the same metallic plate but placed in a shifted position, has been analyzed. The side lobe level obtained with this procedure is just −40 dB below the main peak and is not enough for this application.

(5) The matched filter procedure needs a large separation between the antenna system and the reference plate in order to avoid the overlapping of the second reflection with the first one. Since the side lobes level near the ground reflection is decreased to around −50 dB (Figures 9 and 10), in comparison with VNA procedures that provides only −40 dB (Figures 5 and 6), this procedure is used for SFCW radar calibration.

(6) The Archimedean spirals work with circular polarization, which had been proven very useful for this application because it exhibits the shape of the detected object (the reflected signal embeds information about both dimensions of the object).

(7) The resolution of the SFCW radar is given by the time response of the system. As can be seen on Figures 12 and 13, it is improved from tens of cm to cm, which is in accordance with theoretical down range resolution given by the bandwidth of the radar.

REFERENCES

[1] D. J. Daniels, D. J. Gunton, and H. F. Scott, "Introduction to subsurface radar," *IEE Proceedings*, vol. 135, no. 4, part F, pp. 278–320, 1988.

[2] I. Nicolaescu, P. van Genderen, and J. Zijderveld, "Archimedean spiral antenna used for stepped frequency radar-footprint measurements," in *Proceedinngs of the Antenna Measurement Techniques Association (AMTA '02)*, pp. 555–560, Cleveland, Ohio, USA, November 2002.

[3] G. H. Bryant, *Principles of Microwave Measurements*, Peregrinus, London, UK, 1990.

[4] A. Al-Attar, J. Daniels, and H. F. Scott, "A novel method of suppressing clutter in very short range radar," in *Proceedings of the International Conference on Radar*, pp. 419–423, London, UK, October 1982.

[5] I. Nicolaescu, "Stepped frequency continuous wave radar used for landmines detection," Tech. Rep. IRCTR-S-004-03, Delft University of Technology, Delft, The Netherlands, 2003.